

GC
7.4
M45
1979

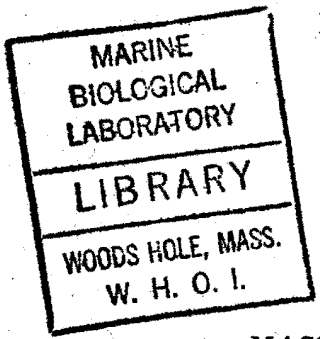
ANALYSIS AND INTERPRETATION OF
TIDAL CURRENTS IN THE COASTAL BOUNDARY LAYER

by

PAUL WESLEY MAY

B. S., Southern Missionary College (1972)

SUBMITTED IN PARTIAL FULFILLMENT OF THE
REQUIREMENTS FOR THE DEGREE OF
DOCTOR OF SCIENCE



at the

MASSACHUSETTS INSTITUTE OF TECHNOLOGY

and the

WOODS HOLE OCEANOGRAPHIC INSTITUTION

May, 1979

Signature of Author
Joint Program in Oceanography, Massachusetts Institute of Technology
- Woods Hole Oceanographic Institution, and Department of Earth and
Planetary Sciences, and Department of Meteorology, Massachusetts
Institute of Technology, May, 1979.

Certified by
Thesis Supervisor

Accepted by
Chairman, Joint Oceanography Committee in Earth Sciences,
Massachusetts Institute of Technology - Woods Hole Oceanographic
Institution.

ANALYSIS AND INTERPRETATION OF
TIDAL CURRENTS IN THE COASTAL BOUNDARY LAYER

by

PAUL WESLEY MAY

Submitted to the Massachusetts Institute of Technology - Woods Hole Oceanographic Institution Joint Program in Oceanography on May 1, 1979, in partial fulfillment of the requirements for the degree of Doctor of Science

ABSTRACT

Concern with the impact of human activities on the coastal region of the world's oceans has elicited interest in the so-called "coastal boundary layer"—that band of water adjacent to the coast where ocean currents adjust to the presence of a boundary. Within this zone, roughly 10 km wide, several physical processes appear to be important. One of these, the tides, is of particular interest because their deterministic nature allows unusually thorough analysis from short time series, and because they tend to obscure the other processes.

The Coastal Boundary Layer Transect (COBOLT) experiment was conducted within 12 km of the south shore of Long Island, New York to elucidate the characteristics of the coastal boundary layer in the Middle Atlantic Bight. Analysis of data from this experiment shows that 35% of the kinetic energy of currents averaged over the 30 m depth are due to the semidiurnal and diurnal tides.

The tidal ellipses, show considerable vertical structure. Near-surface tidal ellipses rotate in the clockwise direction for semidiurnal and diurnal tides, while near-bottom ellipses rotate in the counterclockwise direction for the semidiurnal tide. The angle between the major axis of the ellipse and the local coastline decreases downward for semidiurnal and increases downward for diurnal tides. The major axis of the tidal ellipse formed from the depth averaged semidiurnal currents is not parallel to the local shoreline

but is oriented at an angle of -15 degrees. This orientation "tilt" is a consequence of the onshore flux of energy which is computed to be about 800 watts/m.

A constant eddy viscosity model with a slippery bottom boundary condition reproduces the main features observed in the vertical structure of both semidiurnal and diurnal tidal ellipses. Another model employing long, rotational, gravity waves (Sverdrup waves) and an absorbing coastline explains the ellipse orientations and onshore energy flux as a consequence of energy dissipation in shallow water. Finally, an analytical model with realistic topography suggests that tidal dissipation may occur very close (2-3 km) to the shore.

Internal tidal oscillations primarily occur at diurnal frequencies in the COBOLT data. Analysis suggests that this energy may be Doppler-shifted to higher frequencies by the mean currents of the coastal region. These motions are trapped to the shore and are almost exclusively first baroclinic mode internal waves.

Thesis Supervisor: Gabriel T. Csanady

Title: Senior Scientist
Woods Hole Oceanographic Institution

ACKNOWLEDGEMENTS

This thesis contains contributions from many individuals, only a few of which can be mentioned in this short space. In particular, I would like to thank my thesis advisor, Dr. G. T. Csanady, for his support, encouragement, and patience. Dr. R. C. Beardsley, another member of my thesis committee, kindly provided the data from the CMICE experiment as well as a number of helpful discussions.

Dr. Tom Hopkins and Jim Lofstrand, both from Brookhaven National Laboratory, were very helpful in obtaining a useable version of the COBOLT spar buoy data. In addition, Bert Pade and Neal Pettigrew braved inclement weather and seasickness to perform the daily hydrographic surveys.

The data processing was aided greatly by the "Data Dollies" of the Woods Hole Oceanographic Institution Buoy Group. Nancy Pennington, in particular, was consulted on numerous occasions and cheerfully corrected many of my programming errors.

I would also like to thank Doris Haight and May Reese for their help in typing the various versions of this thesis.

This work was supported by the Department of Energy under Brookhaven National Laboratory subcontract numbers 325373-S and 359133-S.

TABLE OF CONTENTS

ABSTRACT	1
ACKNOWLEDGEMENTS	3
TABLE OF CONTENTS.	4
LIST OF FIGURES.	7
LIST OF TABLES	11
I. The Coastal Boundary Layer and COBOLT Experiment	
A. Introduction	12
B. The COBOLT experiment.	15
C. The experiment site.	16
D. Coastal measurements	18
E. The COBOLT instrumentation	20
F. COBOLT experiments and data.	23
G. Data processing.	32
II. Nearshore Tidal Current Observations	
A. Introduction	34
B. Tidal analysis	35
C. The tidal ellipse.	41
D. Tidal observations in the Middle Atlantic Bight.	44
E. Analysis of the COBOLT tidal signal.	51

F.	Results of the semidiurnal analysis.	54
G.	Band structure of the semidiurnal admittances. . .	67
H.	Results of the diurnal analysis.	68
I.	Consequences and conclusions	75
III.	Tidal Dynamics and Theory	
A.	Tidal theory	84
B.	Vertical structure of tidal currents	89
C.	Effects of friction on tidal propagation	99
D.	The Sverdrup-Poincare wave model	101
E.	The Sverdrup wave--no reflection	107
F.	The Poincare wave--perfect reflection.	107
G.	The combination Sverdrup-Poincare wave	113
H.	Comparison of the model to observations.	123
I.	The effects of local topography.	128
J.	Summary.	144
IV.	Observations of Coastal Internal Tides	
A.	Introduction	147
B.	Dynamical theory of the internal tides	148
C.	Solutions for constant Brunt-Vaisala frequency . .	150
D.	Solutions for an arbitrarily stratified fluid. . .	152
E.	The mean fields of the COBOLT experiment	156

F. Internal tidal oscillations.	164
G. Modal structure of the internal tides.	173
H. Comparison to theory	183
I. Energy and flux of the internal tide	186
J. Conclusions.	190
REFERENCES	191
BIOGRAPHICAL NOTE.	198

LIST OF FIGURES

FIGURE	PAGE
1-1 Cross section and classification of the Middle Atlantic Bight continental shelf	14
1-2 The South shore of Long Island	17
1-3 Configuration of a typical COBOLT spar buoy	22
1-4 Locations of the four spar buoys of the May, 1977 experiment	25
1-5 Depth profile off Tiana beach, location of spar buoys, instrument packages, and hydrographic survey stations	26
1-6 Calendar for the May, 1977 experiment showing buoy duration and hydrographic surveys	27
1-7 Configuration of MESA-CMICE mooring #5	30
2-1 Definition sketch of the tidal ellipse	42
2-2 Cophase contours of the Middle Atlantic Bight from to Swanson, 1976	45
2-3 Tidal ellipses in the New York Bight from Patchen, Long, and Parker, 1976 (MESA)	49
2-4 Variance preserving plot of the kinetic energy of depth-averaged currents at buoy 2	55
2-5 Semidiurnal tidal ellipses in the COBOLT experiment	59

2-6	Semidiurnal tidal ellipses in the CMICE experiment	60
2-7	Vertical profile of semidiurnal ellipticity	61
2-8	Vertical profile of semidiurnal orientation	63
2-9	Vertical profile of semidiurnal kinetic energy	64
2-10	Semidiurnal ellipses for depth-averaged currents	66
2-11	Band structure of semidiurnal admittances	70
2-12	Vertical profile of diurnal ellipticity	73
2-13	Vertical profile of diurnal orientation	74
2-14	Vertical profile of diurnal kinetic energy	76
2-15	Diurnal ellipses for depth-averaged currents	77
3-1	Theoretical vertical profiles of semidiurnal ellipticity	93
3-2	Theoretical vertical profiles of semidiurnal orientation	94
3-3	Theoretical vertical profiles of diurnal ellipticity	96
3-4	Theoretical vertical profiles of diurnal orientation	97
3-5	Geometry of the step shelf tidal model	102
3-6	Ellipticity versus offshore distance for perfect reflection ($r'=1$) and several positive incidence angles	109
3-7	Ellipticity versus offshore distance for perfect reflection ($r'=1$) and several negative incidence angles	110
3-8	Orientation angle versus offshore distance for perfect reflection ($r'=1$) and several incidence angles	112
3-9	Ellipticity angle versus offshore distance for imperfect reflection (positive incidence angle)	115

3-10	Ellipticity versus offshore distance for imperfect reflection (negative incidence angle)	116
3-11	Orientation angle versus offshore distance for imperfect reflection	117
3-12	Ellipticity versus orientation angle at $y=0$; incidence angle varied while holding reflection coefficient constant	120
3-13	Ellipticity versus Orientation angle at $y=0$; reflection coefficient varied while holding incidence angle constant	121
3-14	Ellipticity versus Orientation angle at $y=0$; varying incident wave frequency	122
3-15	Ellipticity versus Orientation angle at $y=0$ with COBOLT observations plotted for three semidiurnal frequencies)	124
3-16	Plot of $\ln(H_0 - H)$ versus offshore distance at COBOLT site, plus linear curve fit	130
3-17	Comparison of modelled depth dependence with actual depth profile off Tiana Beach	131
3-18	Orientation angle versus offshore distance for depth dependent model	138
3-19	Ellipticity versus offshore distance for depth dependent model	139
3-20	Kinetic energy versus offshore distance for depth dependent model	141
3-21	Dissipation versus offshore distance for depth dependent model	143

3-22	Free surface elevation versus offshore distance for depth dependent model	144
4-1	Twenty-two day average sigma-t cross section at the COBOLT site	157
4-2	Twenty-two day average Brunt-Vaisala frequency profiles at buoys 2-4	161
4-3	Salinity time series from instruments 31 and 34	163
4-4	Sigma-t time series at all levels, buoy 3	165
4-5	Sigma-t energy density spectrum from insts. 21-23 & 31-33	166
4-6	Temperature energy density spectrum from insts. 21-23 & 31-33	168
4-7	Onshore velocity energy density spectrum, insts 32-32	169
4-8	Alongshore velocity energy density spectrum, insts 32-33	170
4-9	Kinetic energy density at 15 m for Sept., 1975 experiment	174
4-10	First three vertical velocity modes at buoy 3	175
4-11	First three horizontal velocity modes at buoy 3	177
4-12	Fitted first baroclinic mode at buoy 2: onshore velocities	181
4-13	Fitted first baroclinic mode at buoy 2: alongshore velocities	182

LIST OF TABLES

TABLE	PAGE
1-1 Summary of data returns from Tiana Beach site	31
2-1 The wavelength of the semidiurnal tide	47
2-2 The tidal components used to construct the reference time series	52
2-3 The semidiurnal admittances and coherences	56
2-4 The band structure of the semidiurnal admittances	69
2-5 The diurnal admittances and coherences	71
4-1 Numerical values of T, S, N, and $\sigma-t$: buoy 3	159
4-2 Longshore mean currents at all instruments	162
4-3 Isopycnal displacements for buoys 2 & 3 for all levels: 12 hr., 18 hr., and 24 hr. periods	172
4-4 Energy distribution among modes 0-2; buoys 2-4; 12 hr., 18 hr., and 24 hr. periods	179

CHAPTER I

THE COASTAL BOUNDARY LAYER AND THE COBOLT EXPERIMENT

A. Introduction

The coastal regions of the world's oceans have been the subject of increased interest among physical oceanographers in the last decade. This narrow band of shallow water surrounding the continents has long been regarded as too insignificant to affect the great volume of the deep ocean, and as too complicated to conform to simple dynamical theories. The economic and environmental considerations of offshore fisheries and energy related activities, however, have promoted new scientific interest in the dynamics of the continental seas as an important study in its own right. Improved measurement capabilities have also spurred interest and have led to the realization that shallow water dynamics are not as complicated as originally supposed (see reviews by Niiler (1975) and Winant (1978)). A complete understanding of the interaction of these regions with the rest of the ocean may yet prove the shelf's importance to the deep ocean if only as a boundary condition.

The breadth of the continental shelf is by definition limited to areas within the one hundred meter isobath (Sverdrup, Johnson, and Fleming, 1942), though shelf studies often pass beyond the continental shelf break or continental slope in order to include important

conditions in the transition of shallow to deep ocean flow. Off the east coast of the United States, specifically in a region known as the Middle Atlantic Bight, the shelf extends typically to an offshore distance of 100 km. A representative cross section of this particular region is shown in figure 1.

The eastern continental shelf is often subdivided further into the areas depicted in figure 1: a region of sharp topographic change, known as the shelf break; inner and outer shelf regions; and, a narrow coastal boundary layer (CBL) close to the shore. The dynamical dissimilarities of the inner and outer shelf, and the shelf break, often noted as the basis of this classification scheme, are summarized in Beardsley, Boicourt, and Hansen (1976).

The region that is of interest here is the coastal boundary layer. This term is applied to a band of water on the order of 10 km wide, which is small compared to the width of the continental shelf, but large compared to the several hundred meter width of the surf zone or littoral zone. From a physical standpoint, the coastal boundary layer is the region where offshore currents adjust to the presence of the coast.

Early work on the Great Lakes (Csanady, 1972) has revealed features which are peculiar to the coastal boundary layer. In particular, observational evidence and theoretical modelling led to the concept of a coastal "jet" (see Csanady, 1977 for more details)--- the primary mechanism by which the nearshore waters respond to transient meteorological forcing. With regard to the relatively

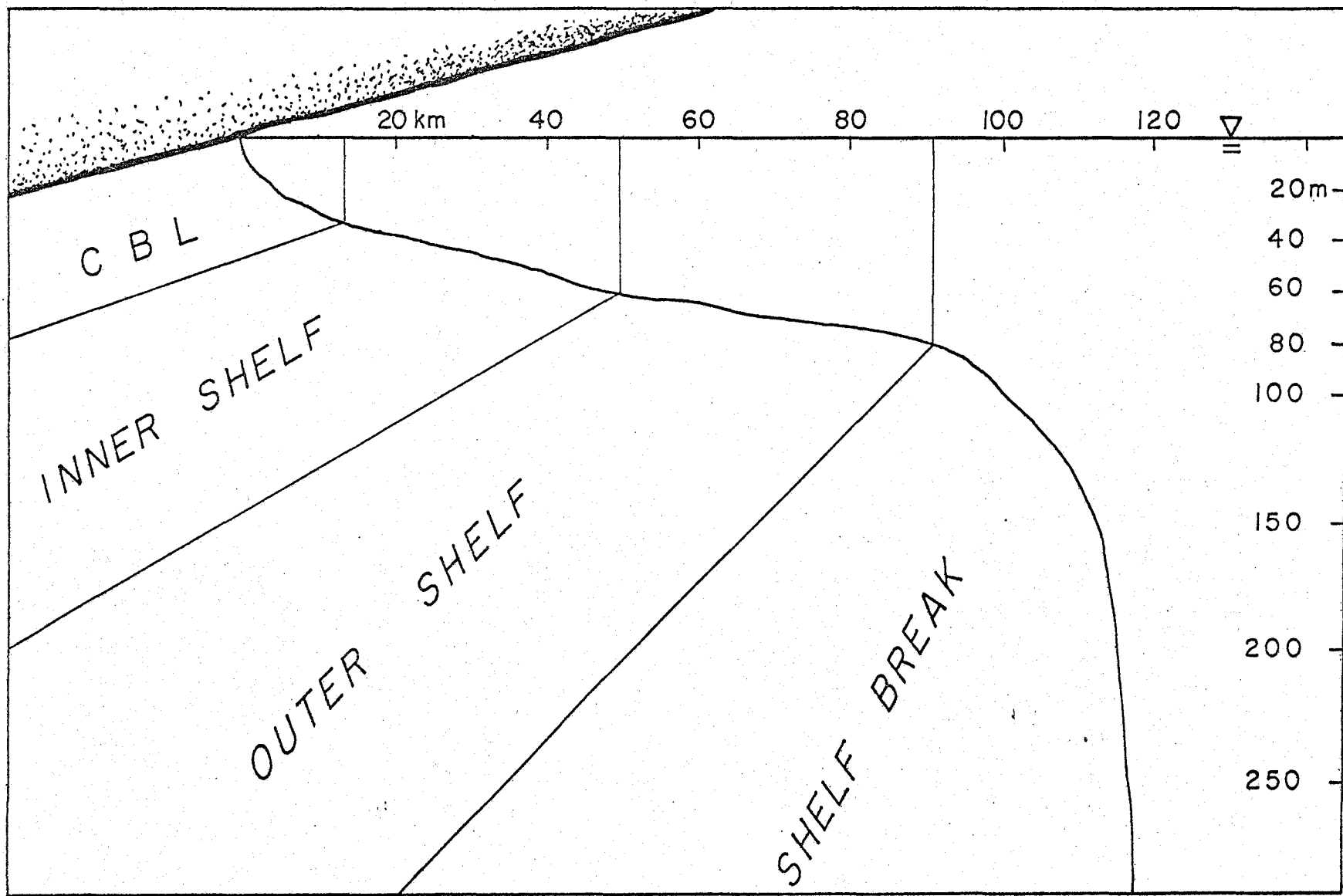


Figure 1-1 Cross section and classification of the Middle Atlantic Bight continental shelf

uncomplicated dynamics of large lakes, this model has substantially increased the understanding of coastal boundary layer processes.

While application of the coastal jet theory to oceanic coastal boundary layers is straightforward, observational confirmation is more difficult since suitable current observations in the coastal region are rare. And, what observations do exist are more difficult to interpret than the equivalent Great Lakes observations due to the presence of strong tidal currents and large scale flows associated with the rest of the shelf. So, it appears that two additional time scales are important in the oceanic coastal boundary layer: the mean circulation, and tidal frequency motions.

As part of the Coastal Boundary Layer Experiment (COBOLT), this thesis is directed toward developing an understanding of the tidal frequency motions of the coastal boundary layer. This goal is pursued by presenting a description of the tidal currents of the coastal zone followed by a conceptual model that reproduces many of the observed features of the barotropic or surface tide. The question of internal or baroclinic tides is addressed with a detailed description and comparison to existing models.

B. The COBOLT experiment

The COastal Boundary Layer Transect (COBOLT) experiment was designed specifically to study the complexity of the coastal zone. Drawing from experience gained on the Great Lakes and taking advantage of newly developed instrumentation, it was planned to provide a

detailed spatial and temporal picture of the wind-driven coastal boundary layer, the currents induced by tides, and the interaction with the large scale circulation of the continental shelf. The motivation for the experiment was provided by proposals to locate power stations offshore, together with the realization that very little was known observationally about the coastal boundary layer. The project represents the joint efforts of the Woods Hole Oceanographic Institution and Brookhaven National Laboratory (BNL).

C. The experiment site

The southern coast of Long Island was chosen for the site of the COBOLT experiment because of its similarity to an idealized straight coastline. This region is shown in figure 2. Tiana Beach, the shore location point, is 135 km east of New York City and the New York Bight Apex, and 60 km west of Montauk Point, the terminus of Long Island. The approximate coordinates of the experiment are $40^{\circ} 45'N$ and $72^{\circ} 30'W$. The site enjoys easy access from the protected waters of Shinnecock Bay through Shinnecock Inlet which is about 6 km east of Tiana Beach, and is also within reasonable distance of Brookhaven National Laboratory.

Geographically, the coast of Long Island forms part of the northern boundary of the Middle Atlantic Bight. The coast itself is a virtually continuous barrier sand bar, with only four or five breaks for entrances to protected bays in its 195 km extent. The shallow water topography is formed from loose, large-grained sands and is

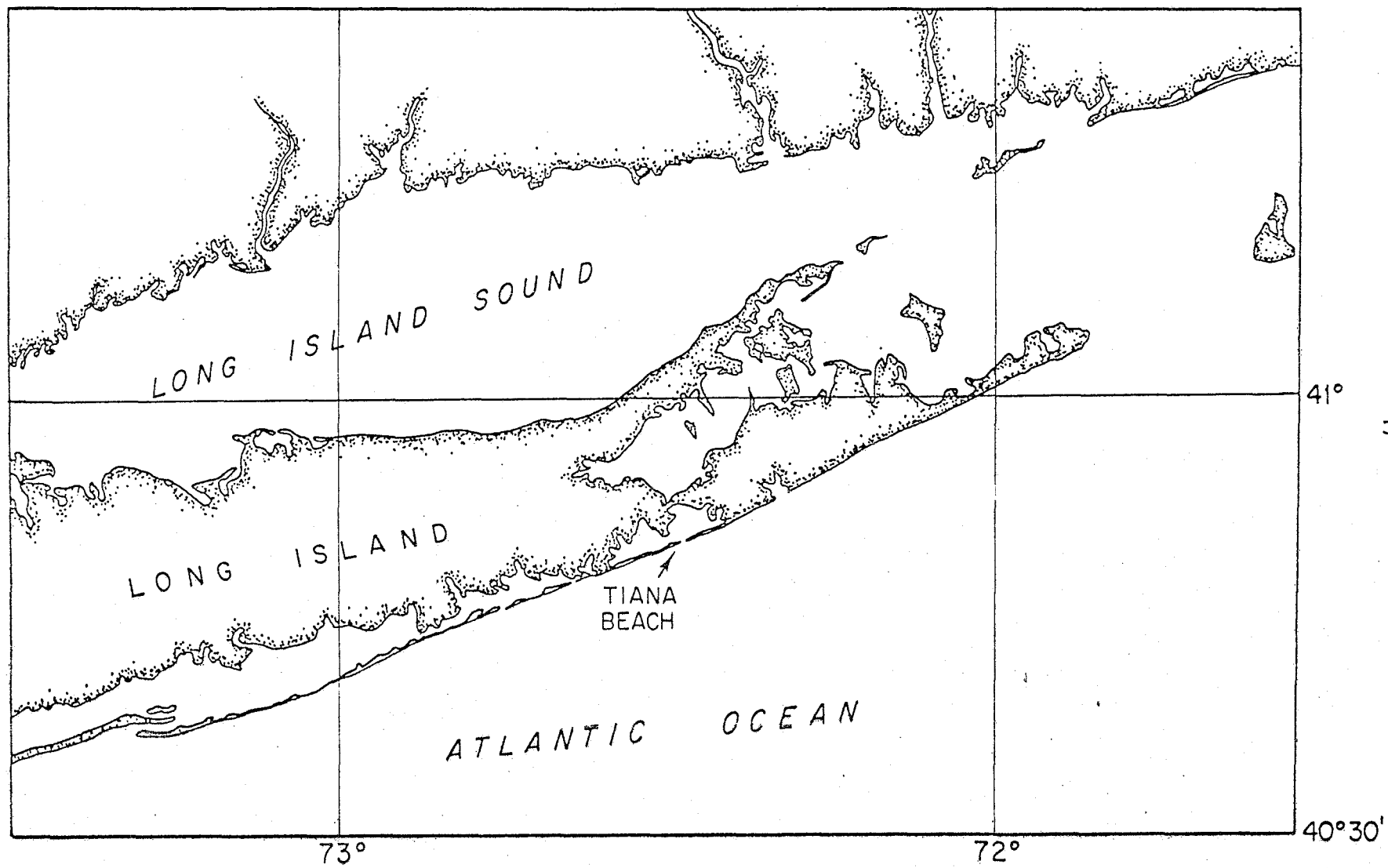


Figure 1-2 The south shore of Long Island

remarkably smooth with minor "swale" features (Swift et al., 1973) as the only irregularities.

While topographic features are smooth and lead to relatively uncomplicated dynamics, there are other features of the COBOLT experiment site which may complicate the interpretation of the data. The presence of Long Island Sound, for example, is likely to have some effects on COBOLT measurements. Tidal observations (Redfield, 1958 and Swanson, 1976) show strong aberrations in tidal propagation characteristics up to 50 km away from the entrance to the Sound. A close-to-resonant response gives rise to very large currents in the vicinity of Montauk Point and tidal phases that change rapidly from point to point. Also, the Sound is a major source of fresh water (Ketchum and Corwin, 1964). Since the runoff from Long Island itself is relatively minor, the Sound is probably the origin of any freshening that occurs at the COBOLT site.

In addition, the proximity of Shinnecock Inlet may influence the measurements. Though it is narrow (about 200 m wide) and less than 5 m deep at most points, visual surveys indicate that the plume of tidal discharge reaches 2-3 km out to sea and is visible as far down-shore as 6 km. Thus, it is conceivable that moorings which are close to shore may show the effects of being near to the inlet.

D. Coastal measurements

One of the major hurdles encountered in mounting a near-shore measurement program is that of choosing adequate instrumentation. It

is well known that current meters mounted near the surface are profoundly affected by high frequency gravity waves even when carefully conceived sampling and averaging schemes are employed. Instruments which sample speed and direction (via Savonius rotor and vane), such as the VACM or Aanderaa current meters, are particularly susceptible to rectification of wave-induced orbital velocities, even when mean velocities are of comparable magnitude (McCullough, 1977). Taut rope moorings also contribute to measurement errors in several ways. Strong currents, such as those encountered in the coastal zone, cause sizable vertical excursions of the instrumentation. Also, surface layer fluctuations can be transmitted down the flexible rope to contaminate measurements at deeper instruments. Finally, the lack of torsional rigidity may introduce directional errors.

The presence of a nearby coast adds measurement problems of its own. In addition to the increased possibility of human interference, the nearness of the coast causes low frequency currents to be polarized in the alongshore direction and increases the probability of measuring important onshore velocities incorrectly. For example, in a strong alongshore current of 50 cm/sec, as little as one degree of error in orientation can cause a 1 cm/sec error in the onshore velocity--an amount which is comparable to the true mean value of the onshore currents.

To the list of difficulties to be overcome in instrument and mooring design must be added the demand that both temperature and salinity be measured. Unlike the deep ocean, where tight temperature-

salinity properties make a functional relationship between the two possible and eliminate (somewhat) the need for salinity time series, shallow coastal waters have no such links. Density variations are controlled by salinity at certain times of the year and by temperature at other times, and both signals are usually large. In order to separate dynamic effects, time series of both parameters are essential.

Despite the difficulties, several useful experiments have been carried out in the coastal zone of the Middle Atlantic Bight using conventional measurement techniques. Two of the most notable of these are the EG&G Little Egg Inlet experiment (EG&G, 1975) and the New York Bight MESA project (Charnell and Hansen, 1974). Even in view of these successes, a concerted effort was made in the COBOLT experiment to eliminate the potential sources of error in conventional instrumentation and moorings, and to add measurement capabilities not available in earlier studies. These requirements necessitated a radical departure from common deep water mooring design and instrumentation.

E. The COBOLT instrumentation

The mooring platform for the COBOLT instruments, the "Shelton Spar", was developed for coastal work off La Jolla, California. It is constructed of sections of 2 1/2" diameter PVC pipe (Lowe, Inman, and Brush, 1972). The moorings utilize specially designed universal joints to allow the spar to articulate freely at the several junction points, without sacrificing too much of the inherent rigidity of the pipe. Since it is torsionally rigid (torsional variations are

estimated by the manufacturer to be less than 1°), the mooring requires only one compass to determine the orientation of the four current meters mounted on it in rigid steel cages. With the large buoyancy element employed, the mooring also tilts very little; typically 10° in a 50 cm/sec current. Thus much of the vertical and rotational movement of conventional moorings is eliminated.

Instrument packages consist of two temperature probes--one "local" and one "remote"--and induction-type conductivity sensor, and a Marsh-McBirney, Inc. Model 711 electromagnetic current meter. The current meters have two orthogonal sets of electrodes mounted on a 2 cm diameter vertically oriented cylinder. The principles of operation of the electromagnetic current meter are discussed in Cushing (1976).

A typical mooring configuration, pictured in figure 3, employs four of the instrument packages described above, plus one compass, two orthogonal tilt sensors, an in situ data processor, and a radio transmitter. Sensor outputs are low-pass filtered in real time with a five second time constant (the stated response time for the sensors is typically one second) and continuously integrated in the data processor. Averaged values of the measured parameters are then transmitted, on command, to a shore station at Tiana Beach. Operators can therefore adjust the sampling rate or detect faulty instruments while the experiment is in progress. Experiment duration is limited, typically to one month periods, by the large power consumption of the transmitter. Further technical details are available in Dimmler, et. al. (1976).

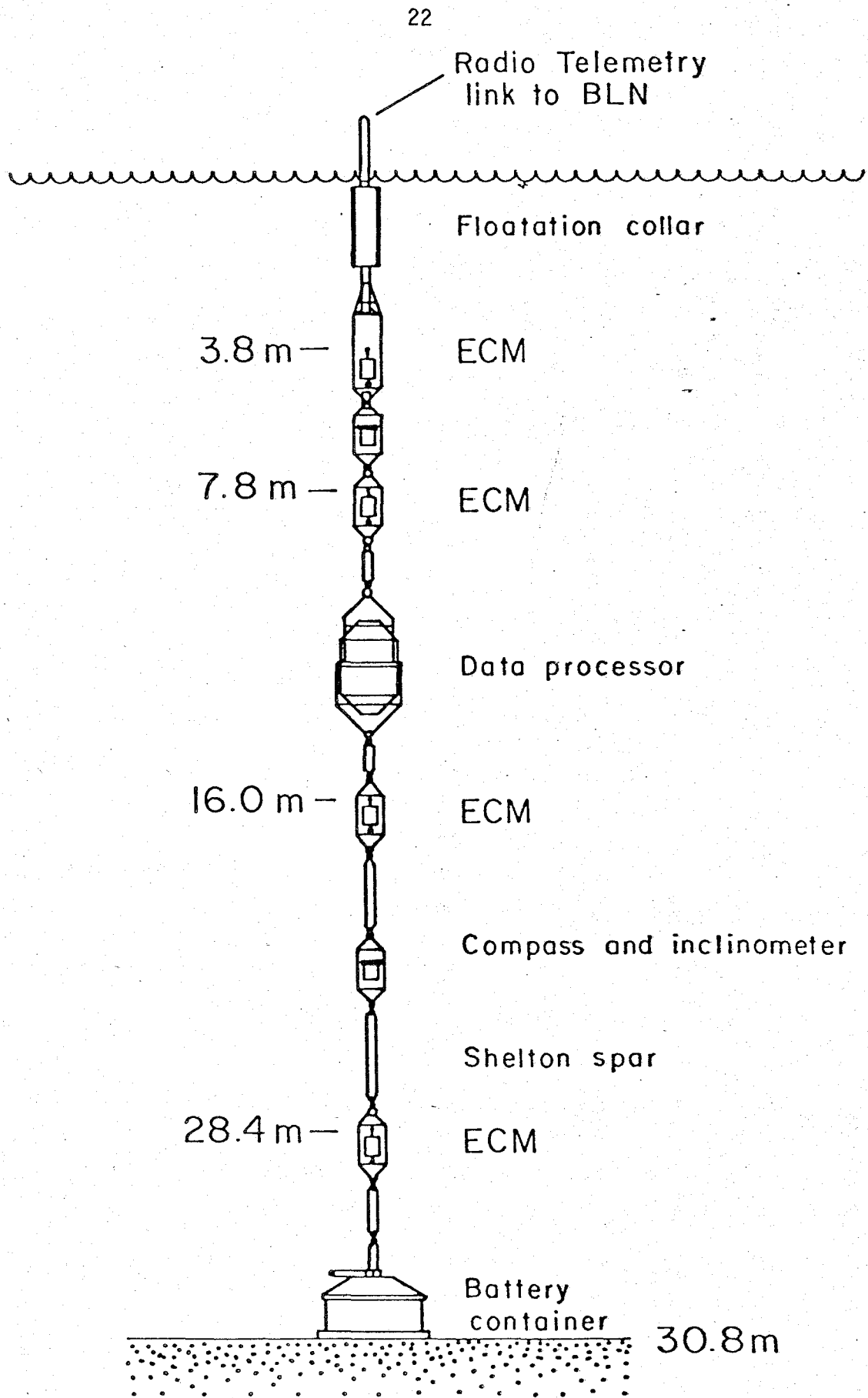


Figure 1-3 Configuration of a typical COBOLT spar buoy

In spite of the care taken in its design, the COBOLT moorings have not been perfected yet. An experiment somewhat related to COBOLT, the Current Meter Inter-Comparison Experiment (CMICE), was conceived as an opportunity to test the merits of the spar system against conventional moorings and instruments. In this experiment, described in detail by Beardsley, et. al. (1978), six moorings were deployed off Tiana Beach in a line parallel to the shoreline and 6 km from the beach. Four of the moorings were conventional taut rope moorings instrumented with a variety of current meters (mostly of the Savonius rotor and vane type), while the remaining two moorings were the Shelton spars. A comparison of the measurements of these instruments suggest that there are some deficiencies in the COBOLT moorings and instrumentation. The sources of possible error in the COBOLT velocity measurements are:

1. Errors due to mis-orientation of the single compass or misalignment of current meters with respect to the compass.
2. Errors due to a shift in the zero point of either or both of the current meter axes.
3. Errors due to asymmetric gain adjustment of the two current axes or non-cosine response of the sensors.

F. COBOLT experiments and data

After some pilot studies, the full COBOLT array of four spar buoys was first deployed in May, 1977. The location of each of the four buoys and their relationship to surrounding features is shown in

figure 4. The buoys were placed approximately 3 km, 6 km, 9 km and 12 km away from the shore, and stand in 20 m, 28 m, 30 m, and 32 m of water respectively.

The instrument configuration, bottom profile, and location of daily hydrographic casts (described subsequently) is shown schematically in figure 5. Instruments are identified by a sequence of two numbers: the first corresponding to the number of the buoy on which the instrument is mounted, and the second corresponding to the order, starting at the top, in which it is mounted. An attempt was made to place instruments at standard depths: the shallowest at 3.8 meters below the surface; intermediate instruments at 7.4 meters and 16.0 meters; and the deepest at 2.4 meters above the bottom. Buoy 1 is the exception to this rule with one instrument at 12.3 meters instead of 16.0 meters.

The spars were launched on April 29, 1977, and regular data recovery from all four buoys was initiated on April 30. Because of non-uniform power drain, endurance of the different moorings varied significantly. Buoys 1 and 3 were operational until May 29; buoy 2 until May 24; and buoy 4 until May 17. The operation period of the experiment is summarized in figure 6.

The quality of instrument records (containing temperature(1), temperature(2), salinity, X velocity and Y velocity) is good, with the exclusion of buoy 1 which suffered numerous irrecoverable data gaps. These gaps were uniformly spread throughout the data and amounted to a total of 140 hours out of a total duration of about 700 hours or

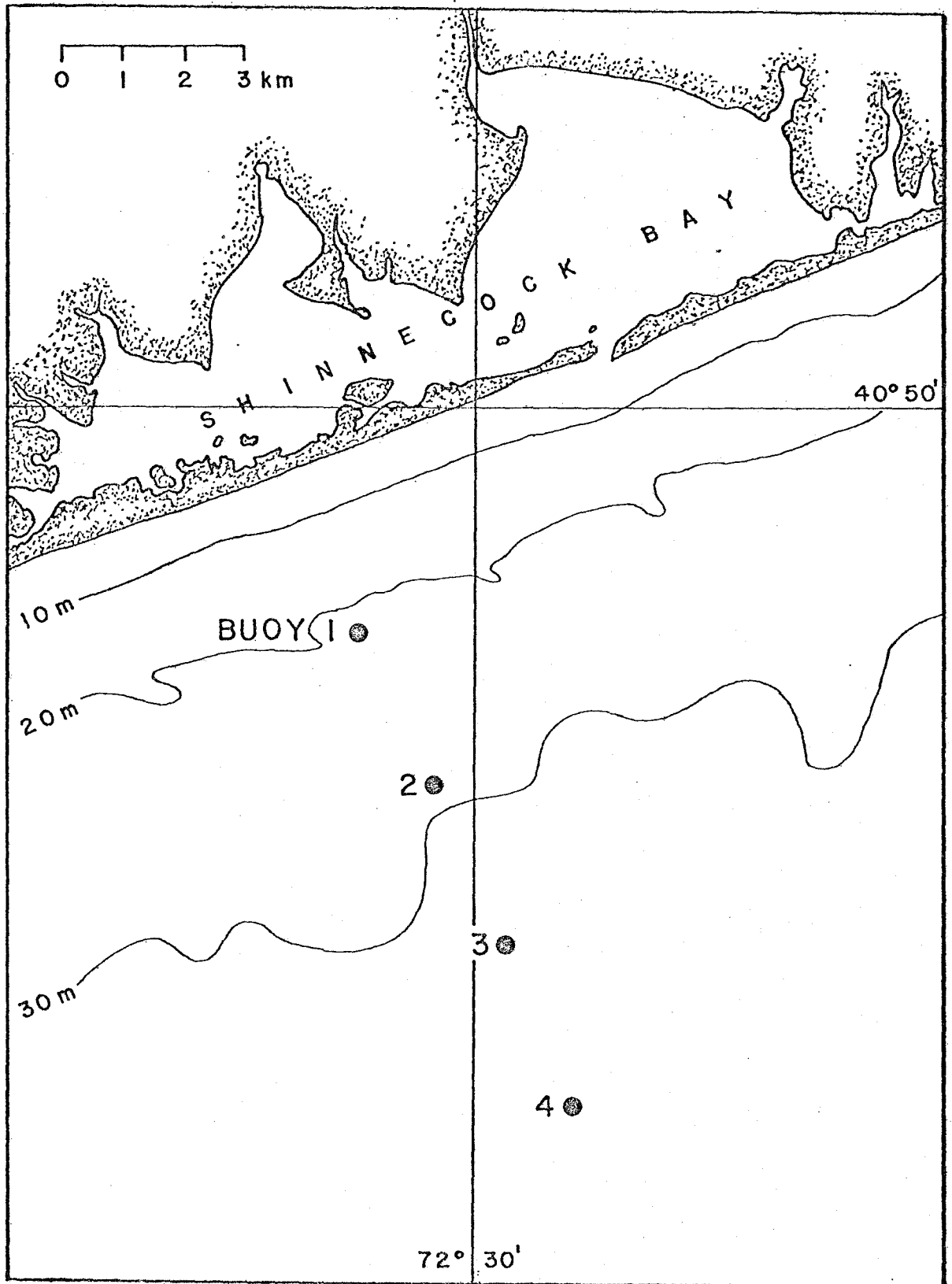


Figure 1-4 Locations of the four spar buoys of the May, 1977 experiment

MAY 1977

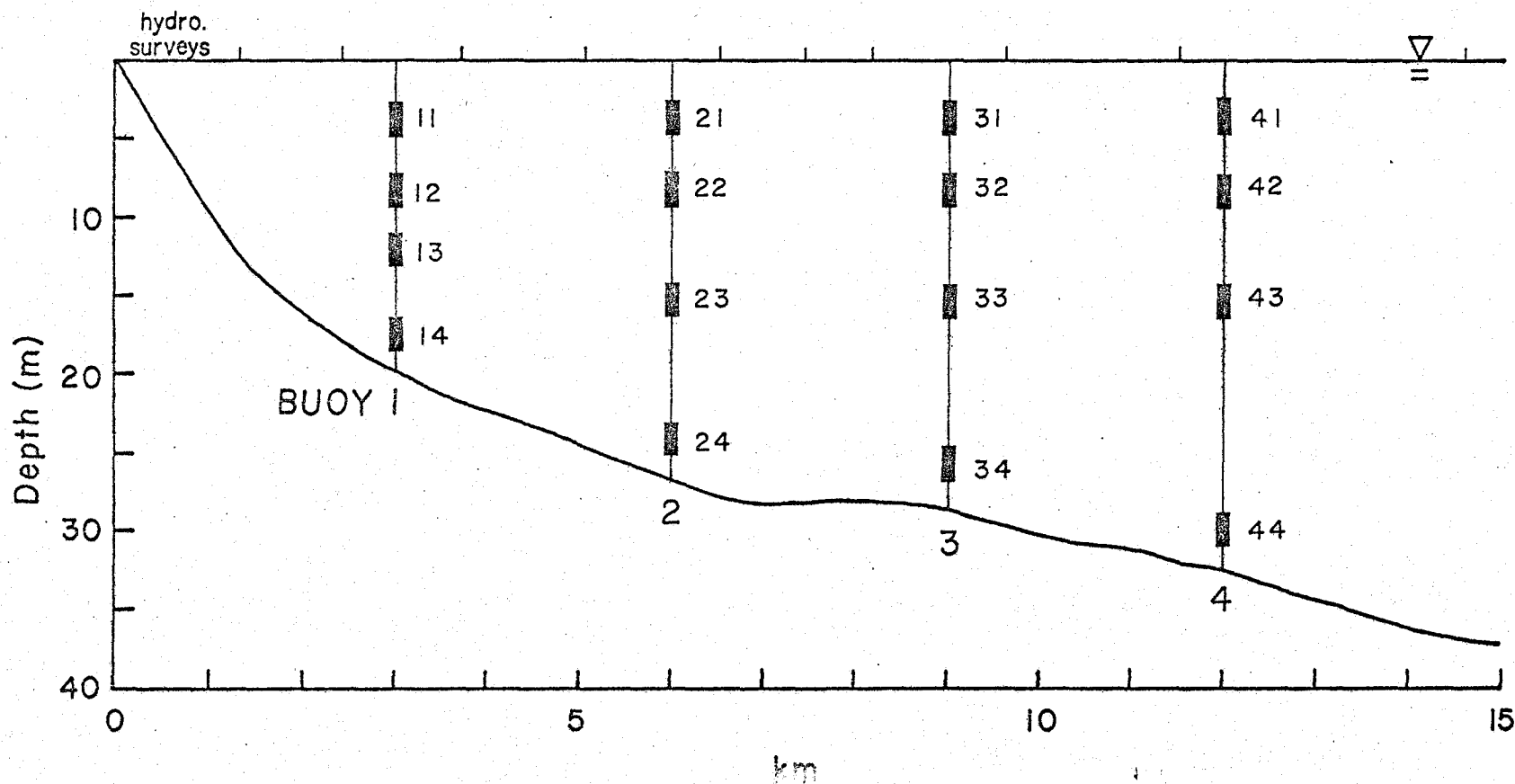


Figure 1-5 Depth profile off Tiana beach, location of spar buoys, instrument packages, and hydrographic survey stations

MAY 1977

APR. 30
START

BUOYS
2
3
4

1	2	3	4	H	5	H	6	H	7	H	
8	H	9	10		11	H	12		13		
			6 hr gap buoys 3, 4								
15	H	16	H	17		18	H	19	H	20	H
				END BUOY 4							
22	H	23	H	24	H	25	H	26	H	27	H
				END BUOY 2							
29	H	30	H	31	H						
END BUOY 3											

H = Hydrographic survey conducted

Figure 1-6 Calendar for the May, 1977 experiment showing buoy duration and hydrographic surveys

one-fifth of the total time. One stretch of ten days was relatively free of long gaps and consequently can be used for limited comparisons, but the rest of the record was abandoned as unacceptable for tidal analysis. Data from the other three moorings, buoys 2-4, showed only occasional, short data gaps during periods of high speed flow. These gaps never exceeded 6 hours in length.

In conjunction with the continuous buoy measurements, daily hydrographic surveys of the area were conducted. These STD measurements were made from a small vessel at ten semipermanent locations along a line coincident with the spar transect. The spacing of the stations, about 1 km, was chosen to give more detailed resolution of the coastal boundary layer than was provided by the 3 km spacing of the spar buoys. Although they were performed only in fair weather, and although they are aliased by tidal fluctuations, the hydrographic surveys are a valuable source of information in interpreting the spar data.

In view of the questions that have arisen concerning the data quality of the spar system, and in an effort to assure the generality of the tidal analysis to follow, results from two other moorings will be included in the discussion: a "reference" mooring from the CMICE experiment, and the COBOLT pilot mooring.

The mooring chosen from the CMICE experiment was deployed by the MESA New York Bight project and has been used extensively in their field program. The instrumentation consisted of four Aanderaa RCM-4 current meters; three mounted on a subsurface taut wire mooring, and a

fourth mounted beneath a surface spar buoy to reduce wave-induced biases. The mooring is shown schematically in figure 7. One instrument at 11 meters below the surface did not function. The experiment was conducted at the COBOLT site in February, 1976 with this particular mooring positioned 6 km offshore at approximately the same location as buoy 2 of the May COBOLT experiment. The mooring was designated as #5 in the CMICE experiment and since this conforms to the convention used here, it is retained in Table 1 and in further references.

The COBOLT pilot mooring, launched in September, 1975, was a single mooring placed 11 km offshore at roughly the same location as buoy 4 of the May, 1977 experiment. It had working instrument packages at 7.8 m, 16.0 m, and 27.0 m and was in 32 m of water. The details concerning this mooring and the others employed in this analysis are summarized in Table 1.

Although it seems a bit capricious to compare current observations taken during different seasons and separated in time by more than a year, there are elements of the signal which are expected to remain the same throughout the year. Even if meteorological forcing and stratification are different, the tidal signal should be deterministically related to well-known forces at all times. Including these additional moorings will allow comparison between certain aspects of the COBOLT experiment spar buoys and the relatively well-understood Aanderaa current meters of the CMICE experiment, and will also assure that measurements are somewhat representative of different seasons and conditions.

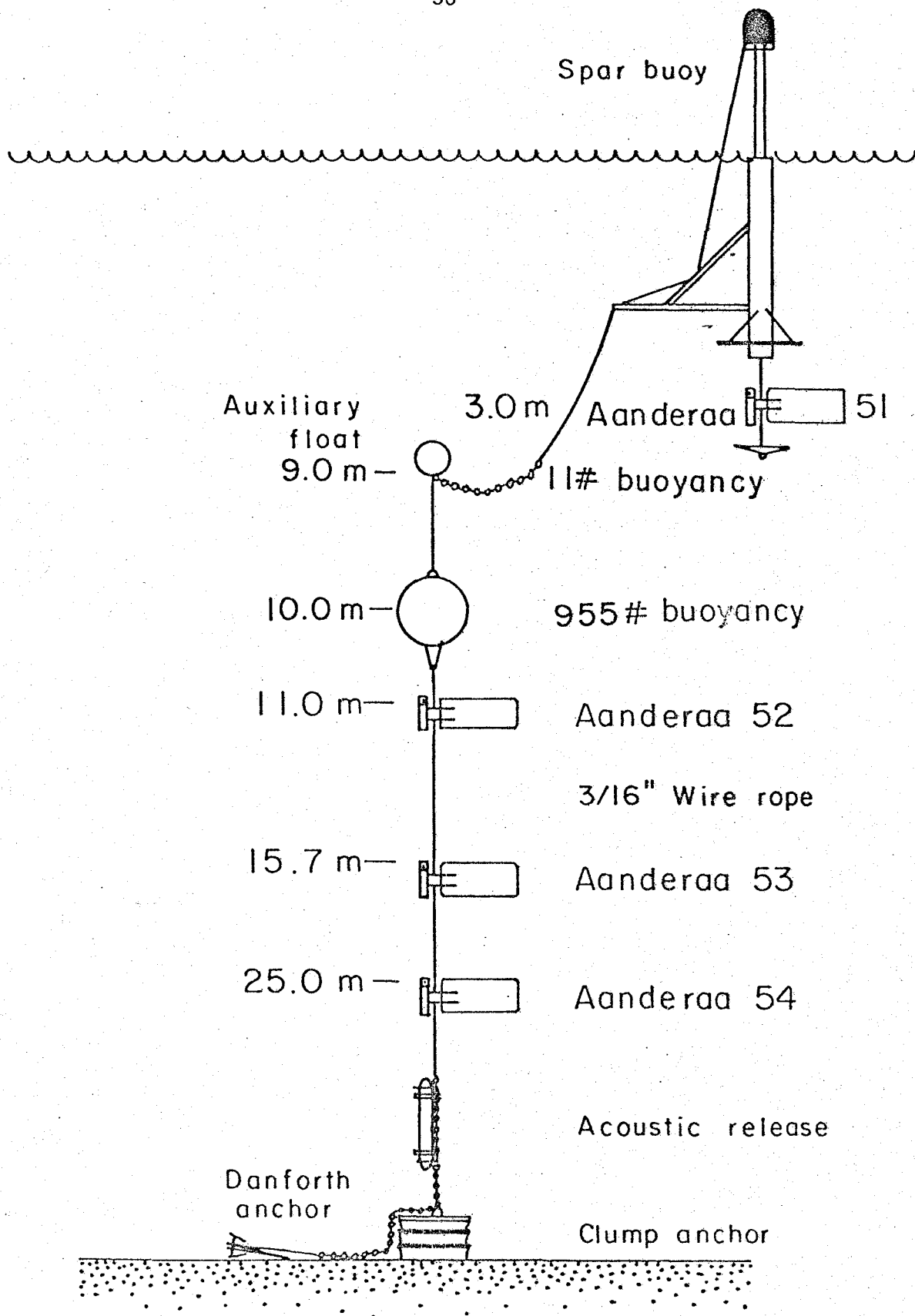


Figure 1-7 Configuration of MESA-CMICE mooring #5

TABLE 1-1

SUMMARY OF DATA

RETURNS FROM THE TIANA BEACH SITE

<u>Date of Exp.</u>	<u>No.</u>	<u>Duration</u>	<u>Water Depth</u>	<u>Dist. offshore</u>	<u>Depth of working Current meters</u>
Sept., 1975	0	640 hr	32.6 m	11 km	4.2 m, 16.5 m, 29.7 m
Feb., 1976	5	697	26.5	6	3.0, 15.7, 25.0
May, 1977	1	240	20.3	3	3.8, 7.8, 12.3, 17.9
	2	577	27.7	6	3.8, 7.8, 16.0, 25.3
	3	700	30.8	9	3.8, 7.8, 16.0, 28.4
	4	385	32.3	12	3.8, 7.8, 16.0, 29.9

G. Data Processing

The data sampling scheme is unique to the spar system and presents minor problems of its own. Buoys were interrogated at separate times and at intervals that ranged from five minutes to several hours. Since ordinary time series analysis demands that sampling intervals be uniform and that measurements for comparison be taken at a common time, the COBOLT data were adjusted to a common time base with a one-hour sampling interval (one hour was by far the most common interval in the data). This was achieved by first averaging all data over a one-hour time period and then interpolating values to the closest whole hour. The interpolation scheme was a third order polynomial that used four data points (two on either side of a gap) to determine the value of the function on the hour. This method has the advantage of eliminating the sharp bends introduced by linear interpolation, and of filling gaps in strong tidal flows with consistent curves. For periodic functions, for example, the polynomial interpolation gives a good visual fit for record gaps of up to one-half of a period. Using this as a guideline, COBOLT data gaps were filled only if they were less than or equal to 6 hrs in duration; that is, half a semi-diurnal tidal period.

The X and Y component velocities output from the current meters were converted to east and north components using the headings from the single on-board compass. Then the coordinate system was rotated by 22° to conform to the local coastline at Tiana Beach. The uncertainties usually associated with this maneuver are quite small

here due to the uniformity of the coastline and topographic features. The result is a coordinate system with the X axis aligned alongshore to the east-northeast and the Y axis pointing onshore to the north-northwest.

The salinity time series from the May, 1977 experiment required special attention. Mean salinities (computed from the measured conductivities) differed by as much as 3 o/oo from adjacent instruments and by as much as 2 o/oo from values obtained from nearby STD measurements. These aberrant salinity measurements resulted in large, persistent inversions in the computed density. Since there was nothing to suggest that these aberrations were other than the result of a constant calibration offset, an effort was made to correct them using two different procedures. In the first, salinities were offset enough to eliminate all density inversions, while in the second, salinities were made to conform to nearby daily hydrographic survey salinities in a least-squares sense. These adjustments agree quite closely and give credence to the notion that errors were due only to calibration offsets and not to instrument drift or malfunction.

CHAPTER II

NEARSHORE TIDAL CURRENT OBSERVATIONS

A. Introduction

An examination of the current records from any coastal experiment in the Middle Atlantic Bight shows that they are dominated (visually at least) by tidal oscillations. Even though such short period oscillations do not transport mass, momentum, or other passive properties of the water column (except in non-linear cases), the large amplitude of the tidal signal often obscures other aspects of the records--particularly if the observation period is short. As a consequence, an understanding of some of the slower and less obvious processes of the coastal region may be improved by an understanding of the tides.

Certain aspects of coastal dynamics may also be directly controlled or influenced by the surface tides. Internal waves, for example, are known to be generated by tidal currents interacting with the topographic features found in coastal areas (Rattray, 1960). There is also evidence (Bowden and Fairbairn, 1956) that the tidal currents control the high background level of turbulence observed in coastal regions--acting, in effect, like a stirring rod. This is closely related to the question of tidal dissipation, much of which is presumed to occur on the continental shelves of the world's oceans (Munk, 1968). Little is known about the mechanisms by which this is

accomplished or the regions in which it occurs. A study of coastal tides may serve to illuminate the subject.

Because of the deterministic nature and relatively high frequency of tidal currents, information can be extracted from relatively short duration experiments. The thirty days of data gathered during May 1977 is suitable for some forms of tidal analysis and will be used in the hope of elucidating some of the local dynamics of the nearshore region, comparing the performance of the COBOLT mooring system to other systems, and as a first step in obtaining detided records for analysis of low frequency phenomena.

B. Tidal Analysis

Tidal analysis is traditionally carried out using the harmonic method introduced by Lord Kelvin in 1867. The frequencies, ω_i , at which forcing occurs, are obtained from expansions of the tidal potential (Doodson and Warburg, 1941) and used in the expression

$$F(t) = a_i \cos(\omega_i t + \phi_i), \quad (1)$$

which is then fitted to the data in a least-squares sense by adjusting the constants a_i and ϕ_i . This method requires long records, typically greater than a year, in order to resolve some of the closely spaced constituents, and to provide statistical stability since weak tidal "lines" are often obscured by background noise. Also, the similarities in responses to given forcing are concealed in

the multitude of different amplitudes and phases. So it is not well suited to the analysis of short records.

In harmonic analysis, statistical stability is usually maintained at the expense of resolution. That is, averaging the spectra of many different pieces or realizations, or averaging across frequency bands in individual spectra reduces the ability to resolve different frequencies but improves the reliability of the spectral estimates (Bendat and Piersol, 1971). In analyzing short time series this problem is critical since the averaging procedure obscures spectral differences between adjacent frequencies. In tidal analysis, for example, fifteen days is the minimum record length that allows resolution of the principal lunar and principal solar constituents since these components differ by one cycle in fifteen days. Averaging spectral estimates over n frequency bands limits the resolving capabilities to signals which differ by n cycles in fifteen days. Thus, reliable estimation of the tidal constituents by spectral or harmonic techniques depends on the availability of fairly long term observations. If this criterion is not met the so-called "admittance approach" offers a viable alternative.

The method used to analyze the COBOLT data, the admittance approach, is described by Munk and Cartwright (1966). Basically, if one hypothesizes a linear, causal relationship between two time series, $x(t)$, which is termed the "input", and $y(t)$, which is termed the "output", the most general linear relationship between the two can be defined by the convolution integral,

$$y(t) = \int_{-\infty}^{\infty} x(t') h(t-t') dt', \quad (2)$$

where $h(t)$ is known as the impulse response function. Defining the Fourier transform by capital letters, i.e.,

$$F(\omega) = \int f(t) e^{-i\omega t} dt, \quad (3)$$

and taking the transform of equation (2) gives

$$Y(\omega) = H(\omega) X(\omega), \quad (4)$$

where $H(\omega)$ is the transfer function or admittance.

Since one rarely works with direct transforms, but rather with spectra, the following definitions are useful:

$$\text{AUTO-SPECTRUM} \quad S_x(\omega) = X(\omega) X^*(\omega) \quad (5)$$

$$\text{CROSS-SPECTRUM} \quad S_{xy}(\omega) = X^*(\omega) Y(\omega);$$

(where * indicates a complex conjugate) from which, using equation (4), it follows that

$$S_{xy}(\omega) = H(\omega) S_x(\omega). \quad (6)$$

If $x(t)$ is a periodic function, say

$$x(t) = a \exp i\omega t , \quad (7)$$

equation (2) assumes a particularly simple form

$$y(t) = H(\omega) x(t) . \quad (8)$$

This form is especially useful in generating the output function, since it is more easily computed than equation (2). It also reveals the conceptual basis of the admittance; it is a measure of the spectral linkage between the input and the output functions.

The primary advantage of the admittance analysis is the ability to reduce noise to well-defined levels without sacrificing resolution. This is accomplished by invoking the so-called "Credo of Smoothness" (Munk and Cartwright, 1966) which states that admittance amplitudes and phases are relatively smooth over broad frequency bands. This is based on the observation that the response of most physical systems does not change too abruptly if the frequency of the forcing or input is altered. Exceptions to this argument are systems that are being forced at close-to-resonant frequencies. The successful use of the admittance approach does not depend on a high degree of resolution because the admittance function varies so slowly with frequency that any structure in it can be discerned with short records or low resolution analysis. Because the input is generally a

well-known function for which long time series are available, high resolution analysis of output time series can be obtained from equation (8) once the form of the admittance function is known.

Instead of resolution and stability, the questions to be answered in the admittance approach center on the proper choice of an input function. The ideal input function is related so closely to the output that the admittances necessarily conform to the "Credo of Smoothness"; it is available (or can be constructed) for long enough time periods to allow the desired resolution; and, it is free of noise.

The analysis offers another important advantage. Because admittances are formed from ratios, they tend to divide out some of the numerical effects of the finite Fourier transform. This is again of interest in the processing of short time series where information from narrow frequency bands is spread out into relatively broad bands by the effective filtering of the transform process. Because the transform alters both the input and output functions in a similar manner, these effects are minimized with the use of the admittance.

Finally, the analysis provides a measure of how much of the output is coherent or phase-locked to the input. This measure is the squared coherence, defined as (Bendat and Piersol, 1971)

$$\gamma^2(\omega) = \frac{S_{xy}(\omega)^2}{S_x(\omega) S_y(\omega)} \quad (9)$$

That part of the signal which has random variations in amplitude and phase, such as weather fluctuations or intermittent baroclinic

effects, is summarily classified as noise. Ensemble averages of the admittances have, as a result, well-defined errors expressed in terms of the coherence. A particularly simple form for the variance of the real and imaginary parts of the admittance (which are distributed normally) is given by Munk and Cartwright as

$$V^2 = \frac{|H(\omega)|^2}{2N} \frac{1 - \gamma^2}{2}, \quad (10)$$

where N is the number of statistical degrees of freedom and γ is the true coherence.

Traditionally the equilibrium tide is chosen as the input function when analyzing short duration tide gauge or current meter data (see Filloux, 1971 and, Regal and Wunsch, 1973). The equilibrium tide, however, is computed from the tidal potential under the assumption that the earth is entirely covered by an infinitely deep ocean. It consequently does not account for variations that occur as the result of the presence of land masses and topography. In shallow, coastal waters it is well-known (Defant, 1961) that direct forcing by astronomical bodies plays only a minor role. The main forcing comes instead through interaction with the deep ocean tides at the continental shelf outer boundaries. Here the oceanic tidal currents are constricted by the rapid decrease in water depth and act through continuity to drive more energetic flows on the continental shelf than could be achieved through the action of direct astronomical forcing alone. (Further discussion of this subject is contained in the following chapter.) For this reason a series of coastal tide

height observations is presumably a much more appropriate input function for analysis of coastal tidal fields. So, following a procedure suggested by Cartwright, Munk, and Zetler (1969), a reference series computed from the tidal harmonics of a nearby tide station is used as the input function in analyzing the COBOLT data.

C. The tidal ellipse

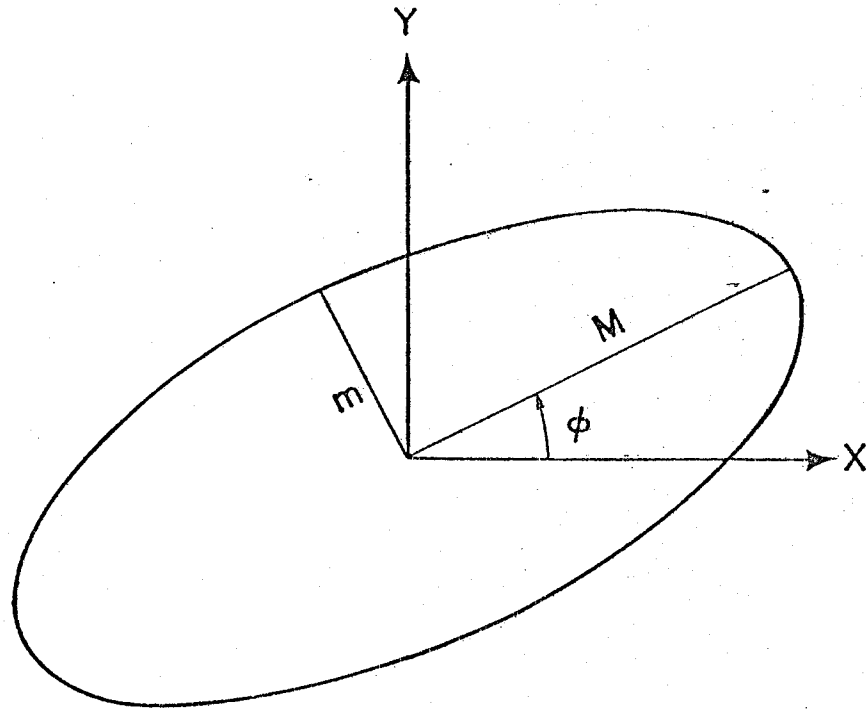
The presentation of the data is conveniently accomplished through the use of the tidal ellipse. Given the orthogonal velocities u and v , which are periodic with some frequency ω , the complex vector $u + iv$ can be formed. This vector may be decomposed into two constant, complex vectors A^+ and A^- , rotating in opposite directions: clockwise (-) and counterclockwise (+). Algebraically this is expressed as

$$u + i v = A^+ e^{i\omega t} + A^- e^{-i\omega t}. \quad (11)$$

These rotating vectors alternately add to, or subtract from one another producing the characteristic shape of the tidal ellipse. The phases of the vectors determine which direction the ellipse is oriented.

The parameters which succinctly describe the ellipse are the ellipticity and the orientation. They are illustrated in figure 1 and defined (respectively) by:

$$\epsilon = \frac{|A^+| - |A^-|}{|A^+| + |A^-|} \quad (12)$$



ELLIPTICITY

$$\epsilon = m/M$$

ORIENTATION

ϕ

TIDAL ELLIPSE

Figure 2-1 Definition sketch of the tidal ellipse

$$\phi = \frac{\arg A^+ + \arg A^-}{2} . \quad (13)$$

In geometric terms, the ellipticity is the ratio of the minor axis of the ellipse to its major axis. It is: positive if the complex current vector $u + iv$ rotates in a positive sense (counterclockwise); negative if the vector rotates in a negative sense (clockwise); equal to one if the vector traces a perfect circle; and equal to zero if the ellipse degenerates into a line.

The orientation measures the angle between the major axis of the ellipse and the positive x axis. (The x axis will point alongshore and the y axis onshore throughout this work.) It is constrained, by definition, to fall between $\pm 90^\circ$.

These quantities are introduced, not only to make the results easier to visualize, but as diagnostic tools for determining the dynamics of the tides. While the free surface co-phase (lines of constant phase) and co-amplitude (lines of constant amplitude) contours are valuable in this respect, the velocity field is quite sensitive to other dynamic (e.g., frictional) effects. This sensitivity is a consequence of the rotation of the earth which introduces ellipse characteristics that are peculiar to certain dynamics. Thus, it is advantageous to employ information from both surface and velocity fields in attempting any interpretations.

D. Tidal observations in the Middle Atlantic Bight

Under a common classification scheme which uses a ratio formed from the amplitudes of four prominent semidiurnal and diurnal constituents, the tides of the Middle Atlantic Bight are characterized as predominantly semidiurnal. This ratio (Defant, 1961),

$$\frac{K_1 + O_1}{M_2 + S_2}, \quad (14)$$

ranges from 0.19 at Sandy Hook, New Jersey to 0.33 at Montauk Point, New York, and averages about 0.25 for the Middle Atlantic Bight in general. The M_2 constituent is the largest; the ratio $M_2:S_2$ typically being about 5:1 (Shureman, 1958).

The Atlantic Ocean semidiurnal tide arrives everywhere at the edge of the continental shelf at roughly the same instant (Dietrich, 1944) and progresses with cophase contours paralleling the New Jersey-Delaware shore. To the north, the presence of Long Island Sound affects propagation characteristics markedly with its near-resonant response (Swanson, 1976). Cophase lines (see figure 2, taken from Swanson's work) bunch up around Montauk Point and distort normal tidal patterns many kilometers away from the Sound itself. As a consequence, the tide propagates to the east (towards the entrance to the Sound) along eastern Long Island and the west along central and western Long Island (in conformity to the rest of the shelf). The contours also show that the propagation pattern divides somewhere near the COBOLT region (station 20 on Swanson's map). Thus this area marks the transition between the tidal regime of the Bight and that

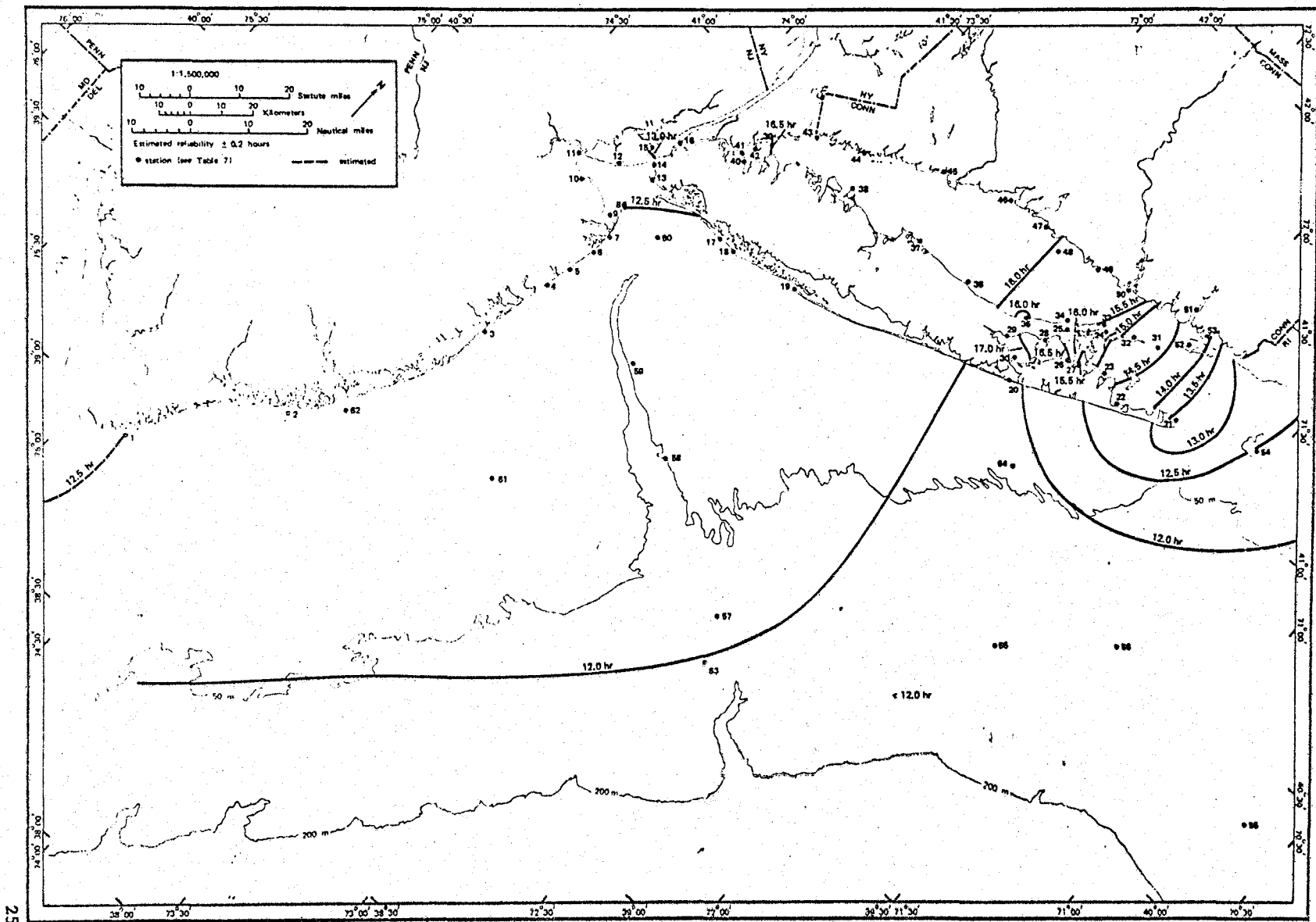


Figure 2-2 Cophase contours in the Middle Atlantic Bight (from Swanson)

Transverse Mercator Projection

of the Sound, and complicated interactions between the regions may be expected.

A crude estimate of the semidiurnal tidal wavelength, which will be valuable in the ensuing discussion, may be made by using the phase lags from the NOAA Tide Tables with the kinematic relationship between wave speed and wavelength,

$$\text{Wavelength} = \text{Phase Speed} \times \text{Period}. \quad (15)$$

These figures suggest that this wavelength is about 1500 km (Table 1).

The diurnal tides are not so well documented as the semidiurnal but seem to progress from north to south with compass contours perpendicular to the isobaths and coastline rather than parallel to them (Dietrich, 1944). In view of the lack of published information, it is difficult to characterize them except in noting that their propagation patterns differ noticeably from those of the semidiurnal constituents.

Tidal current measurements on the shelf, accompanied by the appropriate analysis, are generally sparse. Haight (1942) compiled current measurements from about fifty light ships on the East Coast in one of the earliest studies of tidal currents. Most of these lightships were located at the entrance to large harbors or on dangerous shoals and consequently are very complicated examples of nearshore tidal currents. Some general observations may be made, however. First of all, tidal ellipses are usually very elongated

TABLE 2-1

SEMIDIURNAL WAVELENGTH COMPUTATION

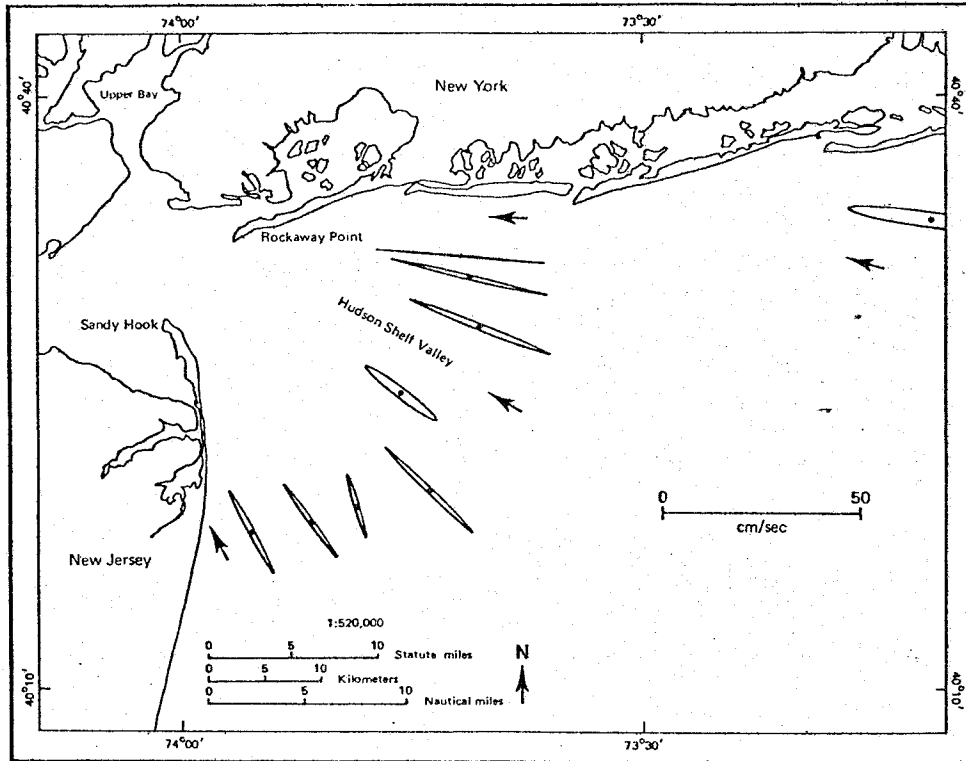
Guage Location	Distance from Sandy Hook	High & Low Water Interval		Phase Speed	Wave- length
Shinnecock Inlet	138 km	0.83 hr	1.13 hr	144 km/hr	1791 km
Fire Island	62	0.63	0.48	114	1413
Jones Inlet	39	0.32	0.45	104	1295

(the ellipticity is much less than one) at nearshore locations and more circular at offshore points. And, velocity vectors rotate almost exclusively in the clockwise direction; at 94% of Haight's observation points, according to Emery and Uchupi, 1972.

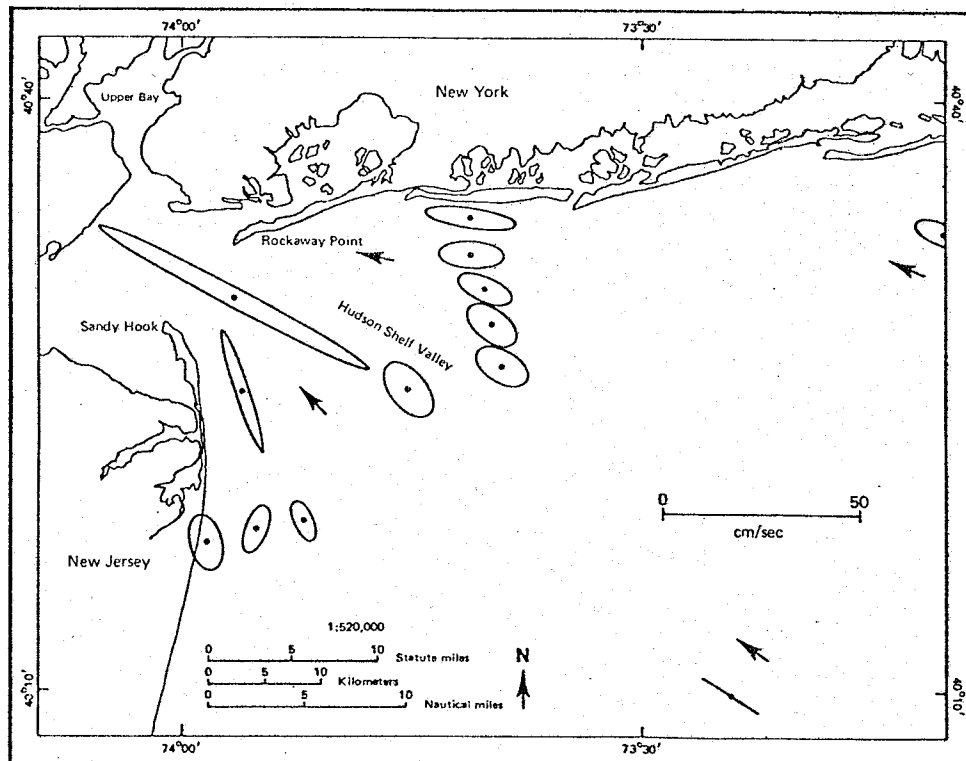
From measurements on the outer shelf, Flagg (1977) found that up to 50% of the total variance at individual current meters was due to the combined effects of diurnal and semidiurnal tides. Truschen (1976), using the same data set, notes that semidiurnal tidal ellipses are virtually circular and oriented in the cross-isobath direction, while diurnal ellipses are very elliptical and are oriented along isobaths.

Nearshore current measurements, such as those of Patchen, Long, and Parker (1976) in the New York Bight Apex, show the pronounced effects of a nearby shoreline, particularly if the measurements are not influenced by the presence of harbors or bays along that shore. If there is a solid boundary, onshore tidal velocities must be diminished to satisfy the boundary condition at the shore. This condition causes the tidal ellipses to elongate into very eccentric (low ellipticity) forms. Figure 3, taken from Patchen, Long, and Parker, shows the semidiurnal tidal ellipses from their experiment. In addition to the elongation of the tidal ellipses, it is noted that the major axes show a noticeable deviation from a shore-parallel orientation. Typically this orientation "tilt" angle is small--anywhere from 5° - 10° --and, it does not seem to correspond to any local topographic or shoreline features.

8 meters above bottom



3 meters or less above bottom



Rotation is predominantly clockwise at 8 m (26 ft) above the bottom, counterclockwise at 3 m (10 ft) or less above the bottom. The centers of ellipses are the station locations.

Arrows indicate direction of progress of the maximum M_2 flood current velocity. Current velocity vectors rotate 360° in 12 to 42 hours.

Source: From Patchen et al 1976

Figure 2-3
Tidal ellipses in the New York Bight

Mercator Projection

Other generalizations regarding the vertical structure of the tidal ellipses can be made from this experiment. It appears that ellipses near the bottom (3 m away) usually exhibit different ellipticities than those near the surface (here they are more circular in shape) and rotate, generally, in the counterclockwise direction. By contrast, tidal ellipses further away from the bottom (8 m) are almost always more eccentric and rotate in the clockwise direction.

Measurements near Little Egg Inlet, N. J. (EG&G, 1975), another coastal series available for comparison, are highly influenced by the presence of the inlet. This, as was the case with Haight's analysis, makes generalizations difficult. The experiment does show, however, predominantly clockwise rotation of tidal ellipses (with one exception) and emphasizes the point that large amounts of variance are due to the tides; 33% for year-long records in this case.

There appear to be few other relevant studies of nearshore coastal tidal currents in the Middle Atlantic Bight despite the increased interest in this region. Measurements which do exist usually focus on the lower frequency signal and neglect altogether mention of tidal phenomena. Work on other shelves (e.g. Petrie, 1975), while serving as a useful comparison, will not be pertinent to the Middle Atlantic Bight because of different deep ocean tidal forcing and topographic features.

E. Analysis of the COBOLT tidal signal

The first step in the analysis of the COBOLT data involved the choice of a reference tide station from which to generate the input time series for the admittance procedure. The station chosen was the tide gauge at Sandy Hook, New Jersey, approximately 140 km to the west of the COBOLT site. This is a reasonable choice if the COBOLT moorings are assumed to be in the tidal regime of the open shelf and not to be too closely related to that of Long Island Sound. It is also the closest one to have operated over the long period of time necessary to obtain stable values of tidal amplitudes and phases for the prediction. It has, in fact, been operational for more than a hundred years.

The tidal constants used to construct the reference time series were taken from Shureman (1958) and represent the results of harmonic analysis of ten years of data. The components employed are listed in table 2 along with appropriate periods, amplitudes, and epochs (the phase relative to the transit of the mean moon over the Greenwich meridian). Non-astronomical tides, such as those due to non-linear and radiational effects, and components with amplitudes that are less than 2% of the M_2 amplitude were ignored.

The input function generated was then subjected to the same procedures as were followed with the current meter data; i.e., overlapping data pieces 360 hours (15 days) long were used with a Fast Fourier Transform routine to give spectral estimates separated by 1/15 cycles per day. These estimates fall approximately on the

TABLE 2-2

TIDAL COMPONENTS OF
REFERENCE TIME SERIES

<u>COMPONENT</u>	<u>PERIOD</u>	<u>AMPLITUDE</u>	<u>PHASE</u>
K ₂	11.96723 hr	2.9 cm	243 deg
S ₂	12.00000	13.0	246
L ₂	12.19162	3.4	203
M ₂	12.42060	70.0	218
N ₂	12.65835	15.9	201
K ₁	23.93447	9.0	102
P ₁	24.06589	3.2	105
O ₁	25.81934	4.3	98

N_2 , M_2 and S_2 frequency bands for the semidiurnal portion of the spectrum, with adjacent estimates at 12.86 hr, 12.42 hr, and 12.00 hr; and approximately on the O_1 and K_1-P_1 bands for the diurnal, with estimates at 25.71 hr and 24.00 hr. The Fourier coefficients were hanned to reduce leakage of energy from the strong tidal lines into the weaker ones, and then used to form cross-spectral estimates between the reference series and the individual velocity components. The admittances for each 360 hr piece were then calculated according to equation (6).

Three types of averaging were utilized on the COBOLT data. Besides the standard practice of averaging cross-spectra over different pieces and across frequency bands, averages were taken among the COBOLT moorings themselves. This was done to reduce the effects of individual instrument errors and short record lengths on the results. Caution must be used in this enterprise since admittances are expected to show real horizontal variations due to the dynamic effects of topography and real vertical variations due to frictional and baroclinic influences. Unlike the other sources of error, these variations should be systematic and presumably subject to prediction. Examining the topography of the region (see chapter 1) suggests that horizontal variations should be small; especially for buoys 2-4 where the depth changes only 4 m in 6 km. So averaging instruments on different moorings seems acceptable provided the instruments lie in the same horizontal plane. Other errors and the presence of background "noise" are expected to swamp any real cross-isobath variations at these locations.

As mentioned before, parallel analysis was also performed on mooring 5 from the CMICE experiment. Since these experiments represent two different seasons--winter and spring--comparing them will provide a check for baroclinic effects. Also, the experiments will furnish a comparison between the CMICE instrumentation and the newer COBOLT instrumentation.

F. The results of the semidiurnal analysis

The presence of tidal frequency motions in the COBOLT data is exhibited by spectral analysis of the velocity time series. The spectrum of depth-averaged currents at buoy 2 is shown in figure 4. This averaging was done to isolate, to some extent, the true depth independent or barotropic velocities. The area beneath each frequency band is proportional to the contribution it makes to the total variance of the time series in this so-called "variance preserving" plot. In this case, the semidiurnal and diurnal tides combined, account for about 35% of the total energy observed in the "barotropic" velocities--a fairly typical proportion in coastal waters.

The admittances for the semidiurnal components are entered in table 3 for each of the instruments deployed. These have been averaged over three frequency bands covering periods from 12.00 hr to 12.86 hr, and over $T/360$ pieces, where T is the record length in hours at the buoy in question. Also included are the 95% confidence intervals computed from equation (10) and using the unbiased estimate of the true coherence,

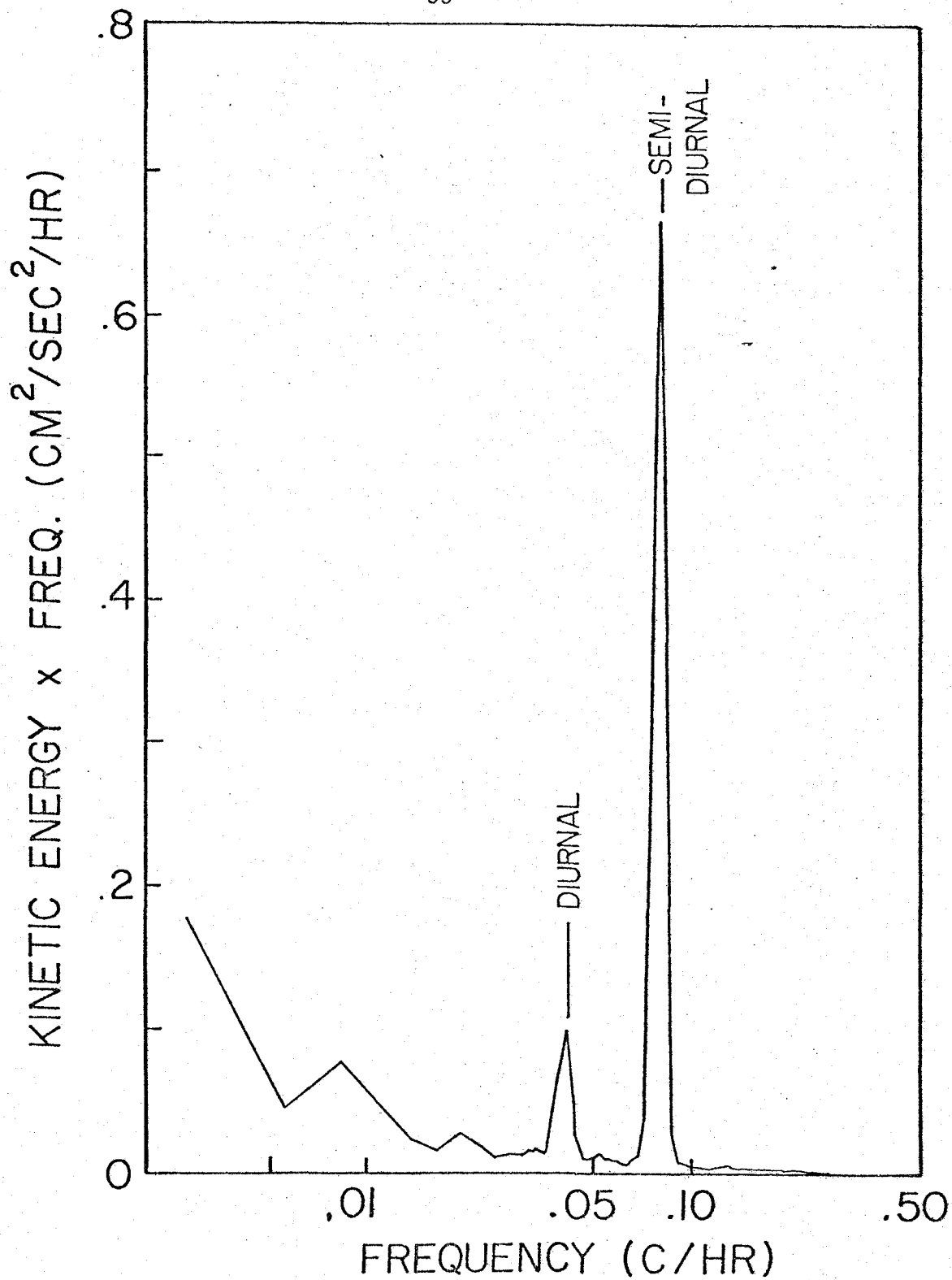


Figure 2-4 Variance preserving plot of kinetic energy of depth-averaged currents at buoy 2

TABLE 2-3

ADMITTANCE AMPLITUDES AND PHASES
FOR THE SEMIDIURNAL TIDE

<u>INST.</u>	<u>AMPL.</u>	<u>ERROR</u>	<u>PHASE</u>	<u>ERROR</u>	<u>COH.</u>
21N	0.058	0.019	-65	18	0.83
21E	.162	.017	58	6	.98
22N	.037	.015	-79	21	.78
22E	.153	.011	58	4	.99
23N	.053	.009	-110	10	.94
23E	.148	.010	47	4	.99
24N	.053	.013	-170	13	.90
24E	.095	.007	34	4	.99
32N	0.052	0.010	-85	11	0.92
32E	.154	.010	57	4	.99
33N	.052	.010	-92	11	.92
33E	.138	.012	50	5	.98
34N	.048	.005	-153	6	.97
34E	.106	.007	36	4	.99
41N	0.028	0.029	-44	46	0.55
41E	.153	.027	61	10	.97
42N	.039	.029	-15	37	.68
42E	.150	.027	65	10	.97
43N	.070	.014	-99	11	.96
43E	.122	.033	54	15	.93
44N	.052	.009	-152	10	.97
44E	.104	.018	30	10	.97
51N	0.047	0.009	-88	11	0.91
51E	.147	.016	53	6	.97
53N	.054	.016	-85	16	.85
53E	.184	.020	50	6	.97
54N	.036	.009	-150	13	.88
54E	.118	.015	40	5	.98

Quantities listed under ERROR are the 95% confidence limits of the admittance amplitude and phase.

COH is the true coherence of tidal currents with the reference series

$$\hat{\gamma}^2 = \frac{N \gamma^2 - 1}{N - 1}, \quad (16)$$

where N is, as before the number of degrees of freedom, and γ is the coherence estimate formed from equation (9).

While the number of degrees of freedom are fairly low (generally less than 12) due to the short record lengths, the coherences are high, especially for the alongshore components. As a consequence, statistical errors are kept to manageable levels. Onshore components, though much noisier, exhibit a certain stability (with the exception of instruments 41 and 42) that suggests that these numbers are also trustworthy.

Though longer records would do much to clear up doubts about the apparent discrepancies, the admittances exhibit some trends which are certainly reliable. Most noticeable is the disparity between the onshore and alongshore admittance amplitudes. This is a consequence of the adjustment of velocities to the presence of the shore and may partly cause the lower coherences evident in the onshore admittances since signal to noise ratios are presumably decreased also.

Vertical trends are also evident. Admittance amplitudes usually decrease towards the bottom, while phases decrease also--quite drastically for onshore components. This tendency is always most evident in the current meter that is nearest to the bottom and may indicate the presence of a frictional boundary layer.

Systematic differences between the May 1977 data and the February 1976 data are small despite the differences between the two experiments. Slightly larger admittances for the CMICE data and

slight discrepancies in phase might be noted, but all variations are well outside the resolving capabilities of the analysis and consequently cannot be argued with much certainty.

The semidiurnal tidal ellipse for each of the available instruments is shown in its appropriate location in figure 5 for the COBOLT moorings and in figure 6 for the CMICE mooring. The striking features of nearshore tidal flow are immediately apparent from these diagrams. The ellipses are all very eccentric but are not oriented parallel to the shoreline. Instead, they have a small but persistent negative inclination (-10° to -15°) which becomes more noticeable near the bottom. Moreover, the sense of rotation, which is clockwise for all shallow and intermediate instruments, reverses to counterclockwise for all bottom instruments.

Some of the ellipses have noticeably different characteristics from ellipses at the same level on other moorings, or from adjacent ellipses on the same mooring. Ellipses at two instruments already alluded to, 41 and 42, have slightly different orientations than other instruments, while the ellipse at instrument 21 appears to have a slightly different ellipticity. These discrepancies are probably a consequence of problems outlined in chapter 1 (i.e., instrument related errors).

Horizontal averaging provides a mean vertical profile of ellipse and tidal characteristics. The vertical profile of averaged ellipticity in figure 7, for example, shows plainly the characteristics described above. Ellipticities through most of the water column are

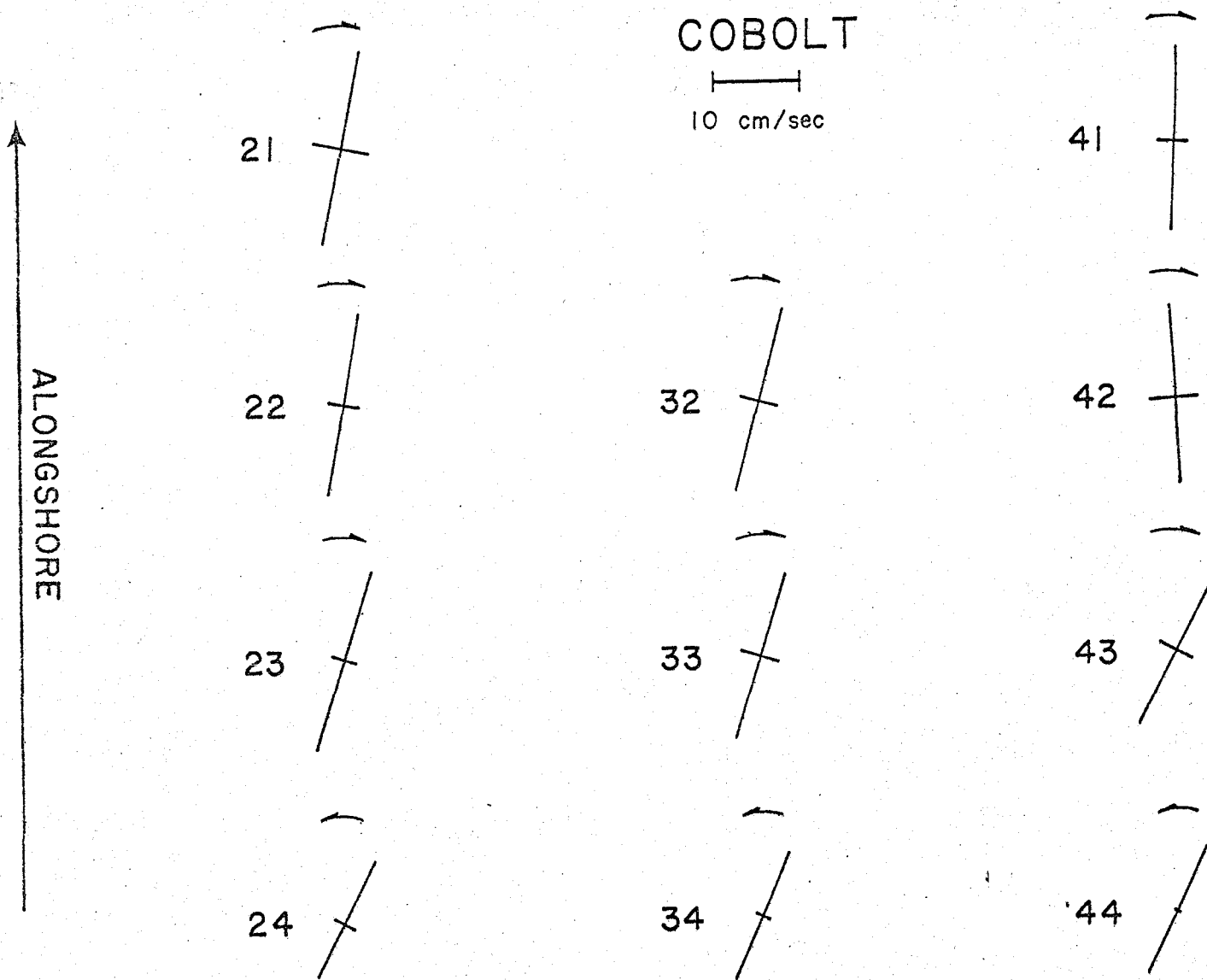


Figure 2-5 Semidiurnal tidal ellipses in the COBOLT experiment

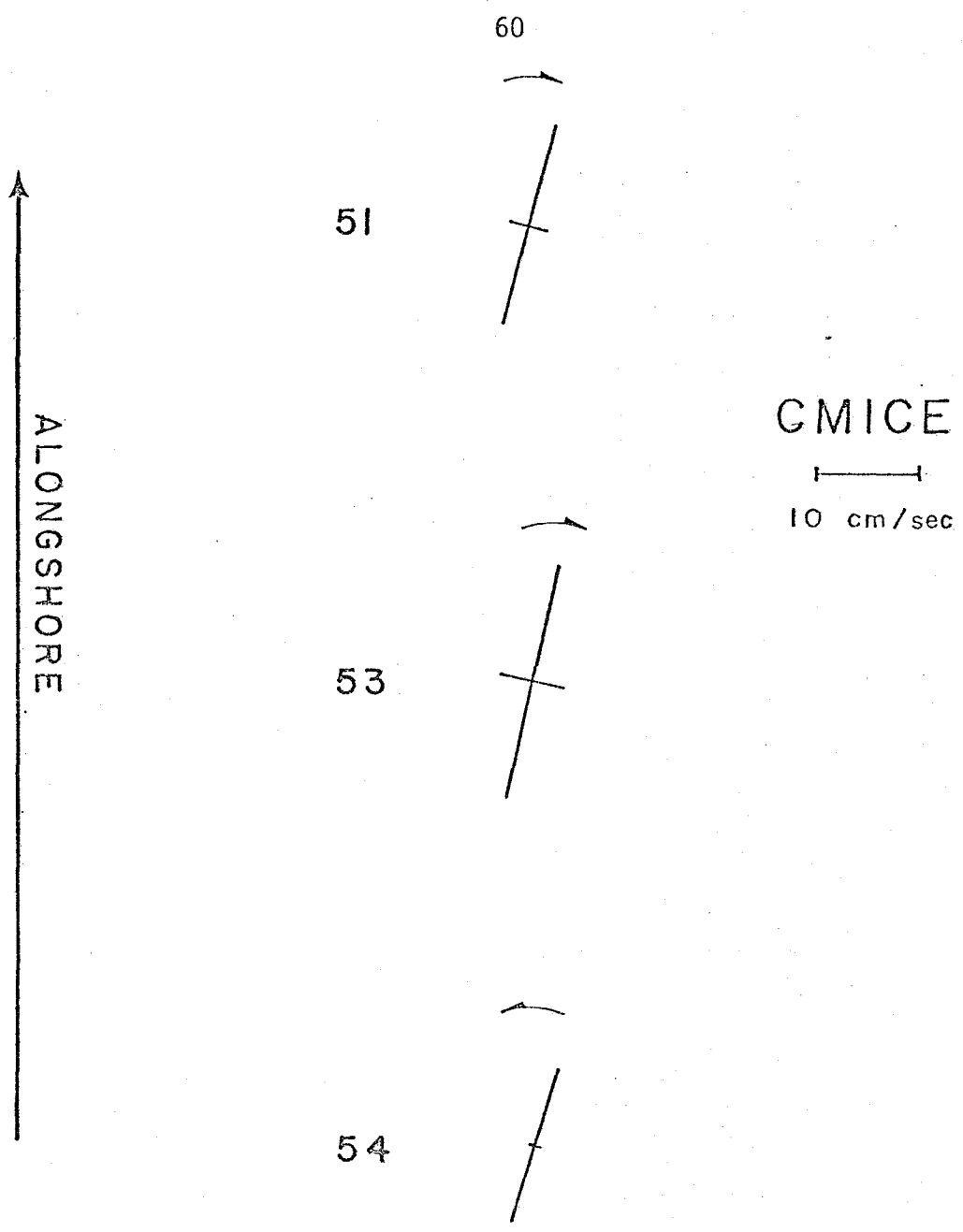


Figure 2-6 Semidiurnal tidal ellipses in the CMICE experiment

ELLIPTICITY

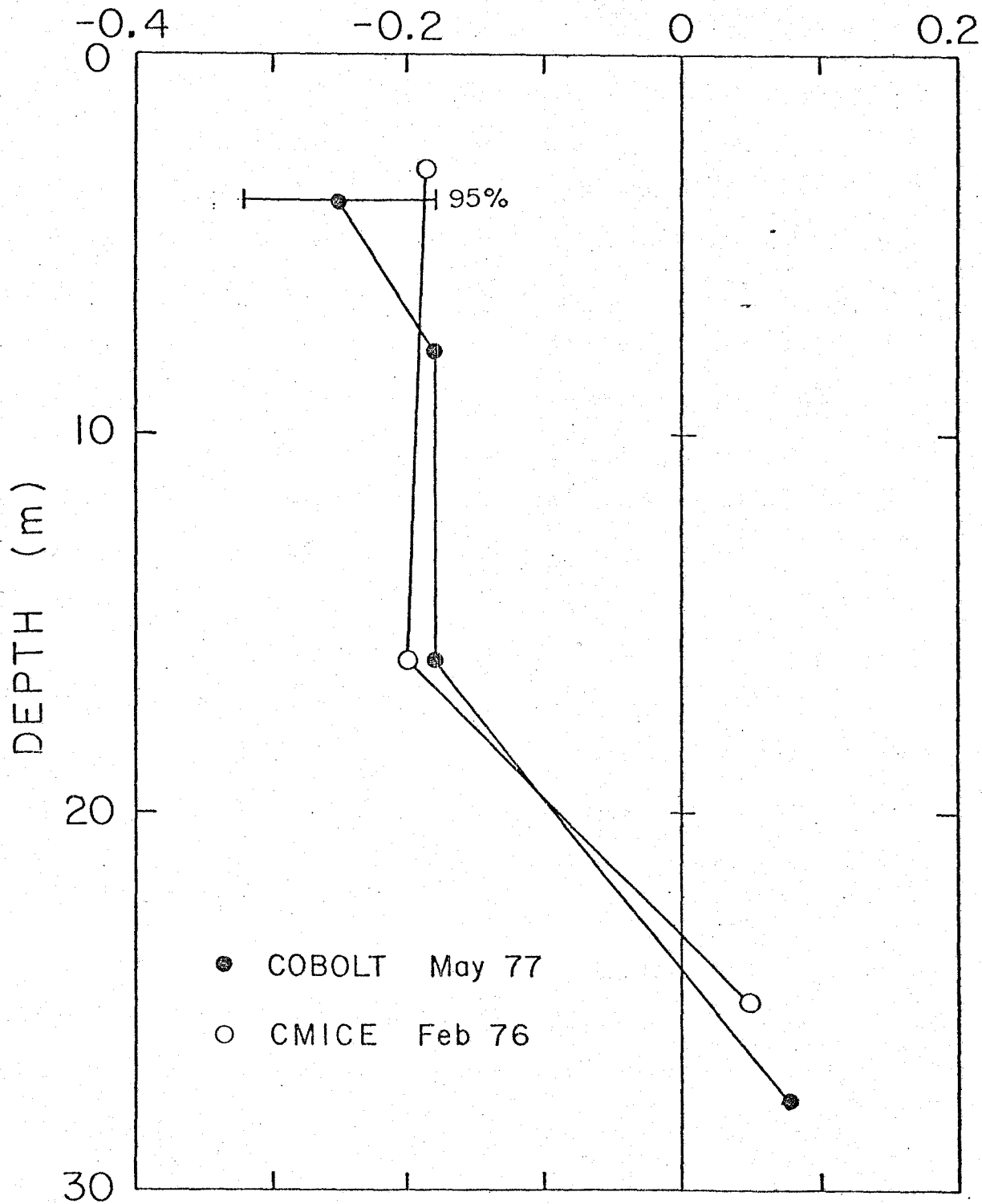


Figure 2-7 Vertical profile of semidiurnal ellipticity

constant and negative indicating clockwise rotation. These values change abruptly, however, somewhere between 16 m and 25 m below the surface. Ellipses near the bottom, in contrast to those above, have positive ellipticities indicating a change to counterclockwise rotation. Unfortunately, this feature is not well resolved and little can be said about the structure in the region where it changes most rapidly. Also from this diagram it is apparent that the agreement between the COBOLT and CMICE data sets is very good even though the ellipticity is subject to large errors because it is formed from a small difference of two large numbers (equation (12)).

The averaged orientation angle with respect to the alongshore direction (figure 8) has an almost linear trend with depth instead of changing suddenly. It is more homogeneous for the CMICE experiment than for the COBOLT experiment, though in view of the statistical uncertainties involved these profiles could be part of the same distribution. More importantly, the orientation angle is negative and significantly different from zero at all levels.

Figure 9 shows the vertical structure of the averaged kinetic energy. This energy was formed from the admittances by multiplying them by the 70 cm amplitude of the principal semidiurnal constituent, M_2 , at Sandy Hook. Also included is the energy from the harmonic analysis of a four day period when the stratification, and presumably the internal tidal oscillations, was strongest. The success of the admittance approach and averaging in eliminating much of the unwanted baroclinic signal is evident by the vertical uniformity of the

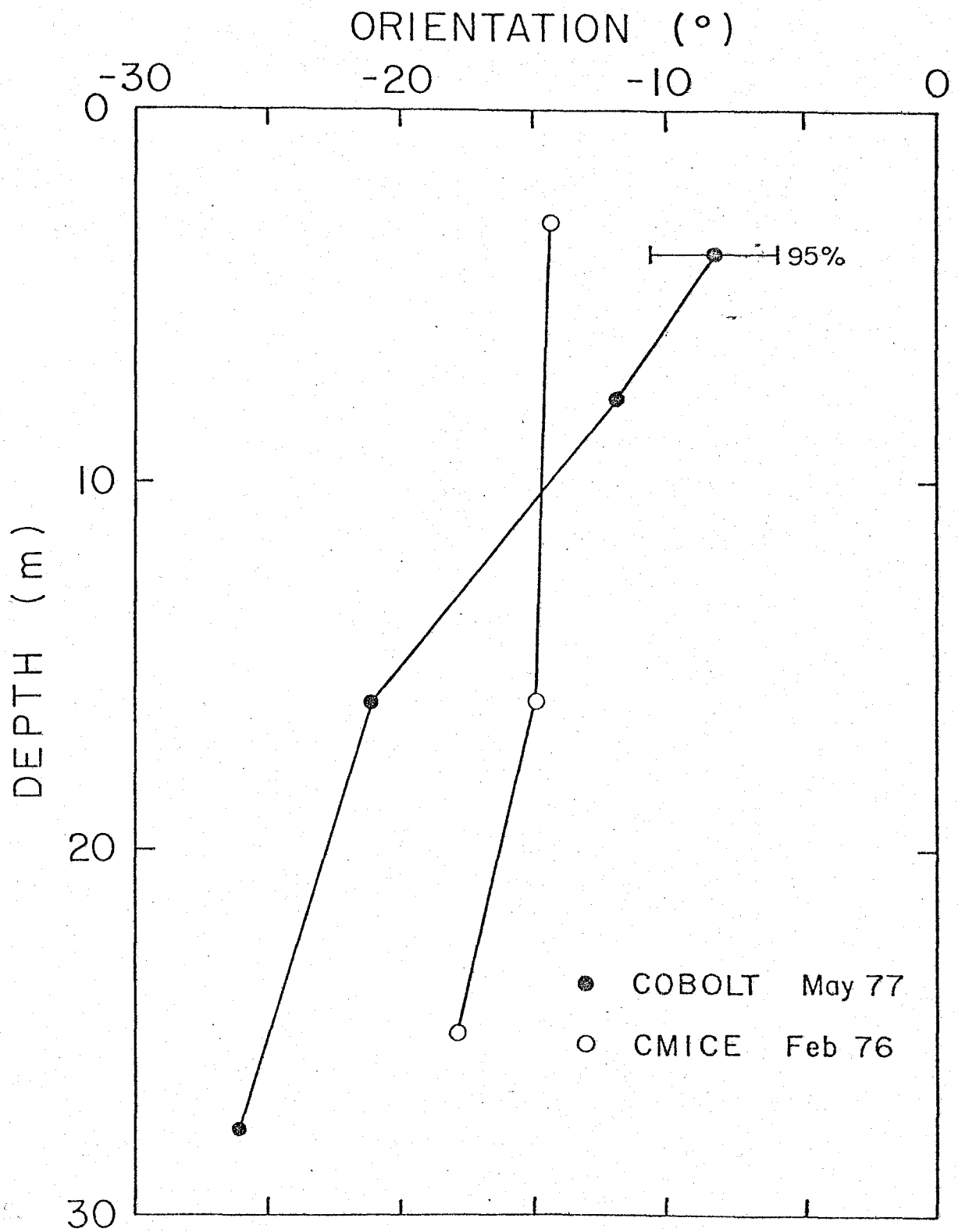


Figure 2-8 Vertical profile of semidiurnal orientation

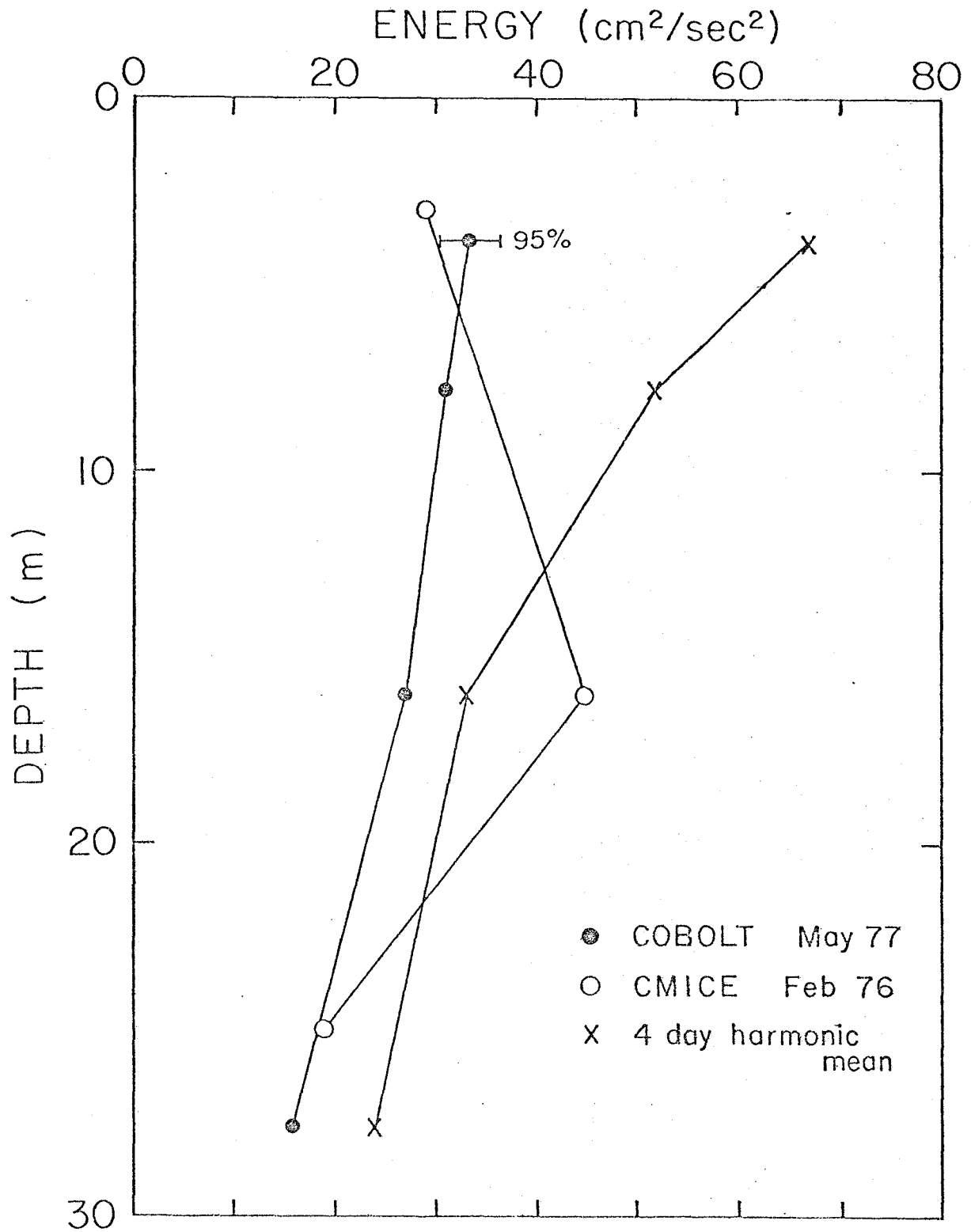


Figure 2-9 Vertical profile of semidiurnal kinetic energy

energy. The CMICE mooring does show some variability in the vertical structure, but this is most likely due to the fact that the surface instrument was not attached directly to the mooring but to a tethered spar. As a result, the top meter shows much less of the surface wave contamination common in conventional moorings and instrumentation.

In view of the homogeneity of tidal energy and the reasonably well-covered water column, it seems natural to form the "barotropic" ellipse by integrating the data vertically. Accordingly, the real and imaginary parts of the admittances were summed using the ordinary trapezoid rule to approximate integration. The velocity equations (using again the 70 cm tidal amplitude to convert admittances to velocities) are:

COBOLT (17)

$$u = 9.0 \cos (\omega t - 51^{\circ})$$

$$v = 2.8 \cos (\omega t + 102^{\circ})$$

and

CMICE (18)

$$u = 10.2 \cos (\omega t - 50^{\circ})$$

$$v = 2.9 \cos (\omega t + 99^{\circ}).$$

The depth integrated ellipses and their respective parameters are compared in figure 10. Although it is difficult to define the uncertainties of the integration procedure, the two ellipses seem to agree very well, further supporting the assertion that the barotropic

SEMIDIURNAL

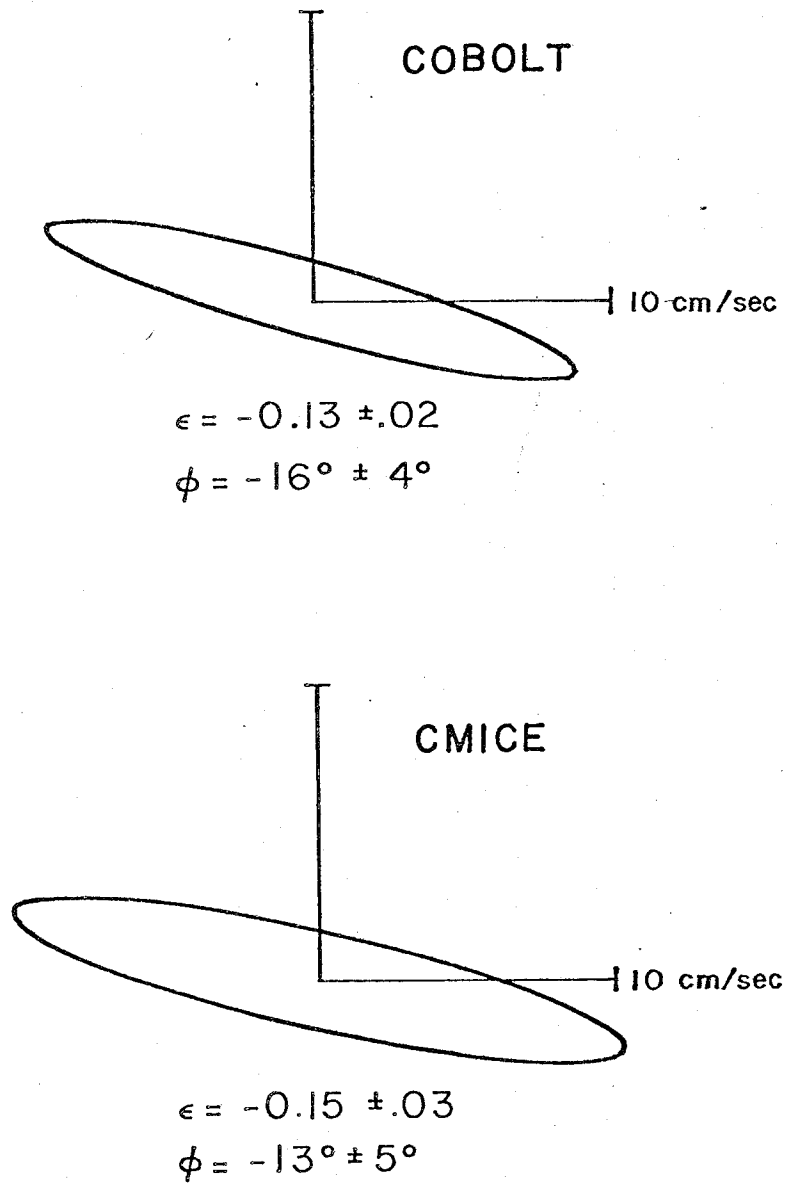


Figure 2-10 Semidiurnal ellipses for depth-averaged currents

tidal currents have been resolved and that the COBOLT spar mooring system has given accurate results. The figure also shows that the primary features of the mid-depth tidal ellipses are preserved in the depth averaged ellipses; i.e., they are significantly inclined to the local shoreline and depth contours, and they rotate in a clockwise sense. These features seem to be a part of the nearshore tidal regime and agree well with the MESA measurements of Patchen, Long, and Parker, 1976.

G. The band structure of semidiurnal admittances

The structure of the admittances across frequency bands has yet to be explored. This structure is expected to be fairly smooth. Certain conditions may alter this statement slightly. In the first place, the tidal height at Sandy Hook, while undoubtedly closely related to that at Shinnecock, probably contains fine differences due to such factors as distance from Long Island Sound or proximity to the Hudson River estuary. These differences are passed along in the admittances. Secondly, the amplitudes of the different constituents vary considerably; the amplitude ratio $N_2:M_2:S_2$, for example is about 17:70:13 cm. This implies more uncertainties in the less energetic constituents, which do not enjoy the high signal to noise ratio of the M_2 tide.

The admittances and phases for the three most energetic bands were obtained by depth integrating the real and imaginary parts of the admittance and then averaging the values for buoys 2-4. The

results, including ellipse parameters, are entered in table 4 and displayed in figure 11.

Both u and v admittance amplitudes tend to decrease with increased frequency. The phases of both components also tend to decrease as the frequency increases. These results, however, must be viewed with slight skepticism considering the magnitude of the errors. As far as the ellipse parameters are concerned the effects of frequency changes are most visible in the ellipticity which decreases dramatically with increased frequency. The orientation, by contrast, is totally unaffected.

H. The results of the diurnal analysis

Analysis of the semidiurnal band is much simplified by reason of its great energy content. The M_2 signal:noise ratio is in fact about 200:1. Furthermore, it contains almost 30% of the total variance observed. By contrast, the diurnal band has only about 5% of the total variance and its principal resolved component, K_1-P_1 , has a signal:noise ratio of only 4:1 in the COBOLT experiment.

As a consequence, the diurnal admittances are liable to have much more uncertainty associated with them. These admittances, averaged over the four frequency bands from 22.50 hr to 27.69 hr, are shown in table 5. It is apparent that the coherences are much lower than for the semidiurnal analysis, especially in the onshore components. In fact, coherences are not significantly different from zero (with 95% confidence) for most of the admittances of buoy 4 and for 3

TABLE 2-4

BAND STRUCTURE OF
SEMIDIURNAL ADMITTANCES

ADMITTANCE							
<u>PERIOD</u>	<u>COMP.</u>	<u>AMPLITUDE</u>		<u>PHASE</u>		<u>ELLIPT.</u>	<u>ORIENT.</u>
12.86 hr	U	0.137	.007	51	3	-0.19	-18 °
	V	0.051	.007	-96	7		
12.42	U	0.132	.005	51	2	-.13	-16
	V	0.041	.003	-102	5		
12.00	U	0.131	.009	48	4	-.10	-18
	V	0.045	.007	-113	9		

ADMITTANCE

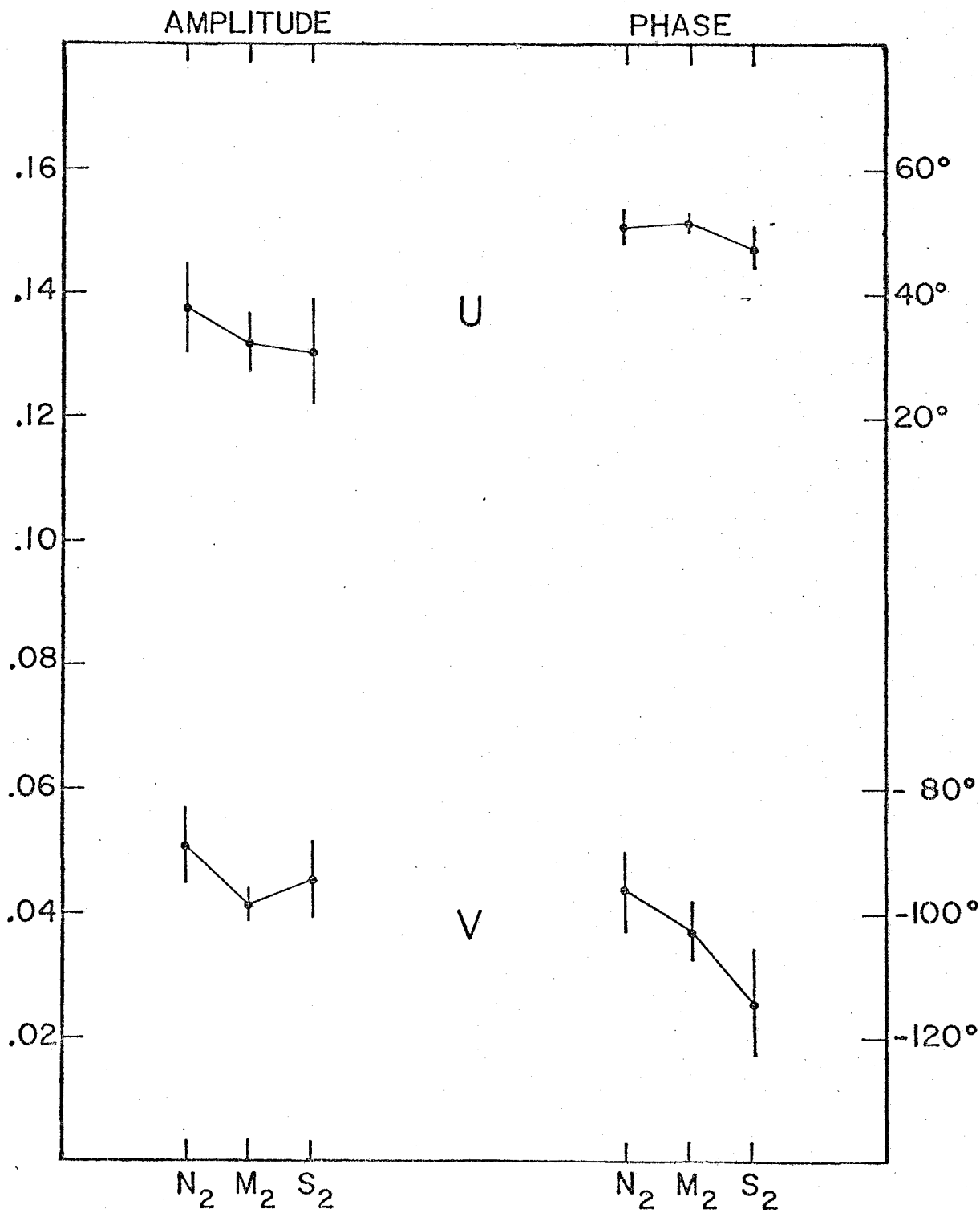


Figure 2-11 Band structure of semidiurnal admittances

TABLE 2-5

ADMITTANCE AMPLITUDES AND PHASES
FOR THE DIURNAL TIDE

<u>INST.</u>	<u>AMPL.</u>	<u>ERROR</u>	<u>PHASE</u>	<u>ERROR</u>	<u>COH.</u>
21N	0.16	0.09	-75	28	0.67
21E	.31	.10	42	18	.83
22N	.09	.06	-74	35	.58*
22E	.35	.13	51	20	.80
23N	.11	-	-122	-	.10*
23E	.37	.35	26	43	.46*
24N	.06	.05	59	37	.54*
24E	.23	.10	55	23	.50*
32N	0.19	0.10	-68	27	0.65
32E	.39	.07	44	11	.92
33N	.07	-	-53	-	.10*
33E	.34	.07	34	12	.90
34N	.10	.03	24	16	.84
34E	.24	.09	60	21	.75
41N	0.30	-	-144	-	0.26*
41E	.48	.08	1	10	.97
42N	.20	-	122	-	.00*
42E	.38	.10	25	15	.93
43N	.20	.09	-2	24	.84
43E	.43	.19	43	24	.84
44N	.17	-	26	-	.32*
44E	.33	.26	76	38	.66*
51N	0.17	0.08	-25	25	0.69
51E	.48	.19	47	21	.75
53N	.29	.12	-106	23	.72
53E	.44	.26	43	31	.59
54N	.15	.07	134	25	.69
54E	.17	.10	19	31	.59

Quantities listed under ERROR are the 95% confidence limits of the admittance amplitude and phase.

COH is the true coherence of tidal currents with the reference series

Starred coherences indicate that these quantities are not significantly different from zero at the 95% confidence level.

components on buoys 2 and 3. The CMICE mooring, with a greater number of degrees of freedom, shows significant, albeit low, coherence at all levels.

Because of the large uncertainties, components will not be considered separately but only as lumped diurnal admittances. The structure of the admittances is consequently lost (and with it the resolution) but useful information is still available from the band-averaged and depth-averaged admittances, just as in the semidiurnal case. This averaging, it appears, is essential for the diurnal admittances since it is the only way to achieve significant coherences.

The vertical structure of the diurnal ellipticity is shown in figure 12. Like the semidiurnal ellipticity it is negative at the surface and increases with depth. The COBOLT ellipticities, furthermore, never become positive and in fact remain less than -0.2 at all depths. This makes the diurnal ellipses more circular than the semidiurnal ellipses at all levels. Ellipticities at the CMICE mooring follow the COBOLT ellipticities at surface and middle depths but abruptly go offscale at the bottom. This is undoubtedly a spurious result.

COBOLT orientation angles (figure 13) progress almost linearly from large negative values at the surface to a positive angle at the bottom. By contrast, the CMICE mooring is non-monotonic and has roughly the opposite slope. These variations appear to be submerged in noise or influenced by non-barotropic effects. Large error bars indicate the consequences of the low coherence.

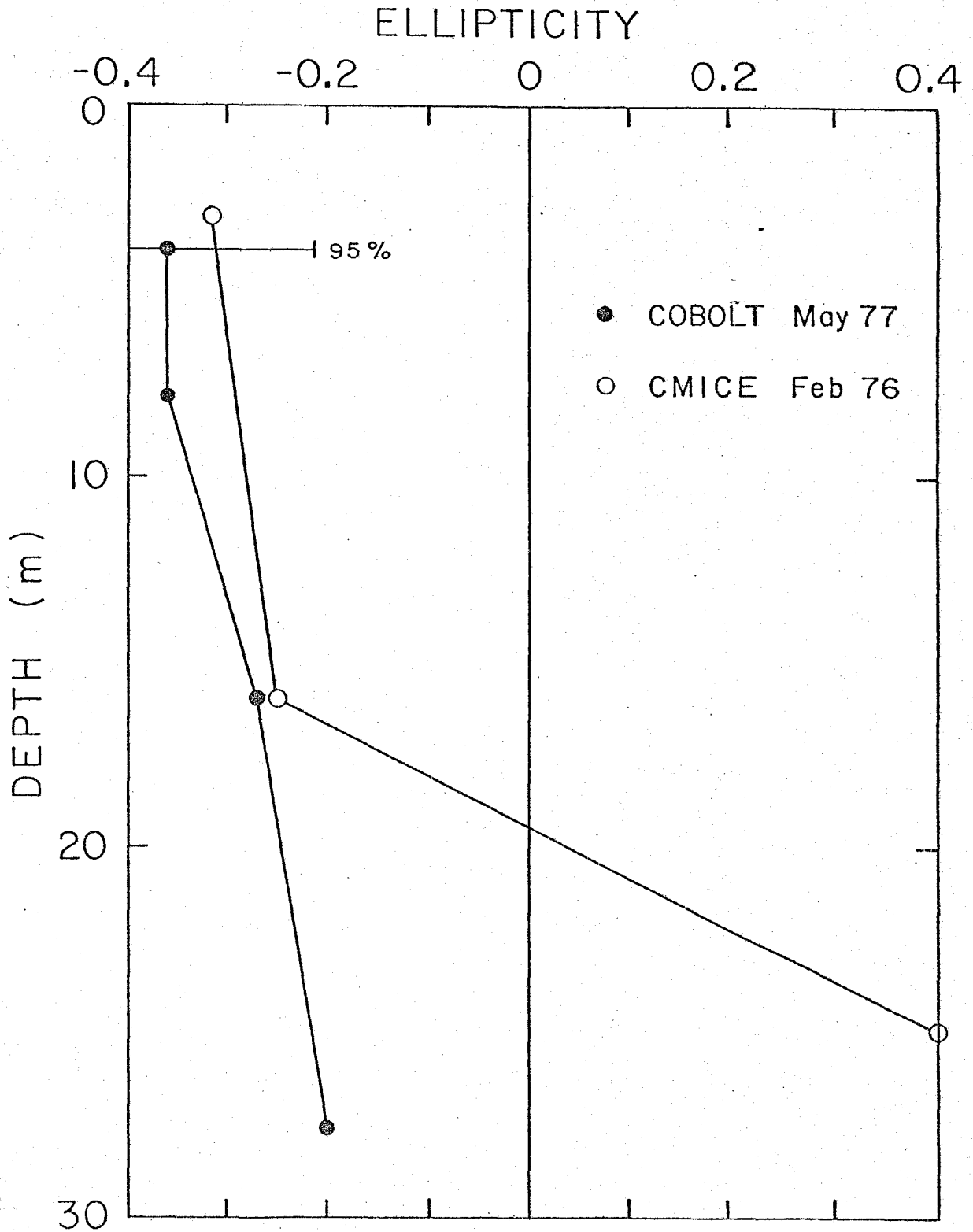


Figure 2-12 Vertical profile of diurnal ellipticity

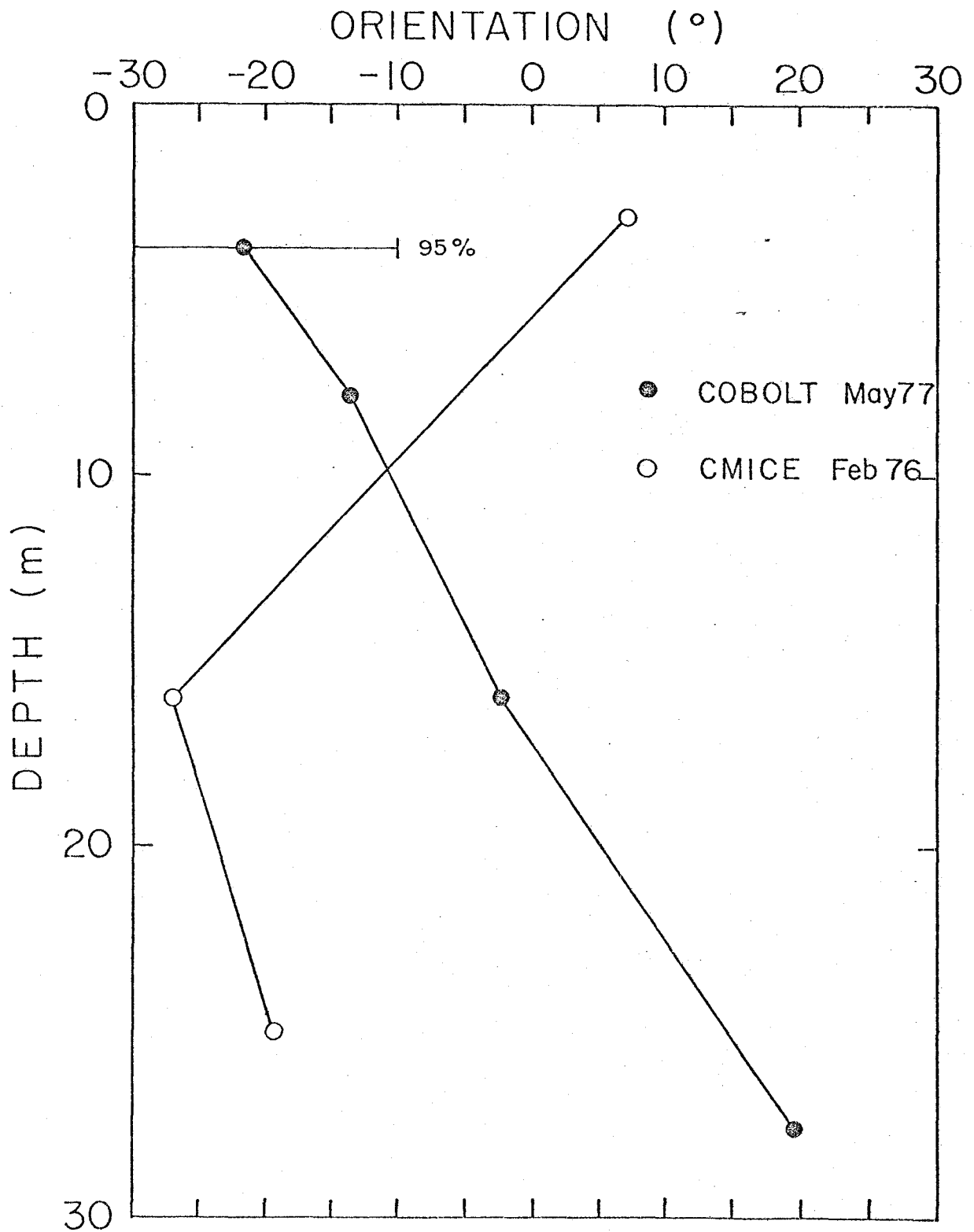


Figure 2-13 Vertical profile of diurnal orientation

The vertical distribution of energy (figure 14) shows almost constant values except near the bottom. The CMICE mooring energy decreases very sharply at the bottom instrument, again calling the result into question.

In spite of major differences in ellipse parameter distributions, the depth-integrated ellipses (figure 15) appear to be quite similar. Compared to the semidiurnal ellipse, the diurnal ellipse rotates in the same direction but is oriented at less of an angle to the shoreline and is slightly more circular. The velocity equations, with phases relative to Sandy Hook high tide, are:

COBOLT (19)

$$u = 3.5 \cos (\omega t - 40^\circ)$$

$$v = 1.3 \cos (\omega t + 80^\circ)$$

and

CMICE (20)

$$u = 3.7 \cos (\omega t - 42^\circ)$$

$$v = 1.1 \cos (\omega t + 90^\circ) .$$

I. Consequences and conclusions

It should be apparent by now that the main features of previous coastal tidal current observations in the Middle Atlantic Bight are also evident in the COBOLT data. The most prominent characteristics are the ellipticity (including sense of rotation) and the small, but non-zero orientation angle. The vertical structure of these

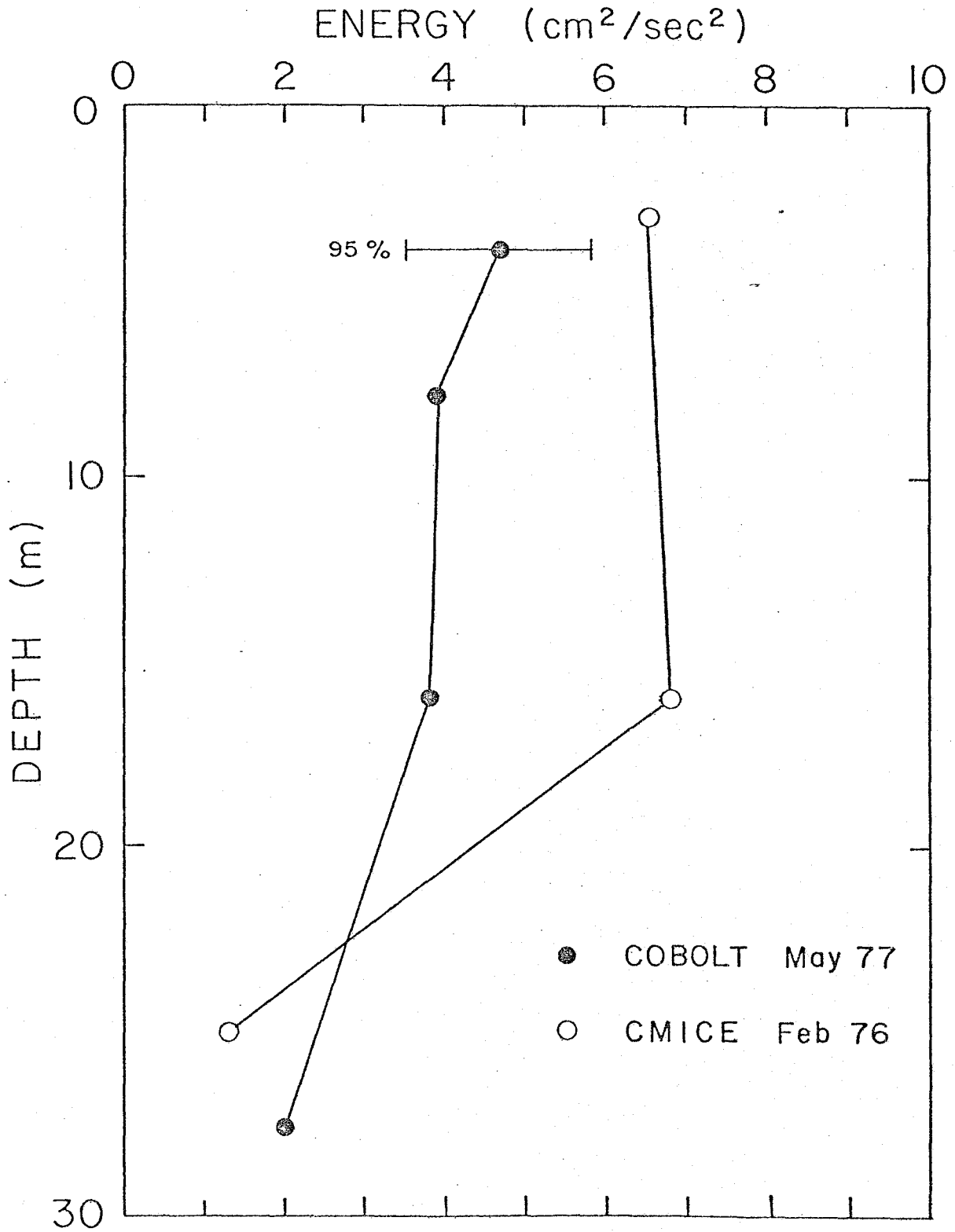
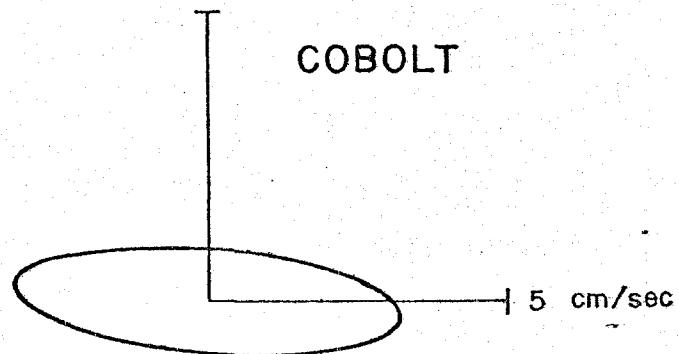


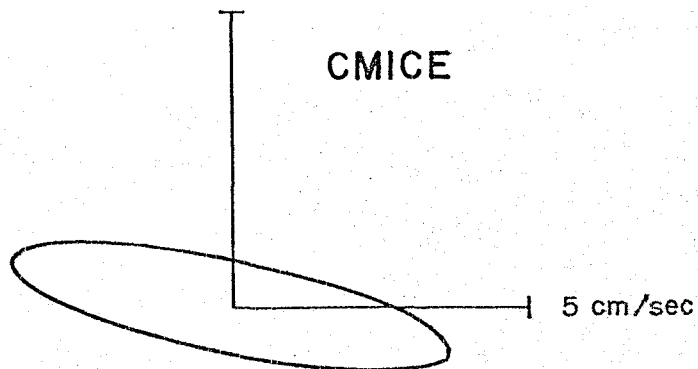
Figure 2-14 Vertical profile of diurnal kinetic energy

DIURNAL



$$\epsilon = -0.27 \pm .08$$

$$\phi = -5^\circ \pm 6^\circ$$



$$\epsilon = -0.20 \pm .11$$

$$\phi = -11^\circ \pm 8^\circ$$

Figure 2-15 Diurnal ellipses for depth-averaged currents

parameters is another feature that agrees qualitatively with other experiments.

A curious, and possibly related observation, concerns the presence of small scale, wave-like topographic features formed by loose-grain sediments. Swift, Duane, and McKinney (1973) have noted that, on average, the "crests" of these features form an acute angle with the shoreline of $22^{\circ} \pm 16^{\circ}$ in the Middle Atlantic Bight. It is certainly conceivable that tidal currents are responsible for these features and may account for their persistence. And, although it is difficult to argue persuasively that this swale topography is further evidence for the inclination angle of tidal ellipses, the possibility is rather intriguing.

These features seem, then, to be characteristic of the barotropic or surface tides of the nearshore region in the Middle Atlantic Bight. The depth structure of the ellipse parameters (particularly the energy profile) suggests that the time and buoy averaging, or the nature of the tide itself, have reduced the baroclinic tidal velocities to insignificant levels. Also, the comparison with the relatively unstratified conditions of February is good enough to support the conclusion that the barotropic tidal components have been resolved. Finally, depth integration has certainly reduced what baroclinic "noise" remained and has exposed the true barotropic tidal currents.

This is not to say that the internal tidal currents are unimportant or do not influence these calculations. This energy primarily

affects the barotropic admittances in manageable ways; namely by introducing low coherences into the measurements. This appears to be particularly true for the on-shore velocity components and for the diurnal tide--both of which show evidence of interference from baroclinic tides. Further discussion of this matter, however, is deferred until chapter 4.

The vertical structure of the ellipse parameters seems also to point to the importance of friction. The depth variations that do occur in the parameters are smooth (at least for the semidiurnal tides) and are accentuated near the bottom where frictional effects should be strongest. This matter will also be explored in more detail (chapter 3).

In terms of importance to continental shelf and coastal boundary layer dynamics, the most interesting and significant observation is that the depth-averaged tidal ellipse has a marked inclination to the shoreline. Such an inclination is indicative of shoreward transport of both energy and momentum. Since all the COBOLT moorings are within 12 km of shore, these fluxes are normally considered to be vanishingly small in order to conform to zero flux boundary conditions at the shore. This appears not to be the case, however.

The energy equation for long waves is obtained from the Laplace tidal equations (see chapter 3) by forming the vector dot product $\vec{h}\vec{v}$ with the momentum equation, and adding it to the product of g and the continuity equation. This gives the energy conservation equation,

$$\frac{1}{2} \frac{\partial}{\partial t} (\vec{v} \cdot \vec{v} + g\zeta^2) + g \nabla \cdot \vec{h}\vec{v} = 0, \quad (21)$$

or

$$\frac{\partial E}{\partial t} + \nabla \cdot \vec{F} = 0, \quad (22)$$

where E is the kinetic plus potential energy of the water column, and \vec{F} is the energy flux. Averaging over a wave period, indicated by brackets, $\langle \rangle$, gives the average tidal energy flux,

$$\vec{F} = gh \langle \zeta \vec{v} \rangle. \quad (23)$$

Before forming this product for the COBOLT data, the reference tide amplitude and phase must be shifted in some manner from Sandy Hook to Shinnecock Inlet. This shift to local tide is primarily in the phase and is rather tenuous due to the lack of tide gauge measurements in the Shinnecock area. Errors of as little as half an hour in estimating the phase can result in radically different directions for the energy flux. The calculation, however, is very revealing even if some errors are present.

Analysis by Swanson (1976) suggests that the tide offshore of Shinnecock Inlet precedes that at Sandy Hook by about 1.0 ± 0.1 hr (error inferred from Swanson), and that the M_2 tidal amplitude is about 50 cm. This amounts to a phase correction of $30^\circ \pm 3^\circ$ for the semidiurnal tide. Unfortunately, no such information is available for the diurnal tide. Despite the obvious shortcomings of this adjustment, these figures are used in obtaining a rough estimate of the tidal energy flux for the semidiurnal tide.

Noting the 30° phase correction in the free surface equation, (17) can be used with equation (23) to give the energy flux,

$$\text{Flux onshore} = 800 \pm 150 \text{ watts/m} \quad (24)$$

$$\text{Flux alongshore} = 1000 \pm 300 \text{ watts/m} .$$

The energy flux has a significant onshore component and an alongshore component to the east (towards Long Island Sound). Furthermore, the magnitude of the energy flux is quite large compared with shelf-wide estimates such as those of Miller (1966). Miller, using a frictional dissipation equation due to Taylor (1919),

$$E = C_d |\vec{U}|^3, \quad (25)$$

(with $C_d = 0.002$ and typical tidal current speeds), found that the energy flux on the eastern coast of the United States averaged less than 250 watts/m and was relatively unimportant on a world-wide scale. Though comparisons between this shelf-wide dissipation argument and the direct local flux calculation are difficult, the COBOLT calculations seem to indicate that Miller's values are an underestimate.

A more unusual fact is that the flux is so high at such a short distance from the shore. If a bottom friction mechanism similar to Taylor's is supposed, this rate requires tidal current amplitudes of 30 cm/sec shoreward of the COBOLT moorings--about three times higher than those observed.

Another candidate for this dissipation, Shinnecock Bay, has only the narrow (200 m) and shallow (5 m) inlet to admit energy. Even a gross overestimate of energy entering the bay, made by assuming that all the energy of the incoming tide is dissipated, results in an energy flux of only 10 watts/m at the COBOLT site.

It is possible that the flux can be accounted for by considering the divergence of alongshore energy flux. This supposition requires that the alongshore flux increase towards the entrance to Long Island Sound by roughly 100 watts/m for every kilometer closer to the Sound. While there is no direct evidence that might dispute a divergence of this magnitude, the dissipation rates in the Sound would have to be 5-10 times greater than are expected in order to accommodate the divergence.

As suggested, the alongshore flux is probably due to the presence of Long Island Sound. The large tidal currents of the Sound also imply relatively large dissipation rates. This flux does not mean that tidal currents at the COBOLT site are dominated by Long Island Sound tidal flow. Co-oscillating tides, such as those of the Middle Atlantic Bight, generate substantial velocities but transport little energy because of their standing wave characteristics.

The uncertainties of the flux calculations are absent in the evaluation of Reynold's stress terms due to tidal velocities. These depend only on the time averaged product of the velocity equations, (17) and (18).

For the semidiurnal tide, a phase difference of about 150° results in a momentum flux of

$$\langle uv \rangle = -13 \text{ cm}^2/\text{sec}^2 . \quad (26)$$

This is onshore transport of westward momentum and is very small in comparison with other forces if its divergence is uniform across the 10 km coastal region. The momentum flux does not show any divergence across buoys 2-4 (to within 6 km of shore), however, and may yet prove of significance very close to shore.

The diurnal momentum flux is an order of magnitude smaller than the semidiurnal flux and has the same sign. Although totally negligible, it makes an interesting comparison with Smith, Petrie, and Mann (1978) who found large momentum fluxes in both tidal components on the Scotian shelf. In contrast to the COBOLT measurements, the Scotian shelf semidiurnal and diurnal fluxes had opposite signs.

To summarize: with a few well-defined exceptions, the tidal analysis of the COBOLT data promotes considerable confidence in the performance of the COBOLT instrumentation in comparison with more conventional techniques. From a physical standpoint, the COBOLT experiment raises important questions concerning the proper flux boundary condition to be applied at the inner boundary of the continental shelf.

CHAPTER III

TIDAL DYNAMICS AND THEORY

A. Tidal dynamics

Theoretical interest in the tides dates back to Newton's development of the tidal potential which appeared in Principia in 1686. Although the potential did explain the origin of tide-producing forces, the real beginnings of the dynamic theory of the tides can be traced to Laplace; in particular to his Mechanique Celeste which appeared in 1799. So the subject is old, and enough work has been done that it is difficult to find a problem that has not been approached in some manner before (see e.g., Ferrell's (1874) discussion of non-linear bottom stress and tidal friction). Much of the early tidal theory is summarized in Lamb (1932), Proudman (1953), or Defant (1960), while more recent reviews, such as Munk and Hendershott (1970) and Hendershott (1973), emphasize the areas that are of concern to modern investigators.

A dynamic theory of the tides begins by considering the Eulerian equations of motion for a fluid in a rotating frame of reference. In their most general form they are (Krauss, 1973):

$$\left(\frac{\partial \vec{v}}{\partial t} + (\vec{v} \cdot \nabla) \vec{v} + 2\vec{\Omega} \times \vec{v}\right) = -\nabla p - \nabla \Phi + \nabla \cdot \vec{T} \quad (1)$$
$$\frac{\partial \rho}{\partial t} + \nabla \cdot \rho \vec{v} = 0,$$

where the symbols are defined as follows:

- ρ is the density of the fluid,
- $\mathbf{v} = (u, v, w)$ is the Eulerian velocity,
- $\vec{\Omega}$ is the rotation vector of the observer's frame of reference,
- p is the fluid pressure,
- Φ is the gravitational potential,
- \vec{T} is the stress tensor,

and the other quantities have well known meanings.

As they stand, these equations are much too difficult to solve and are traditionally simplified for application to tides on the earth. The usual approximations, which lead to the Laplace tidal equations, have been critically examined by Miles (1974) and will be used here with one exception--the fluid is not considered frictionless.

Basically, the important approximations and idealizations employed, and the modifications required of (1) are:

1. a homogeneous, incompressible fluid:

$$\frac{\partial \rho}{\partial t} + \vec{v} \cdot \nabla \rho = 0; \quad (2)$$

2. small disturbances relative to uniform rotation:

$$(\vec{v} \cdot \nabla)\vec{v} = 0; \quad (3)$$

3. a uniform gravitational field (which implies the neglect of tidal self-attraction);
 4. a rigid ocean bottom; and
 5. a shallow, or hydrostatic, ocean:

$$\frac{\partial p}{\partial z} = -\rho g. \quad (4)$$

This last simplification, known as the "traditional approximation" (Eckart, 1960), involves not only the neglect of vertical accelerations but also the neglect of the vertical Coriolis force due to the horizontal velocity. The omission of the latter term (and the approximation itself) has come under some attack (Phillips, 1966) but no specific instance has come to light where its use would be misleading.

In addition to the simplifications listed above, the nature of tidal dynamics on the continental shelf allows certain other simplifications. They are:

6. a plane earth coordinate system:

$$2 \vec{\Omega} = f \hat{k}; \quad (5)$$

7. retention of stresses on horizontal planes only:

$$\nabla \cdot \vec{T} = \partial \vec{\tau} / \partial z \quad (6)$$

where $\vec{\tau} = X \hat{i} + Y \hat{j}$; and,

8. the omission of direct tidal forcing:

$$\nabla \phi = 0. \quad (7)$$

The plane earth, or f-plane approximation is commonly used for modelling the dynamics of small scale oceanic phenomena. It is made after noting that the Coriolis parameter of a local Cartesian coordinate system on a spherical earth, $f = 2|\vec{\Omega}| \sin \theta$, varies slowly as a function of the latitude, θ . The ratio of the first two terms of the Taylor expansion of f around a given latitude forms the criterion for applicability of equation (5),

$$\frac{\Delta\theta}{\tan \theta} \ll 1, \quad (8)$$

where $\Delta\theta$ is a latitude increment and $R\Delta\theta$ is the length scale of the problem ($R = 6000$ km being the radius of the earth). A typical shelf dimension of 100 km, for example, gives (8) a value of about 2×10^{-2} for mid-latitudes.

According to equation (1), frictional forces in a fluid are a consequence of stress gradients. In the oceanic case, forces due to turbulent "stresses" are known to dominate forces due to viscous stresses (except possibly in very thin layers near boundaries). With the familiar Reynold's decomposition (Bowden, 1962) these turbulent forces are (in the x direction)

$$(\nabla \cdot \tilde{T}) \cdot \hat{i} = \frac{\partial \langle u'v' \rangle}{\partial x} + \frac{\partial \langle u'w' \rangle}{\partial z}, \quad (9)$$

where the bracket indicates a time average and the primes indicate velocity perturbations. Introducing a horizontal length scale, L , and a vertical length scale, H , the ratio of the terms on the right-hand side of (9), is

$$\frac{\langle u'v' \rangle H}{\langle u'w' \rangle L} \quad (10)$$

The validity of assumption 7 requires that this ratio be very small. For tidal waves on the shelf, $H = 100\text{m}$ and $L = 1000\text{ km}$, so $H/L = 10^{-4}$; while direct measurements show that $\langle u'v' \rangle = 10\text{ cm}^2/\text{sec}^2$ and $\langle u'w' \rangle = 1\text{ cm}^2/\text{sec}^2$. Thus, this criterion is met.

Finally, tidal phenomena on the shelf are generally assumed to be independent of the direct forcing of the tidal potential (Defant, 1960). They are instead generated by the inertia of the deep ocean, acting through continuity, at the edge of the continental shelf. The tides are then termed "co-oscillating" and are treated as freely propagating waves. The condition for the validity of this approximation is that

$$\frac{\nabla\phi}{g\nabla\zeta} = \frac{\nabla\eta}{\nabla\zeta} \ll 1, \quad (11)$$

where η is known as the equilibrium tide and is given by Lamb (1932) as

$$\eta = \frac{3}{2} \frac{M}{E} \left(\frac{R}{D}\right)^3 R \left(\cos^3\theta - \frac{1}{3}\right), \quad (12)$$

where M/E is the ratio of the mass of the moon to the mass of the earth, and R/D is the ratio of the radius of the earth to the distance to the moon. The gradient is typically

$$\frac{1}{R} \frac{\partial\eta}{\partial\theta} = \frac{3}{2} \frac{M}{E} \left(\frac{R}{D}\right)^3 \sin 2\theta = 5 \times 10^{-8} \quad (13)$$

for middle latitudes. A comparison of this quantity with the order of magnitude of the surface gradient made from estimates of the tidal wavelength ($\nabla\zeta = 10^{-6}$) indicates that the ratio (11) is small—about 0.05.

With the changes described above, and using the hydrostatic relation to replace the pressure with the free surface function, ζ , equation (1) reduces to the x and y momentum equations, and continuity:

$$\begin{aligned}\frac{\partial u}{\partial t} - fv &= -g \frac{\partial \zeta}{\partial x} + \frac{1}{\rho} \frac{\partial X}{\partial z} \\ \frac{\partial v}{\partial t} + fu &= -g \frac{\partial \zeta}{\partial y} + \frac{1}{\rho} \frac{\partial Y}{\partial z} \\ \frac{\partial u}{\partial x} + \frac{\partial v}{\partial y} + \frac{\partial w}{\partial z} &= 0.\end{aligned}\tag{14}$$

B. The vertical structure of tidal currents

To examine the effects of friction on the vertical structure of tidal currents, the stress must be related to the currents in some manner to close the set of equations (14). The form chosen,

$$\vec{\tau} = K_v \frac{\partial \vec{v}}{\partial z},\tag{15}$$

where K_v is a constant eddy viscosity, models turbulent effects in a well-mixed water column, away from boundaries.

It is apparent that the free surface, being independent of z , can be treated as a forcing function on the horizontal velocities in (14). This results in a "local" calculation of current structure for prescribed tidal height variations. Multiplying the second equation by i and adding the two, leads (including the stress parameterization (15)) to the single, complex, second-order equation,

$$\frac{\partial q}{\partial t} + i f q - K_v \frac{\partial^2 q}{\partial z^2} = P, \quad (16)$$

where $q = u + i v$ and

$$P = g \left(\frac{\partial \zeta}{\partial x} + i \frac{\partial \zeta}{\partial y} \right) = i \left((\omega + f) A^+ e^{i\omega t} - (\omega - f) A^- e^{-i\omega t} \right)$$

is the arbitrary forcing function expressed in terms that will relate it easily to the tidal ellipse (see chapter 2).

The solution to this equation can be expressed as the sum of a clockwise and a counterclockwise rotating solution,

$$q(z) = q_1(z) e^{i\omega t} + q_2(z) e^{-i\omega t}, \quad (17)$$

where

$$q_1(z) = C_1 \exp((1+i)z/d_1) + C_2 \exp(-(1+i)z/d_1) + A^+$$

for all ω , and

$$q_2(z) = C_3 \exp((1+i)z/d_2) + C_4 \exp(-(1+i)z/d_2) + A^- . \quad (18)$$

(using the plus sign for $\omega < f$ and the minus sign for $\omega > f$) with the integration constants C_n , and defining the parameters

$$d_1 = \sqrt{2 K_v / (\omega + f)} \quad d_2 = \sqrt{2 K_v / |\omega - f|} .$$

This problem has been treated before by Sverdrup (1926) and more recently by Butman (1975). The difference between the two analyses lies in the choice of a bottom boundary condition, which Sverdrup took to be non-slippery. From a physical standpoint, this condition does not model the turbulent boundary layer correctly. In order to account for the existence of the so-called "wall layer", Butman used instead a slippery boundary condition,

$$K_v \frac{\partial q}{\partial z} = r q \quad \text{at } z = 0, \quad (19)$$

where r is an adjustable drag coefficient. Both investigations used the same no-stress surface boundary condition

$$\partial q / \partial z = 0 \quad \text{at } z = H. \quad (20)$$

With these boundary conditions, equation (18) becomes

$$\begin{aligned} q_1(z) &= A^+ e^{i\omega t} \left(1 - \frac{r d_1}{K_v Q_1} \cosh(1+i)\left(\frac{z-H}{d_1}\right) \right) \\ q_2(z) &= A^- e^{-i\omega t} \left(1 - \frac{r d_2}{K_v Q_2} \sinh(1+i)\left(\frac{z-H}{d_2}\right) \right), \end{aligned} \quad (21)$$

where

$$Q_n = (1 \pm i) \sinh(1 \pm i)H/d_n + (rd_n/K_v) \cosh(1 \pm i)H/d_n$$

for $n = 1, 2$ and where the minus sign is used for $\omega > f$ and the plus sign for $\omega < f$.

The analogy to the ellipse equation (equation (11) of chapter 2) is seen clearly in equations (17) and (21). Indeed, for the case of

no bottom stress, (17) reduces exactly to the complex ellipse equation and shows that the forcing parameters, A^+ and A^- , can be identified with the frictionless, barotropic tidal current ellipse.

Because the forcing parameters are arbitrary in the "local" description, the actual numerical values of ellipticity and ellipse orientation are also arbitrary. However, it has been shown by Butman that the vertical structure of tidal ellipticity and orientation is independent of the forcing parameters A^+ and A^- . Thus the vertical structure of the ellipse parameters depends solely on the frictional constants, r and K_v ; a fact which was used by Butman to make estimates of these constants.

The vertical profiles of ellipticity and orientation are shown in figures 1 and 2 for values of the dimensionless quantities,

$$\gamma = r/fH$$

and

(22)

$$\Delta = \frac{1}{H} \sqrt{\frac{2 K_v}{f}},$$

that gave good visual fits to the observed semidiurnal profiles of the same ellipse parameters (presented in chapter 2).

These figures were made to correspond roughly to figures 7 and 8 of chapter 2 by adjusting Δ to match the observed thickness of frictional influence (Δ is actually the ratio of the Ekman layer depth to the total depth of the water column) and then varying γ to match

ELLIPTICITY

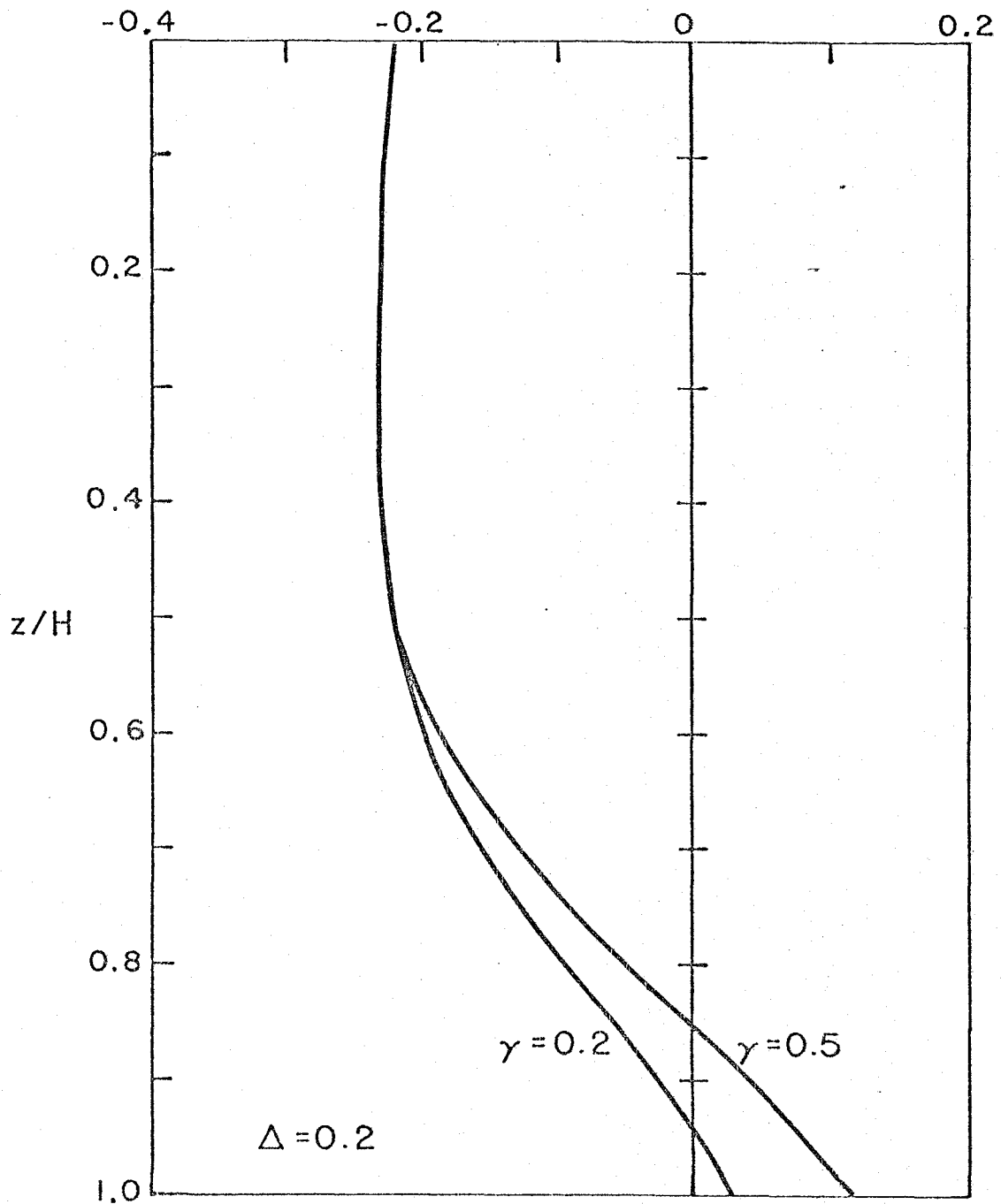


Figure 3-1 Theoretical vertical profiles of semidiurnal ellipticity

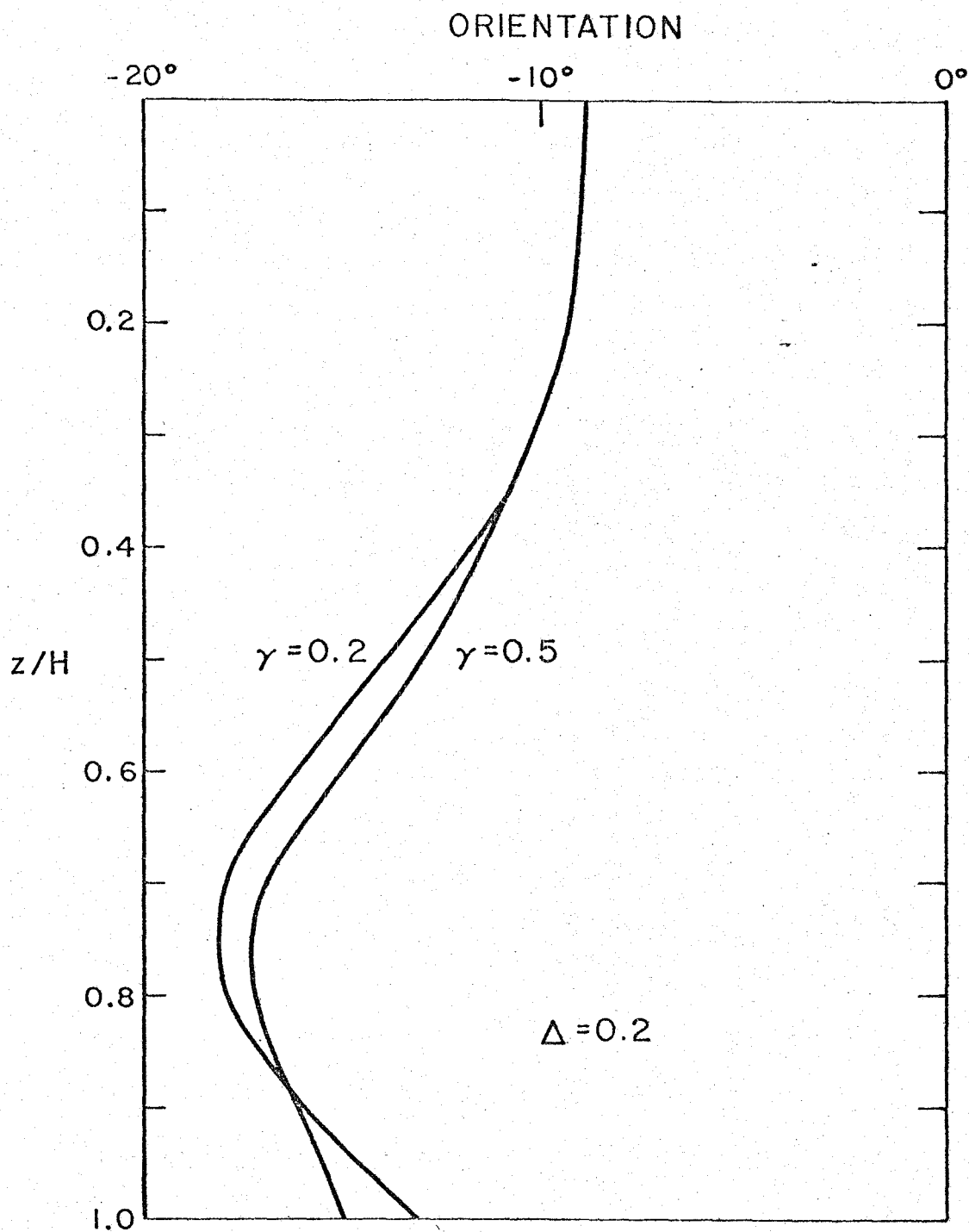


Figure 3-2 Theoretical vertical profiles of semidiurnal orientation

the range of values assumed by the ellipticity or orientation. It was found that large values of γ , which correspond (in the limit as γ approaches infinity) to Sverdrup's no-slip bottom boundary condition, result in excessively large ranges for the ellipse orientation and ellipticity. The actual observed range of this parameter supports the use of the slippery boundary condition (19).

The model reproduces the main features of the observations fairly well considering its simplicity. The ellipticity, for example, is constant near the surface and then changes rather sharply to higher values (currents can even rotate counterclockwise) near the bottom. The orientation has an almost linear slope towards negative angles as in the middle of the water column, but diminishes sharply near the bottom. Thus, it shows the effects of friction a little further away from the boundary than the ellipticity does.

Since the values of γ and Δ were chosen to fit the observed vertical structure of semidiurnal ellipticities and orientations, and since the actual values of these numbers were determined by judicious choice of the forcing parameters, A^+ and A^- , it may not be too surprising that the agreement between theory and observation is good. An independent test may be made, however, by applying the same values of γ and Δ to the diurnal tidal ellipse vertical structure. Figures 3 and 4 are these predicted vertical profiles.

The diurnal ellipticity profile is much like the semidiurnal, except that it has a slightly more gradual slope since the boundary layer is deeper for frequencies that are closer to inertial (see the

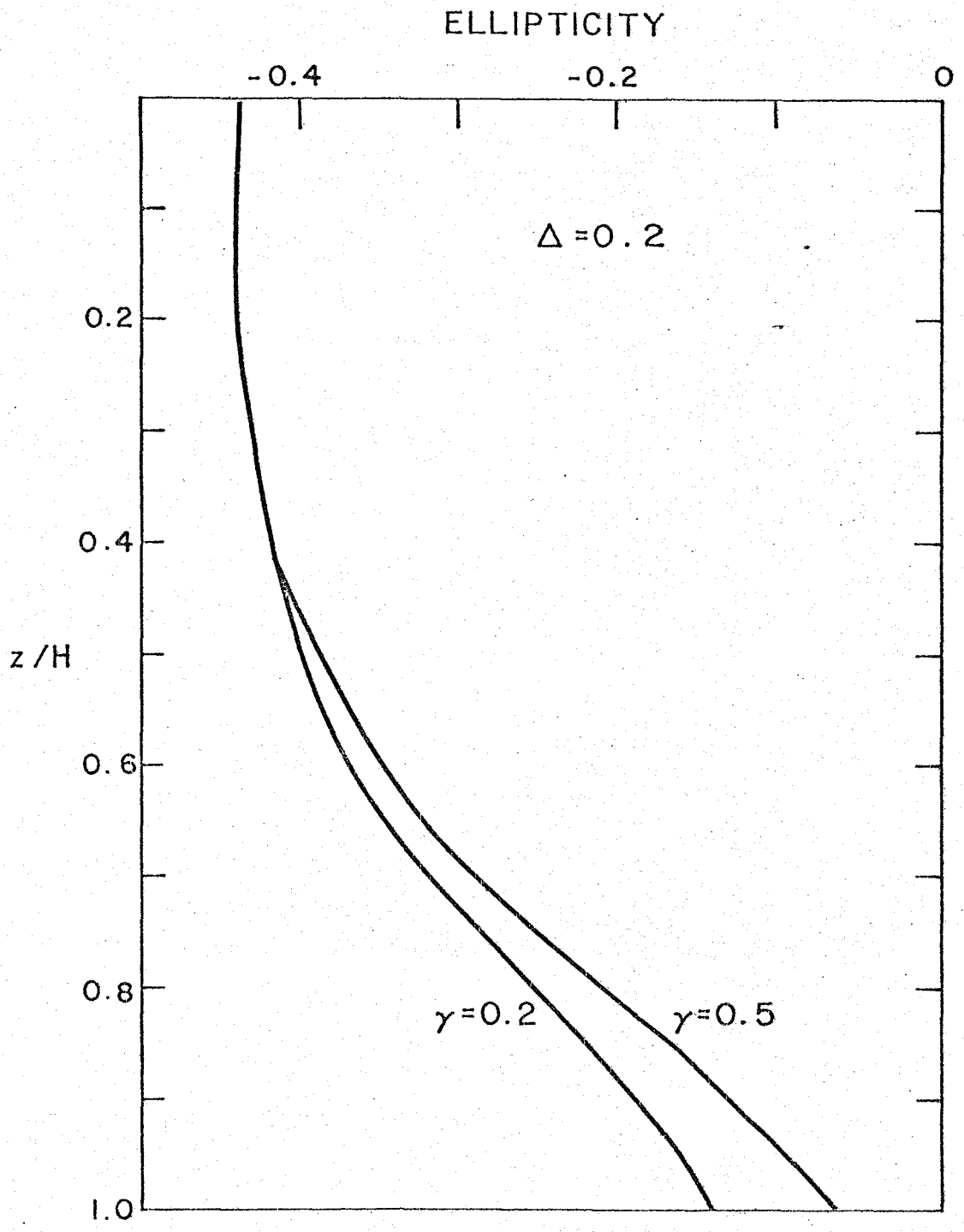


Figure 3-3 Theoretical vertical profiles of diurnal ellipticity

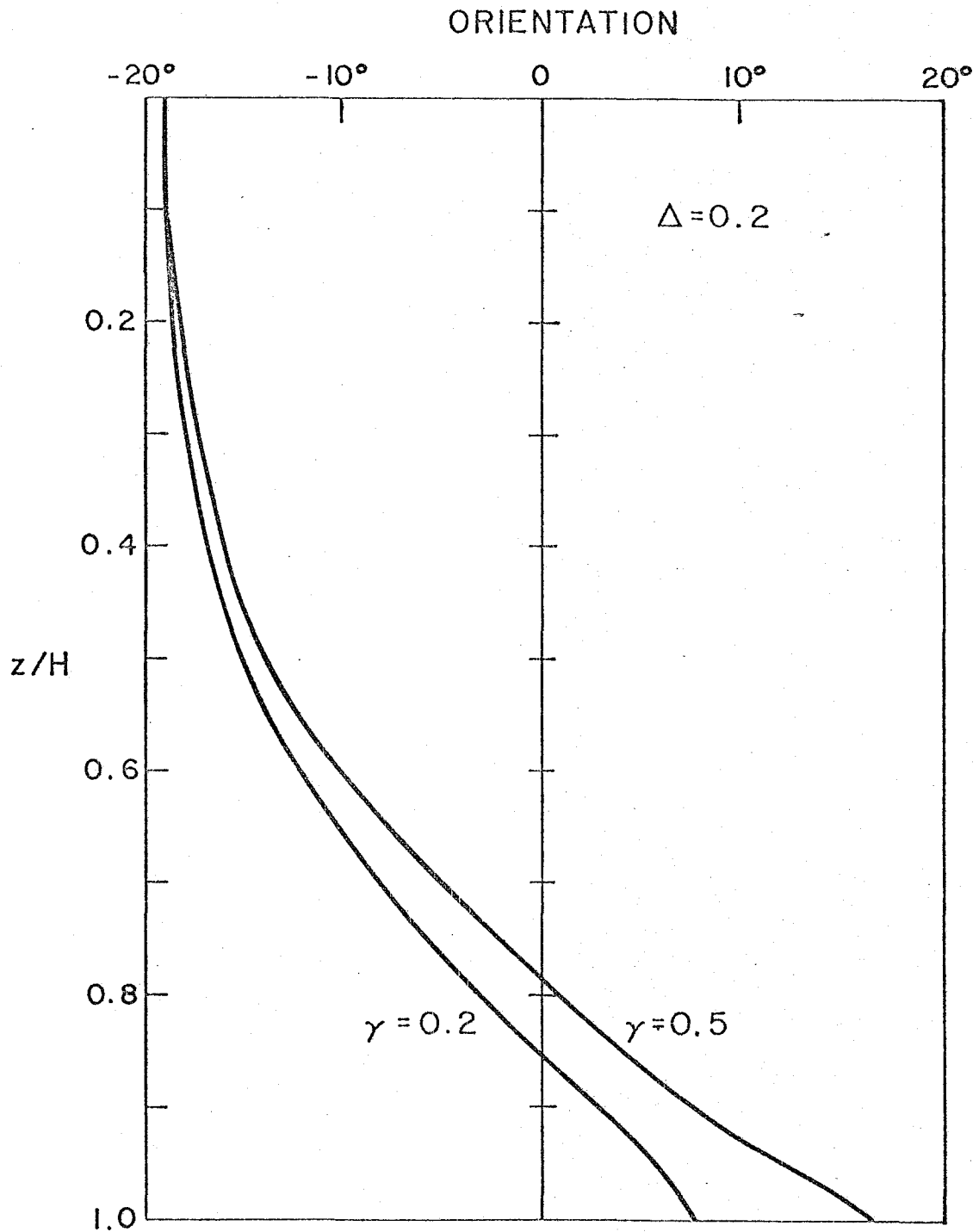


Figure 3-4 Theoretical vertical profiles of diurnal orientation

expressions for d_n following equation (18)). The diurnal orientation, on the other hand, is totally different at frequencies below f --it increases with depth rather than decreases. This opposite slope is exactly what is found in the COBOLT observations (figures 12-13 in chapter 2). The model also shows a greater range of orientation angles--again a feature that is found in the data.

Given the independent agreement between the constant eddy viscosity model and the COBOLT semidiurnal and diurnal frequency observations, it is reasonable to suppose that this model will also provide acceptable values of the friction parameters, K_v and r . Using the definitions of equation (22), the nominal depth of 30 m at the COBOLT site, and the range of values for γ and Δ that produced the best agreement with observations ($\Delta = 0.20 \pm .05$ and $\gamma = 0.4 \pm .1$) gives

$$K_v = 10-25 \text{ cm}^2/\text{sec} \quad (23)$$

$$r = 0.09-0.014 \text{ cm/sec} .$$

These values agree well with other estimates made in shallow water (see e.g., Butman, 1975). The value for r also agrees with an estimate made by Scott and Csanady (1976) at the COBOLT site using low frequency currents.

C. The effects of friction on tidal propagation

Besides affecting the local vertical structure of the tidal currents, friction also affects the global propagation characteristics of the tides (this "global" surface tide was impressed on the previous solution as the arbitrary forcing of equation (16)). While this subject has received considerable attention in the past, most investigators have ignored some of the basic conditions that are important in the coastal region; namely rotation and depth variations.

In general, friction acts as expected by attenuating waves in space or time, depending on the nature of the boundary or initial conditions. It also shortens the wavelength (Proudman, 1955). In shallow water, where the water column has less inertia and hence, less resistance to change, the effects of bottom friction are much more apparent. It is this largely ignored fact, the enhancement of frictional effects in shallow water, that is investigated here.

In order to explore the global structure of the tidal elevation field in the simplest terms, the vertically integrated versions of equations (14) will be used:

$$\begin{aligned}\frac{\partial u}{\partial t} - fv &= -g \frac{\partial \zeta}{\partial x} + \frac{B_x}{\rho H} \\ \frac{\partial v}{\partial t} + fu &= -g \frac{\partial \zeta}{\partial y} + \frac{B_y}{\rho H} \\ \frac{\partial \zeta}{\partial t} + \frac{\partial}{\partial x}(Hu) + \frac{\partial}{\partial y}(Hv) &= 0\end{aligned}\tag{24}$$

where

H is the depth of the fluid;

B is the bottom stress; and

u and v are the vertically averaged velocities defined by

$$\vec{v}(x,y,t) = 1/H \cdot \int_0^H \vec{v}(x,y,z,t) dz .$$

In direct analogy to equation (19), bottom friction will be taken as proportional to the depth-averaged velocity, i.e.,

$$\vec{B} = -r \vec{v} . \quad (25)$$

Although this form has some shortcomings (Rooth, 1972), it does introduce a dissipative mechanism, albeit a crude one, into the dynamics. Physically, velocities above the frictional wall layer should be used in (25). But for tidal oscillations, the depth-integrated velocities are a good approximation.

The equations can be solved quite simply if the depth is taken to be constant. The elimination of all variables except the surface elevation leads to the equation,

$$\left(\left(\frac{\partial}{\partial t} + \frac{r}{H} \right)^2 + f^2 \right) \frac{\partial \zeta}{\partial t} - gH \left(\frac{\partial}{\partial t} + \frac{r}{H} \right) \nabla^2 \zeta = 0 . \quad (26)$$

Rearranging this into frictional and non-frictional expressions gives

$$\begin{aligned} & \frac{\partial}{\partial t} \left(\left(\frac{\partial^2}{\partial t^2} + f^2 \right) \zeta - gH \nabla^2 \zeta \right) + \\ & + \frac{r}{H} \left(2 \frac{\partial^2 \zeta}{\partial t^2} + \frac{r}{H} \frac{\partial \zeta}{\partial t} - gH \nabla^2 \zeta \right) = 0 . \end{aligned} \quad (27)$$

Thus the equation separates neatly into two well-known forms. For small bottom friction or large depth, the familiar wave equation (upper part) governs the dynamics of tidal waves, while for large

friction or small depth, the dynamics are governed by the telegraph equation (lower part) which is known to have wave-like and diffusive solutions. In fact for the large friction-shallow water case, (27) reduces approximately to the parabolic partial differential equation,

$$\frac{\partial \zeta}{\partial t} - \frac{gH^2}{r} \nabla^2 \zeta = 0 \quad (28)$$

The scaling factor that indicates which dynamics are appropriate is $r/\omega H$. This factor is small at the COBOLT mooring site (about 0.2-0.4) but rapidly becomes important nearshore because of the decreasing water depth. Using $r = 0.1$, as inferred from the vertical structure, $r/\omega H$ reaches a value of unity in about 10 m of water. This point, which is about 1 km from the shore at the COBOLT site, marks the outer boundary of frictional dominance in depth dependent dynamics.

D. The Sverdrup-Poincare wave model

Analytical solutions of (24) are extremely complicated if both rotation and variable depth are retained in the model. To simplify, one must either make a choice between the two or try to model the frictional effects of shallow water in some other manner.

The obvious choice for an alternate model is a step discontinuity to simulate shoaling water. The geometry of this situation and the coordinate system that will be used is shown in figure 5. As envisioned, the deeper of the two sides is a region where wave dynamics dominate, and the shallower a region where the diffusive solution dominates (though this region is not examined in detail).

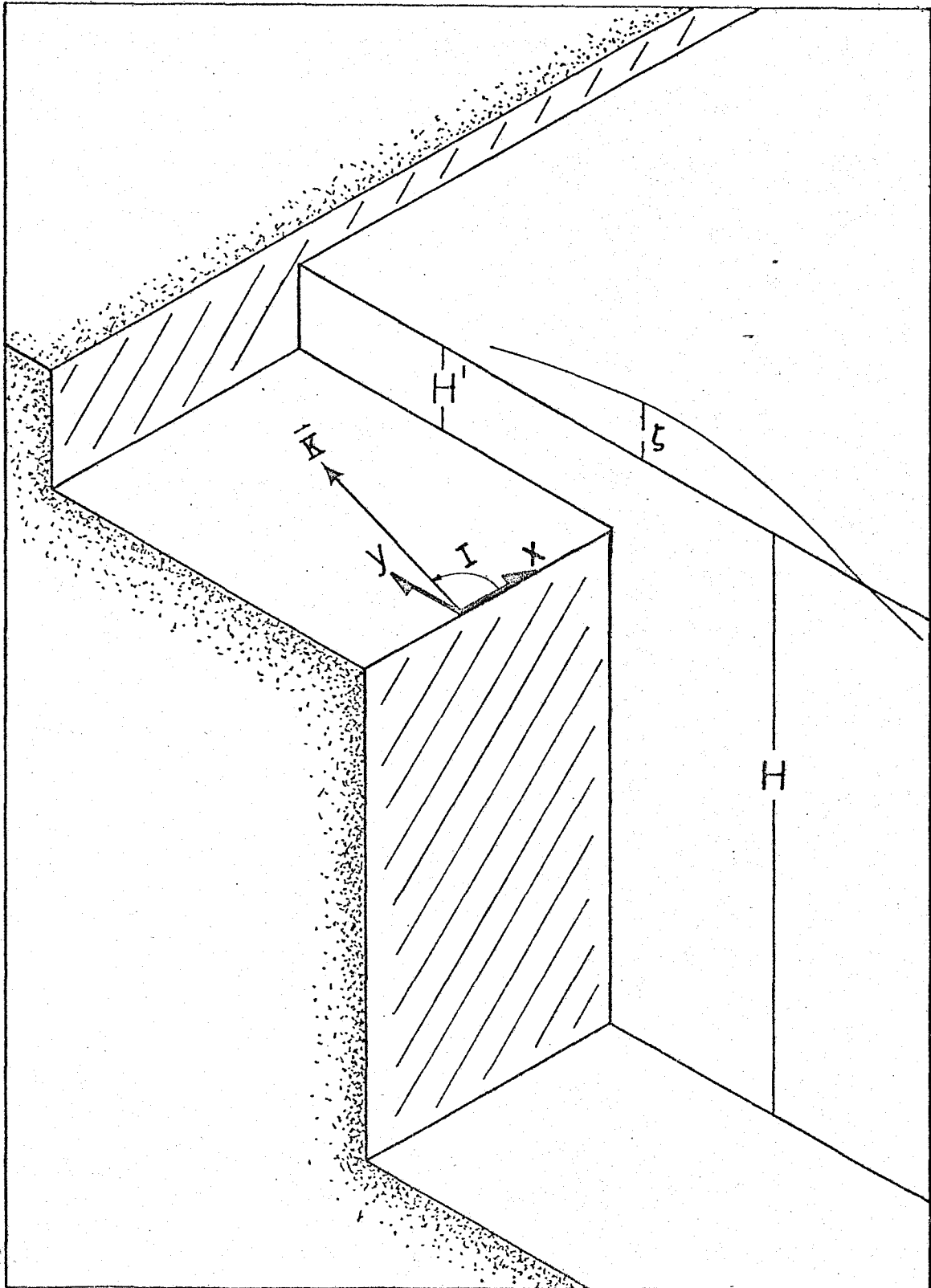


Figure 3-5 Geometry of the step shelf tidal model

In the deep region, this problem is posed in the same manner as the familiar wave refraction problem with the solutions formed from incident, reflected, and transmitted waves. The boundary conditions,

$$\zeta = \zeta' \quad \text{at } y = 0, \quad (29)$$

$$Hv = H'v'$$

determine the relationships between the various components. Because of the first condition, Kelvin waves, which travel only in the x direction (alongshore), must be excluded from consideration since they will decay in the shallow region but not in the deep, and a mismatch at the boundary will inevitably result.

The governing equation in the deep region is (from (24))

$$\left(\frac{\partial^2}{\partial t^2} + f^2\right)\zeta - gH \nabla^2 \zeta = 0, \quad (30)$$

with the velocity fields defined by

$$\left(\frac{\partial^2}{\partial t^2} + f^2\right)u = -g\left(\frac{\partial^2 \zeta}{\partial t \partial x} + f \frac{\partial \zeta}{\partial y}\right) \quad (31)$$

$$\left(\frac{\partial^2}{\partial t^2} + f^2\right)v = -g\left(\frac{\partial^2 \zeta}{\partial t \partial y} - f \frac{\partial \zeta}{\partial x}\right).$$

Assuming a solution consisting of an incident and a reflected wave,

$$\zeta = a (\exp i(kx+ly-\omega t) + R' \exp i(kx-ly-\omega t)), \quad (32)$$

where k and l are real wave numbers, and substituting it into equation (30), gives the dispersion relation for the elementary long

gravity wave in a rotating reference--the Sverdrup wave (Sverdrup, 1926):

$$\omega^2 - f^2 = gH (k^2 + \ell^2) . \quad (33)$$

The solution in shallow water is relatively unimportant since friction is assumed to absorb all the energy that is transmitted across the step. It must, however, have the same functional form in the x direction as the deep water solution. It is taken to be

$$\zeta' = T' \exp i(kx + \ell'y - \omega t) , \quad (34)$$

where ℓ' can be complex to allow for frictional attenuation away from the discontinuity.

Applying the boundary conditions, with the aid of equation (31) prescribes the relationships:

$$R' + 1 = T' \quad (35)$$

$$\frac{gH}{\omega^2 - f^2} (\omega \ell (R' - 1) + i f k (R' + 1)) = \frac{i g H' T'}{((r/H - i\omega)^2 + f^2)} (f k - (r/H - i\omega) \ell)$$

which can be solved for the complex amplitude of the reflected wave,

$$R' = \frac{HQ - H'Q'}{HQ^* + H'Q'} , \quad (36)$$

where

$$Q = \omega \ell - i f k$$

$$Q' = \omega \ell' - i f k .$$

Equation (36) can be reformulated into the more convenient form,

$$R' = (Q/Q^*) r' , \quad (37)$$

where r' will be called the "reflection coefficient" and is defined by

$$r' = \frac{1 - (H'Q'/HQ)}{1 + (H'Q'/HQ^*)} . \quad (38)$$

In the present context H'/H is presumed to be small in order to keep the absorption of energy to small values. In this case r' can be approximated to order $(H'/H)^2$ by

$$r' = 1 - 2 \frac{H' \text{Real}(Q)}{H |Q|^2} Q' . \quad (39)$$

In general r' is complex, but for small H'/H it can, for all practical purposes, be considered real since the imaginary part of r' is very small in this instance. For the case of no rotation, r' is real since both Q and Q' become real. Also, r' is less than unity for $H' < H$, indicating an absorbing boundary.

Replacing R' in equation (32) with equation (37) gives the wave solution,

$$\zeta = \frac{a}{Q^*} (r'Q e^{-i\lambda y} + Q^* e^{i\lambda y}) e^{i(kx - \omega t)} \quad (40)$$

and the velocity distributions,

$$\begin{aligned} v &= \frac{ag|Q|^2}{\omega^2 - f^2} \frac{1}{Q^*} (r' e^{-i\lambda y} - e^{i\lambda y}) e^{i(kx - \omega t)} \\ u &= \frac{ag}{\omega^2 - f^2} \frac{1}{Q^*} (r'SQ e^{-i\lambda y} - S^*Q^* e^{i\lambda y}) e^{i(kx - \omega t)} , \end{aligned} \quad (41)$$

where

$$S = \omega k - ifl.$$

These solutions consist of incident and reflected Sverdrup waves whose elementary characteristics are well-known but are seldom invoked as an explanation of tidal phenomena. The ellipse characteristics are easily examined from equations (40) and (41).

This boundary condition bears a close relation to one proposed by Proudman (1941) in an attempt to model the dissipative effects of the continental shelf as a boundary to the deep ocean. The Proudman boundary condition,

$$v = \alpha \zeta \quad \text{at } y = 0, \quad (42)$$

takes the place of the boundary conditions (29) and has been used in some of the numerical models of the deep ocean tides (Hendershott, 1977). It was also used by Hendershott and Speranza (1971) to model strongly localized coastal dissipation at the end of a long channel. These solutions were applied to the Adriatic Sea and the Gulf of California with some success. Finally, the absorbing boundary is included implicitly in Redfield's (1978) model of Long Island Sound and several other basins.

To show the analogy, the solution (32) is used in equation (31) with (42) as a boundary condition to give

$$R' = \frac{gQ + \alpha(\omega^2 - f^2)}{gQ^* - \alpha(\omega^2 - f^2)} = \frac{Q}{Q^*} r', \quad (43)$$

where

$$r' = \frac{1 + \alpha(\omega^2 - f^2)/gQ}{1 - \alpha(\omega^2 - f^2)/gQ^*} \quad (44)$$

is a clear analogy to equations (37) and (38). If α/g is small,

$$r' = 1 + 2 \frac{\alpha(\omega^2 - f^2) \text{Real } 0}{g |Q|^2} \quad (45)$$

Thus α must be complex to agree completely with equation (38) and also must be negative to assure that $r' < 1$.

E. The Sverdrup wave--no reflection

The plane Sverdrup wave is investigated by setting $r' = 0$ and $\ell = 0$, which is the case of no reflection or perfect absorption. For this wave, the ellipticity is defined by

$$\epsilon = -i (v/u) = -(f/\omega). \quad (46)$$

For middle latitudes, the Sverdrup tidal ellipse has an ellipticity of about $-2/3$ --i.e., a clockwise rotation of the current vector and minor axis:major axis ratio of 2:3. The orientation angle of the Sverdrup tidal ellipse coincides with the direction of propagation so in this instance is identically zero.

F. The Poincare wave solution--perfect reflection

Examining the opposite extreme, the case of perfect reflection or $r' = 1$, shows the characteristic tidal ellipses of two superimposed Sverdrup waves whose onshore velocities exactly cancel one another at the shore. This combination is known as the Poincare wave (Platzman, 1971). Often invoked as a solution in a channel, where boundaries result in an eigenvalue problem and a set of discrete cross-channel wave numbers (Defant, 1960), this solution is also valid for long,

straight coasts or continental shelf topographies (Munk, Snodgrass, and Wimbush, 1970) where only one boundary plays an important role in the dynamics. The resulting free surface and velocity distributions are:

$$\zeta = \frac{2a}{Q^*} (\omega \ell \cos \ell y + f k \sin \ell y) e^{i(kx - \omega t)}$$

$$v = \frac{-i2ag}{Q^*(\omega^2 - f^2)} ((\omega^2 - f^2)\ell^2 + f^2(k^2 + \ell^2)) \sin \ell y e^{i(kx - \omega t)} \quad (47)$$

$$u = \frac{2ag}{Q^*(\omega^2 - f^2)} ((\omega^2 - f^2)k\ell \cos \ell y + (k^2 + \ell^2)\omega f \sin \ell y) e^{i(kx - \omega t)}$$

As in the non-rotating, standing wave problem, the possibility of surface nodes is apparent from the first of the equations in (47). Otherwise, the rotating standing wave characteristics are more complicated than the non-rotating case. Turning again to the tidal ellipse to elucidate the signature of the Poincare wave,

$$\varepsilon = -i \frac{v}{u} = \frac{(\ell^2 + f^2/gH) \sin \ell y}{k\ell \cos \ell y + \omega f/gH \sin \ell y}, \quad (48)$$

where the dispersion relation has been used to simplify the expression. Besides depending on the distance offshore, the ellipticity is highly dependent on the wave numbers, or equivalently the angle of incidence of the incoming Sverdrup wave. By defining the angle of incidence as the angle between the wave vector and the shoreline (see figure 5),

$$I = \tan^{-1} \left(\frac{\ell}{k} \right), \quad (49)$$

the wave properties can be plotted as a function of offshore distance

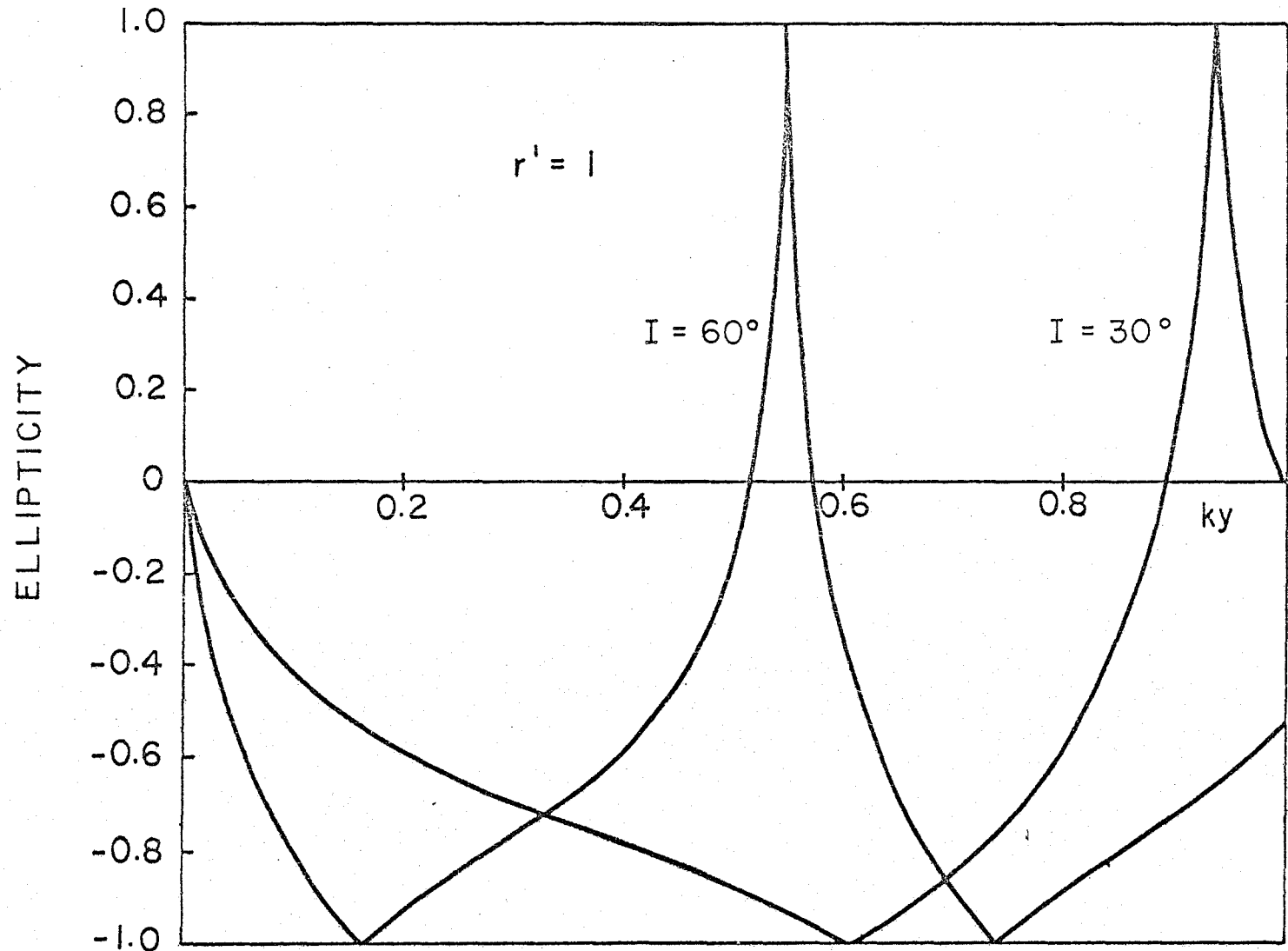


Figure 3-6 Ellipticity versus offshore distance for perfect reflection and several positive incidence angles

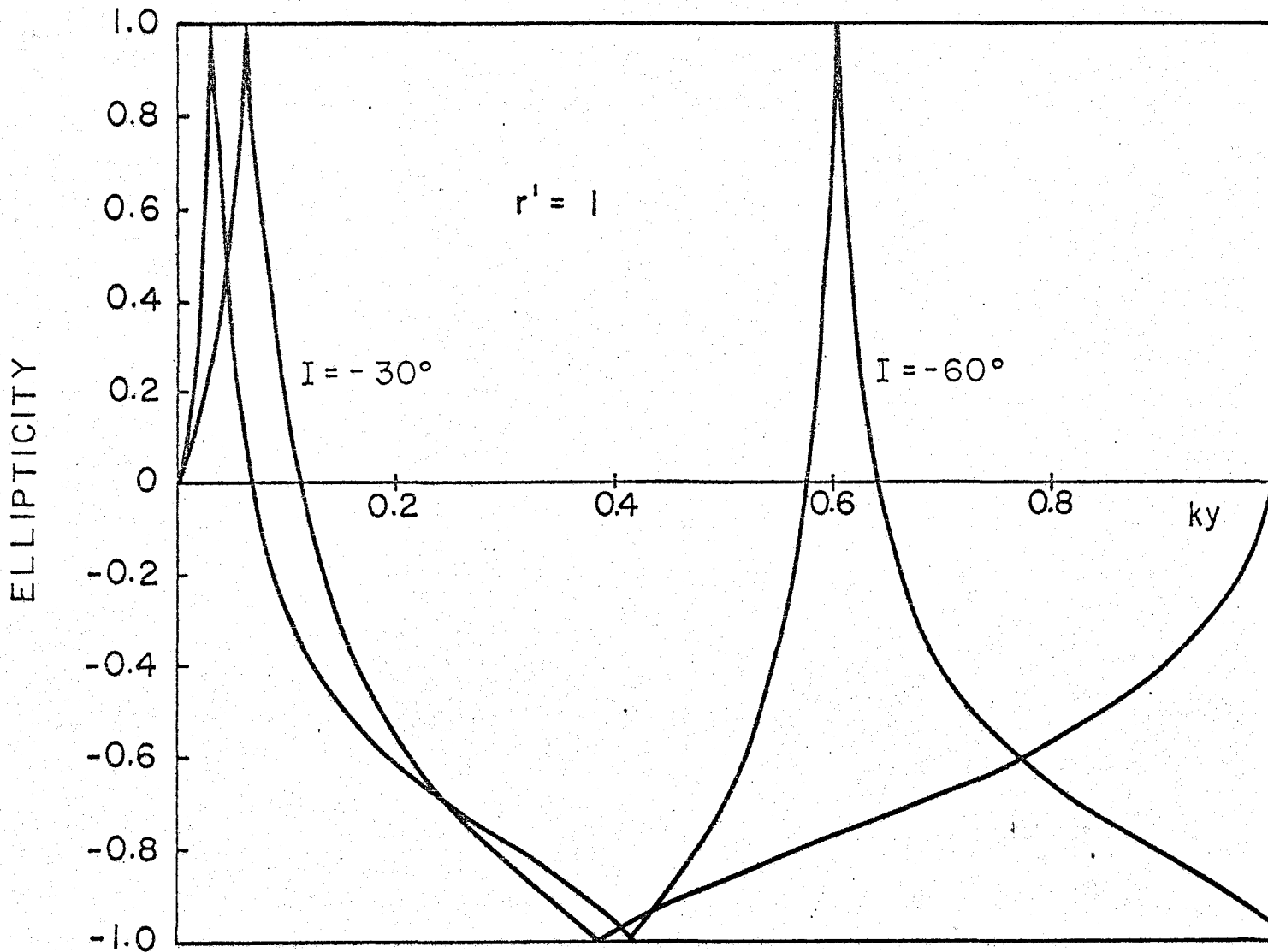


Figure 3-7 Ellipticity versus offshore distance for perfect reflection and several negative incidence angles

for various incidence angles. This is done in figures 6 and 7 for several representative negative (shore on the right-hand when looking in the direction of propagation) and positive incidence angles. Note that the offshore distance in these plots is scaled by the wavelength.

The ellipticity varies greatly, assuming both positive and negative values depending on the angle of incidence and the distance offshore. At the shore ($y = 0$) the ellipticity is identically zero (the ellipse is linearly polarized) but becomes positive a short distance offshore if $k < 0$ (shore to the right) or negative if $k > 0$ (shore to the left). At some distance away from shore, the onshore velocity becomes equal to the alongshore velocity and the ellipse becomes circular. From this point on, the onshore velocities are greater than alongshore velocities and ellipticities tend again toward smaller values.

Also at this point, the orientation of the major axis of the ellipse changes abruptly from 0° to 90° . Since the phase relation between u and v is always 90° (see equation (47)) the orientation is constrained to be either 0° or 90° for all distances from shore and all incidence angles. Figure 8 shows the orientation angle for the same values of the incidence angle (both positive and negative) as the previous figures.

It is clear that the COBOLT data differs substantially from both Sverdrup and Poincare wave models. While the Sverdrup wave current ellipse does rotate in the clockwise direction, the shape of the ellipse is much too circular to agree with COBOLT observations. The

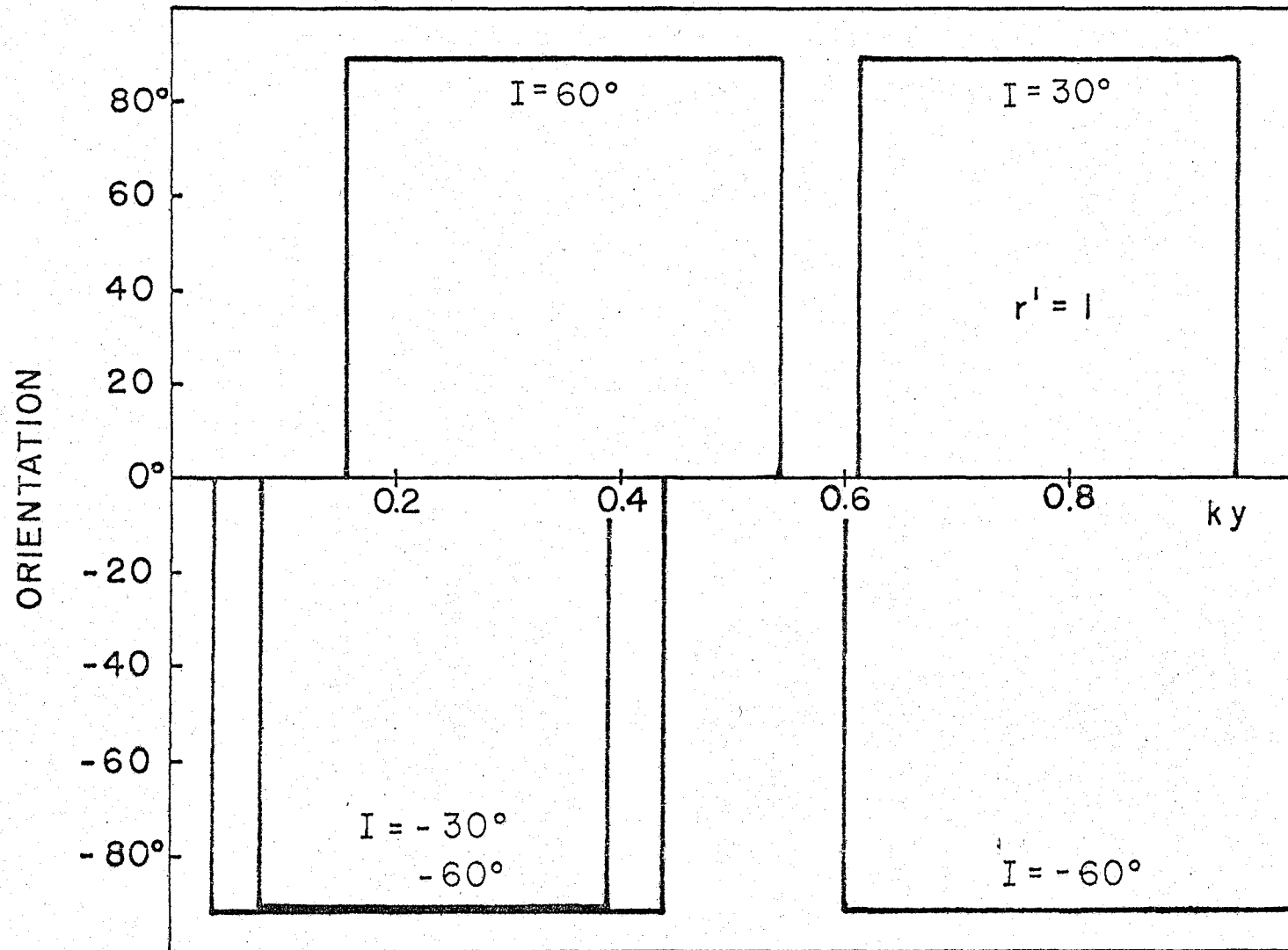


Figure 3-8 Orientation angle versus offshore distance for perfect reflection and several incidence angles

Poincare current ellipse, unlike any of the ellipses in the COBOLT observations, is oriented exactly alongshore and exhibits no onshore orientation tendencies close to the shore. Also, for an incident wave progressing with the shoreline on its right-hand side, Poincare wave model ellipses degenerate into lines very near to the shore and rotate counterclockwise further away, again unlike the observations. So as they stand, the Sverdrup and Poincare waves are not capable of reproducing the results of the COBOLT experiment individually.

G. The combination Sverdrup-Poincare wave

A combination of these waves offers a third alternative, and with pure Poincare and Sverdrup waves as references, the case of $0 < r' < 1$ is less difficult to interpret. This solution consists of an incident Sverdrup wave plus a smaller amplitude reflected Sverdrup wave; or equivalently, a Poincare wave plus a smaller amplitude incident Sverdrup wave. The solutions for this case are:

$$\zeta = -\frac{a}{Q^*}((r'+1)(\omega l \cos ly + fk \sin ly) - i(r'-1)(fk \cos ly + \omega l \sin ly)) e^{i(kx-\omega t)} \quad (50)$$

$$u = \frac{-ag}{Q^*(\omega^2-f^2)} ((r'+1)((\omega^2-f^2)kl \cos ly + (k^2+l^2)\omega f \sin ly) - i(r'-1)((k^2+l^2)\omega f \cos ly + (\omega^2-f^2)kl \sin ly)) e^{i(kx-\omega t)}$$

$$v = \frac{ag}{Q^*(\omega^2-f^2)} ((\omega^2-f^2)l^2 + f^2(k^2+l^2)) \cdot ((r'-1) \cos ly - i(r'+1) \sin ly) e^{i(kx-\omega t)}$$

In natural situations it is likely that the reflection coefficient will generally be close to unity because the shore is certain to reflect much of the energy impinging on it. This is particularly true very near to shore. Nevertheless, it is valuable to consider all possible reflection coefficients since the ellipse parameter diagrams will then be representative of all the possible interactions of two Sverdrup waves of unequal amplitude (just as the Poincare diagrams are representative of all possible interactions of two Sverdrup waves of equal amplitude). The offshore distance can then be interpreted as the phase difference between the two interacting waves. Considering the entire range of reflection coefficients will establish the range of possibilities that exist for two interacting Sverdrup waves and may provide some insight into the forms of tidal ellipses that can occur under a wide range of reflection conditions and distances from shore.

Plots of the tidal parameters are shown in figures 9 through 11 for different real values of the reflection coefficient. Instead of the sharp transitions noted in the Poincare wave ellipse parameters, the combination waves exhibit smoother profiles as interference between the two waves becomes less important. In the $r' = 0$ limit the ellipse parameters reduce to those of the uniformly smooth pure Sverdrup wave with an orientation angle equal to the complement of the angle of incidence and an ellipticity equal to $-f/\omega$.

The ellipticity, as a result of the transition to Sverdrup wave characteristics, increasingly favors negative values as the reflection coefficient drops. Thus, clockwise rotation of the tidal

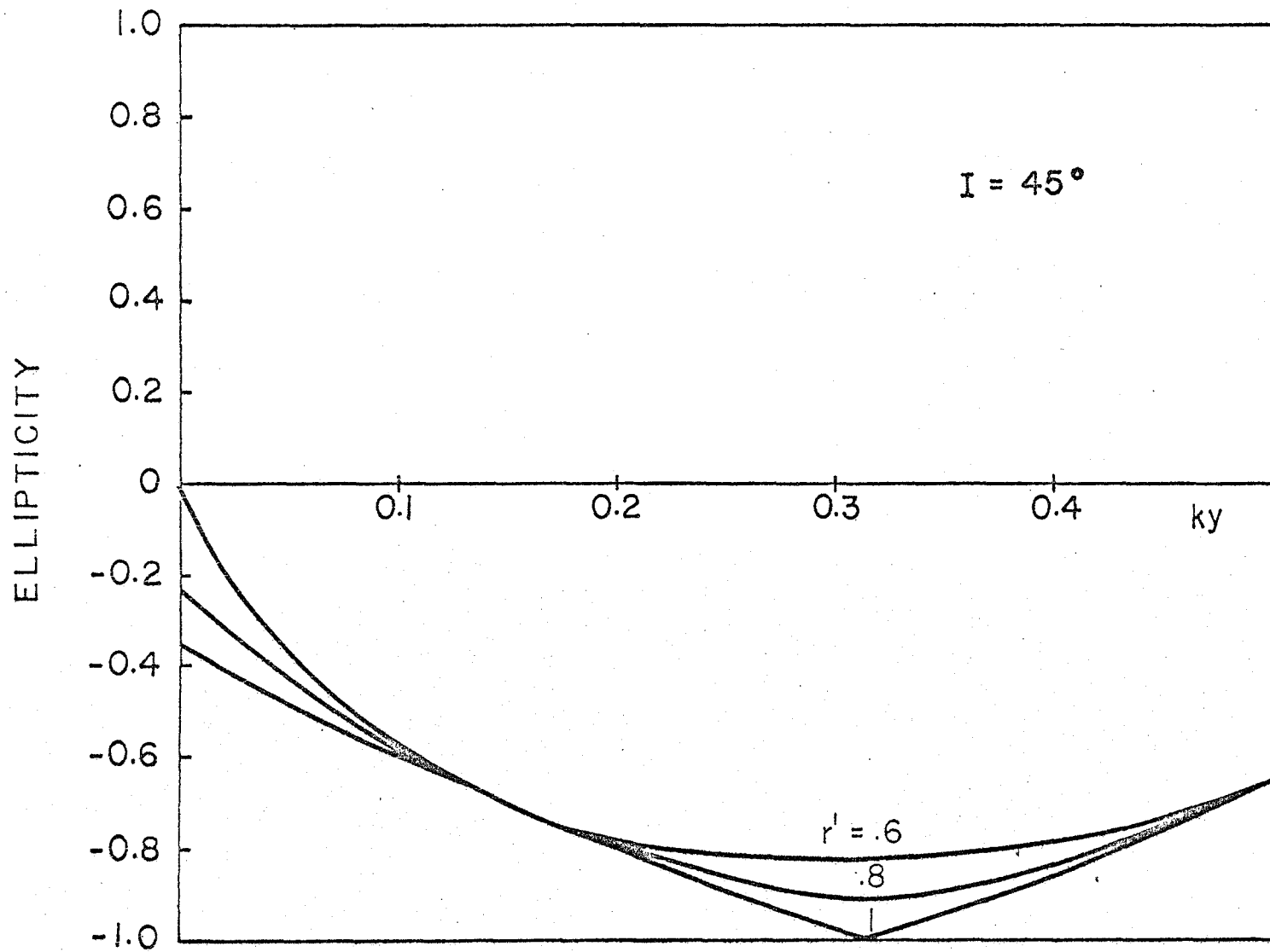


Figure 3-9 Ellipticity versus offshore distance for imperfect reflection

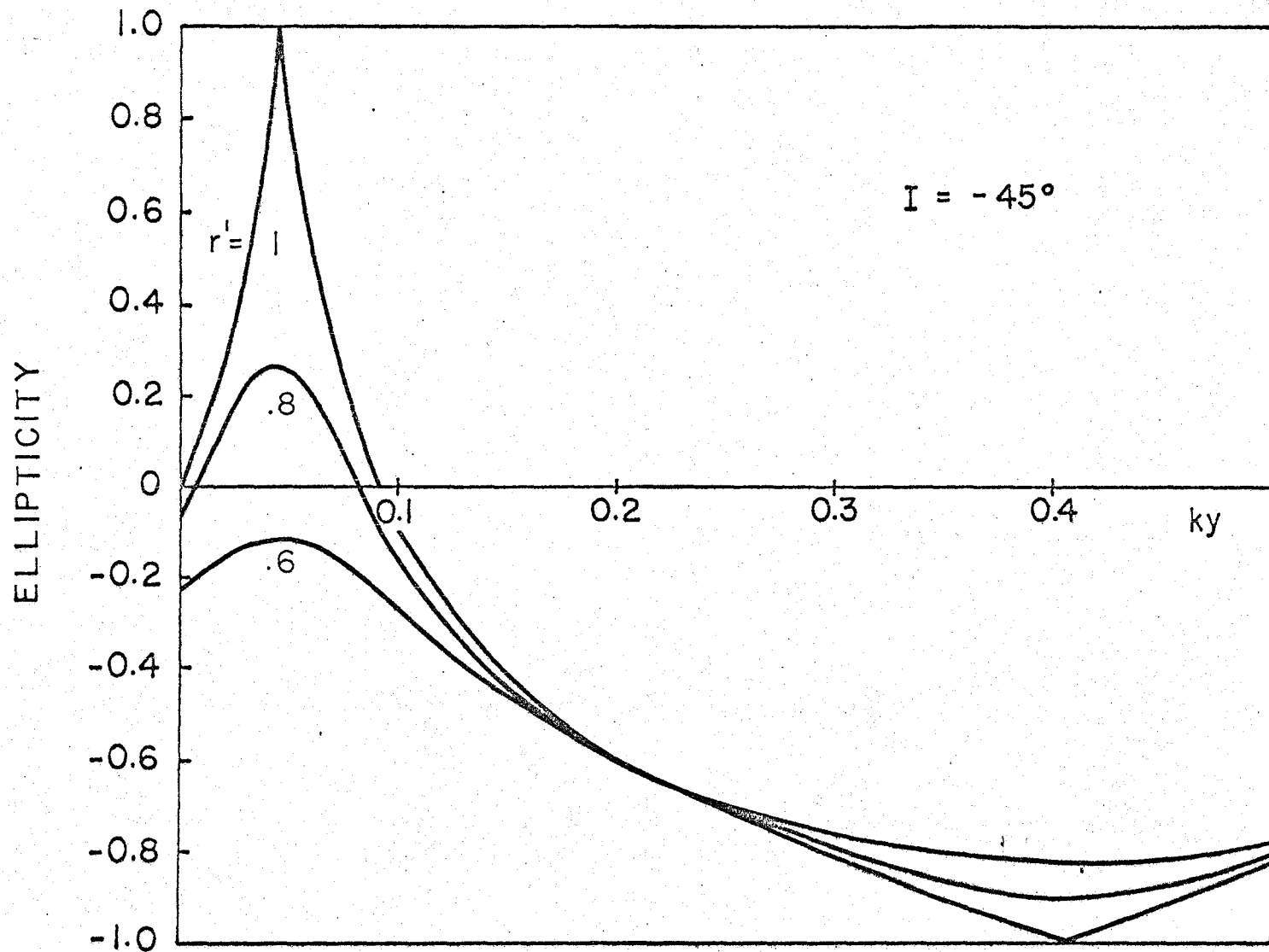


Figure 3-10 Ellipticity versus offshore distance for imperfect reflection

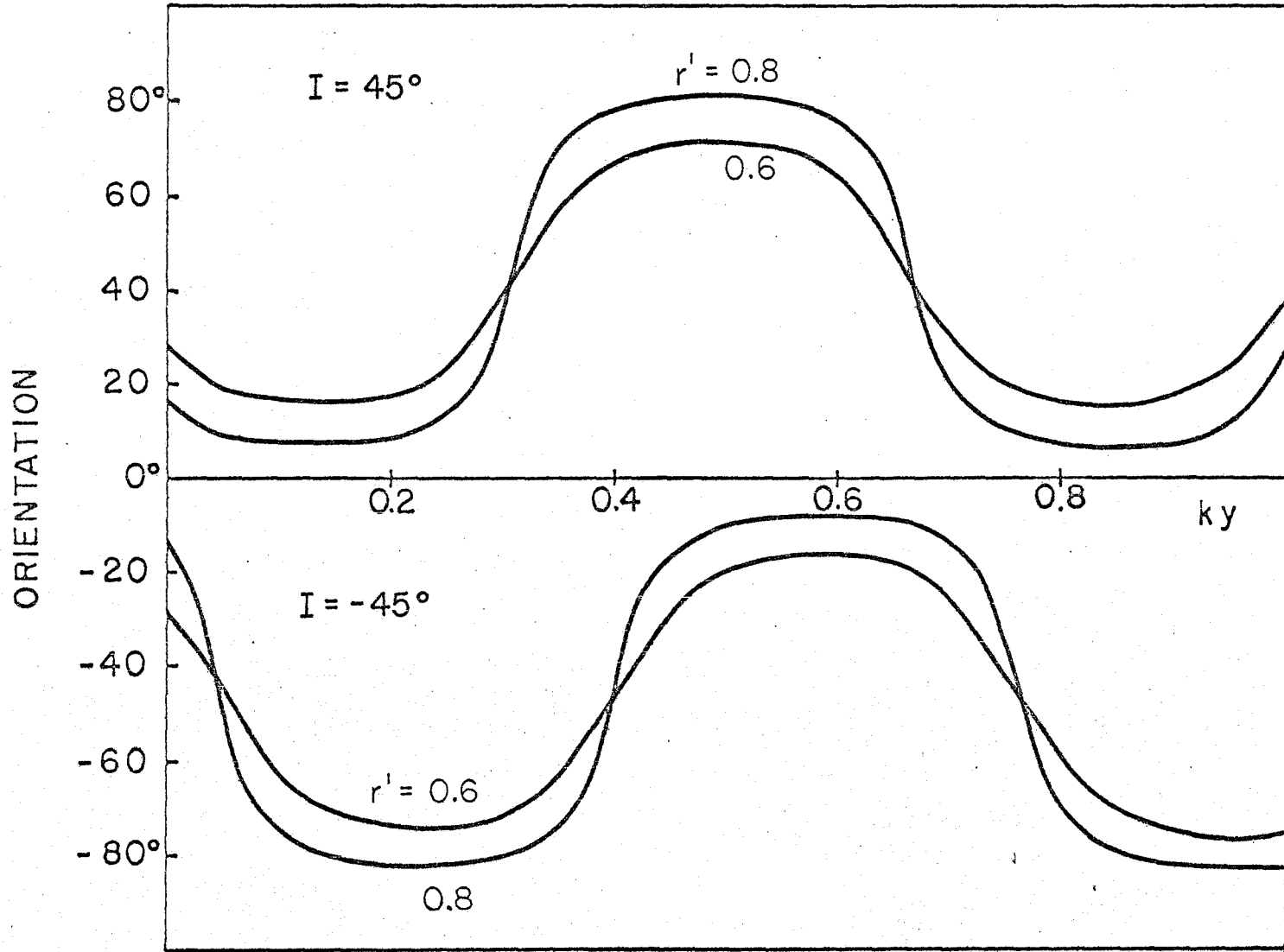


Figure 3-11 Orientation angle versus offshore distance for imperfect reflection

ellipses becomes more probable (as measured by the extent of the graph over which the ellipticity is negative). The probability of observing perfectly circular ($\epsilon = 1$) is quite small since the ellipticity tends to range somewhere between zero and $-f/\omega$. Also, it is seen that orientation angles (figure (11)) no longer exhibit the sharp jumps from 0° to 90° as were seen in the Poincare wave. With these general trends established, extrapolations can easily be made for cases not shown.

Considering that the tidal wavelength is generally large compared to shelf dimensions, the most interesting aspects of the ellipse parameters may be found for $ky \ll 1$. It is apparent from figures 9-11 that, unlike the Poincare wave model, the combination wave allows both non-zero orientation angles and non-zero ellipticities near the shore (near $y = 0$)--features which reproduce the results of the COBOLT experiment.

In particular, the conditions at $y = 0$, which are of the most interest to the COBOLT experiment, are conveniently summarized by plotting the possible combinations of ellipticity and orientation angles as a function of the angle of incidence and the reflection coefficient. The various curves in figure 12 are formed by varying the angle of incidence while holding the reflection coefficient constant. Since the diagram is symmetric about the 0° orientation axis, only negative orientation angles are shown. Also, the range of incidence angles is limited to negative values, $-80^\circ < I < -10^\circ$

(10° angle of incidence increments are indicated by dots), with the exception of the asymptotes which are indicated by dashed lines.

As an alternative for examining the ellipse characteristics for constant r' , a similar plot can be made by holding the angle of incidence constant while varying the reflection coefficient. In figure 13 r' is varied from 0.6-1.0 with dots indicating reflection coefficient increments of 0.1. By considering both of these figures, the variations of ellipse characteristics that occur due to changes in reflection coefficient or angle of incidence should be evident.

From figure 12 (and its reflection about 0°) it is apparent that while the orientation angles can cover the complete range of angles from -90° to $+90^\circ$, ellipticities are always negative nearshore regardless of the angle of incidence or reflection coefficient. For higher reflection coefficients, furthermore, the bulk of incidence angles result in small orientation angles (positive or negative since the plot is symmetric) and small, negative ellipticities. This convergence of lines to small orientations and small ellipticities is quite evident in figure 13 and would make determination of incidence angles difficult in any real situation where reflection coefficients are close to unity. It is also evident from figure 13 that small negative incidence angles (waves with larger alongshore wave numbers) are associated with small negative orientation angles.

The ellipticities and orientations also show variations that depend on the frequency of the incoming wave. Figure 14 shows curves

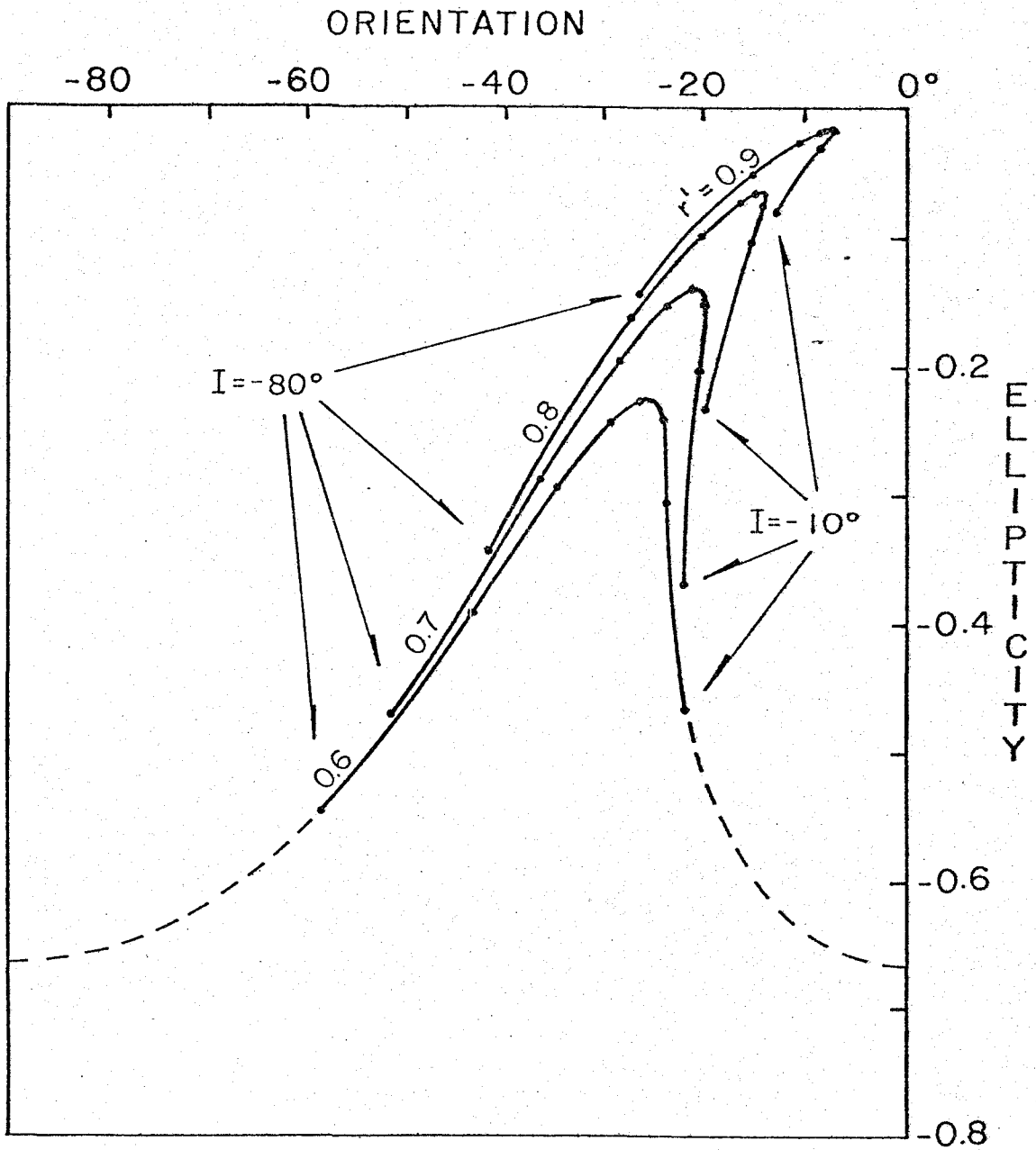


Figure 3-12 Ellipticity versus orientation angle at $y = 0$; incidence angle varied while holding reflection coefficient constant

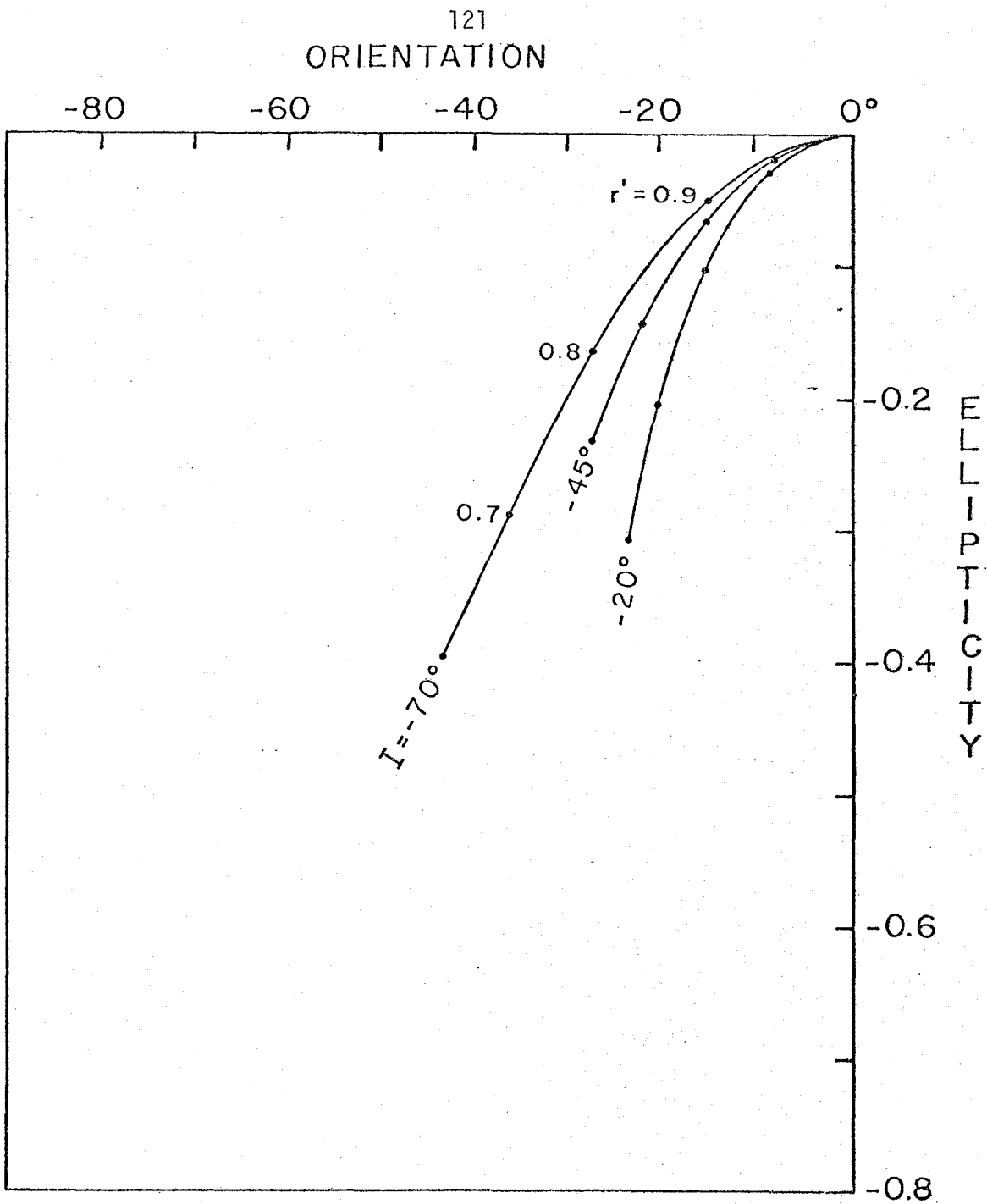


Figure 3-13 Ellipticity versus orientation angle at $y = 0$; reflection coefficient varied while holding incidence angle constant

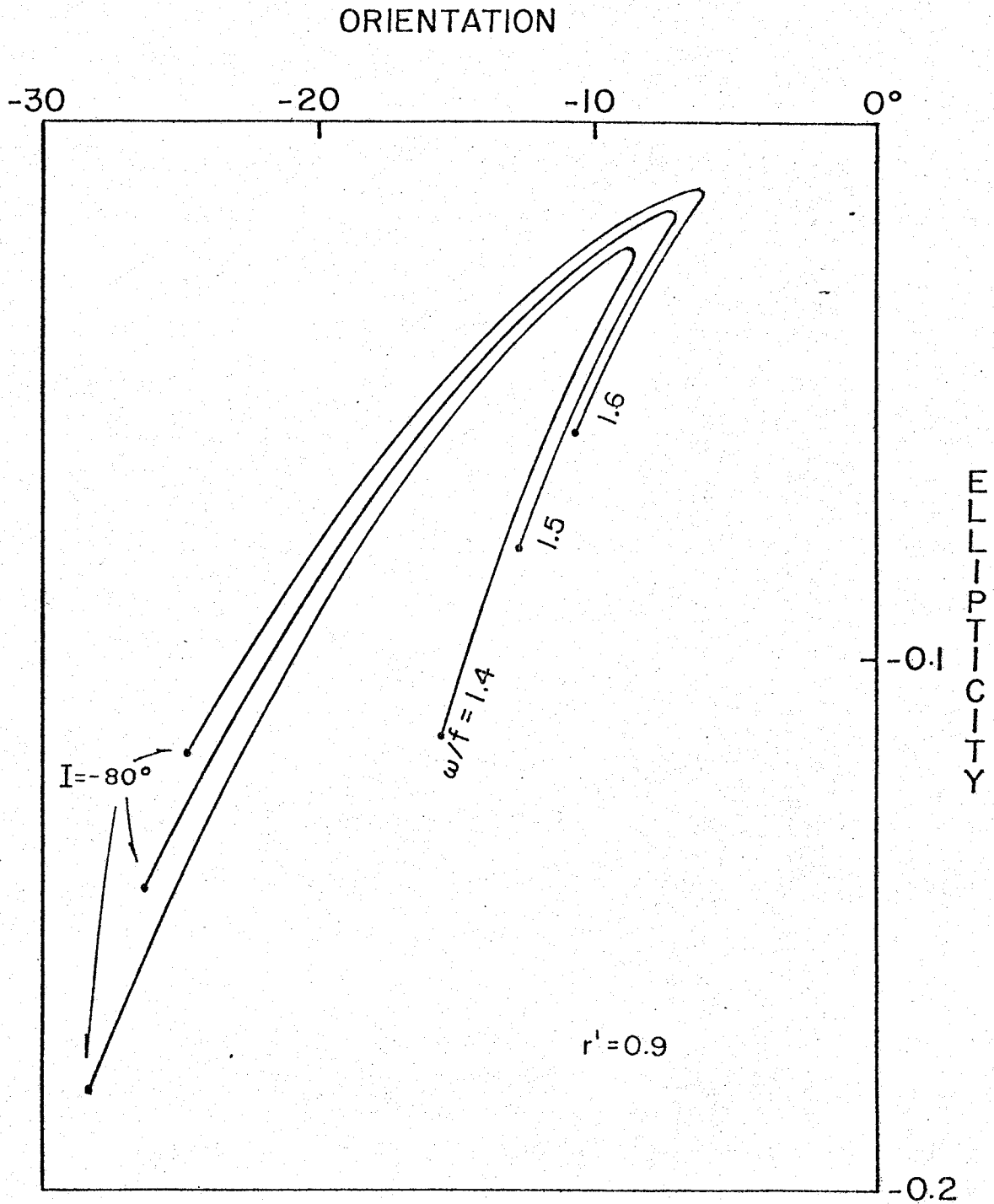


Figure 3-14 Ellipticity versus orientation angle at $y = 0$; varying the incident wave frequency

for several different frequencies for $r' = 0.9$ and for the incidence angle range, $-70^\circ < I < -20^\circ$. Although $\omega/f = 1.5$ was used in the previous figures as representative of the mid-latitude M_2 tide, it is clear from figure 14 that other tidal frequencies have slightly different ellipse characteristics. In particular, higher frequency waves tend to have less negative nearshore ellipticities (i.e., the ellipticity approaches zero) than lower frequency waves.

Again, it should be noted that similar diagrams for positive incidence angles (shore on the left of a wave if looking in the direction of propagation) can be constructed simply by reflecting the plots around the 0° orientation angle axis. The main affect of this operation is that all orientation angles become positive when the coast is on the left of an incoming wave.

H. Comparison of the model to observations

A comparison of the COBOLT observations with the Sverdrup-Poincare wave model is accomplished by plotting the observed orientations and ellipticities of the three resolved semidiurnal tidal components on figure 12. Figure 15 shows an enlarged corner of figure 12 with these observed values in place.

The positions of the observations on the plot are consistent with that of an incident wave emanating from the deep ocean (negative incidence angle) since observed orientation angles are negative; a fact predicted by the modelling of waves with a coast on the right-hand side of the wave (looking in the direction of propagation).

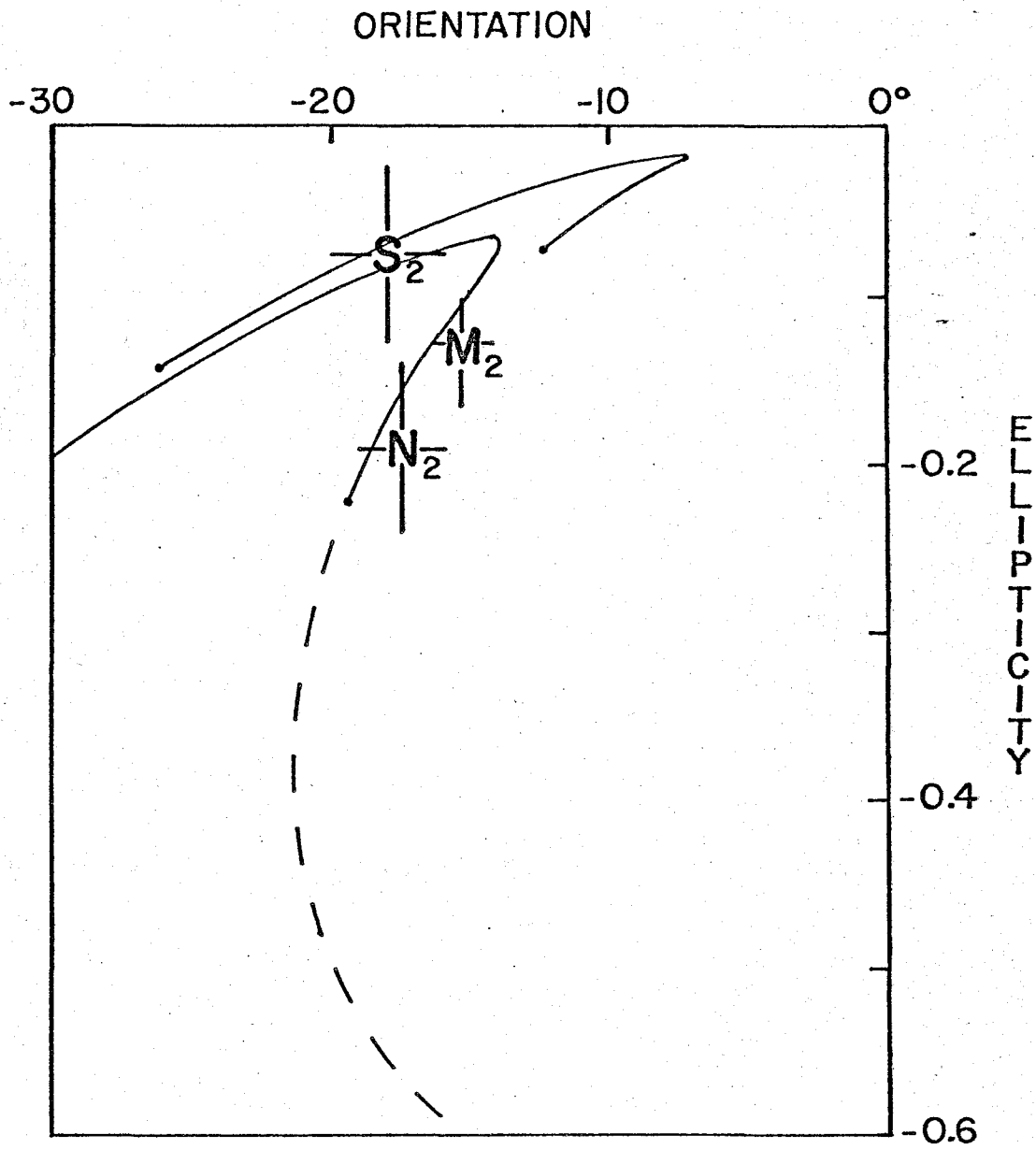


Figure 3-15 Ellipticity versus orientation angle at $y = 0$ with COBOLT observations plotted for three semidiurnal frequencies

Furthermore, the data are also consistent with predictions for large incidence angles (since observed orientation angles are small) and large reflection coefficients (since observed ellipticities are close to zero). Finally, the data exhibit the dependence on frequency suggested by the theory--i.e., the highest frequency semidiurnal tidal component, S_2 , is closest to zero ellipticity, while the lowest frequency component, N_2 , is furthest away.

The notion of small incidence angle can be confirmed independently, to some degree, by examining Swanson's semidiurnal cophase chart (figure 2-2). It shows that the wave vector (which is perpendicular to cophase contours, or wave crests) does indeed form a small angle with the south shore of Long Island. While some ambiguity exists, due to the curvature of cophase lines, this angle appears to be approximately -20° .

Physical considerations suggest that a large reflection coefficient is also a reasonable result. By requiring that theoretical onshore energy fluxes match observed energy fluxes, it is possible to compute a reflection coefficient. From the energy flux equation (chapter 2) and the Sverdrup-Poincare free surface and onshore velocity distributions (equation (50)), the onshore flux is

$$\begin{aligned} F_y &= gH \operatorname{Real} \langle \zeta v^* \rangle = \\ &= \frac{a^2 g^2 H}{\omega^2 - f^2} \frac{1 - r'^2}{2} \end{aligned} \quad (51)$$

Substituting the following numerical values into (51):

$$a = 50 \text{ cm}$$

$$H = 30 \text{ m}$$

$$\omega = 2 / 24 \text{ hr}$$

$$l = 2 / 1500 \text{ km},$$

and equating it to the energy flux estimates of chapter 2 (COBOLT measurements and Miller's shelf-wide estimate) gives

$$r' = 0.98 \pm .01, \quad (52)$$

a value that supports the large reflection coefficient deduced from the tidal ellipse parameters.

Since the ellipse parameters depend on the two unknowns, reflection coefficient and angle of incidence, it is impossible to determine the values of both with an observation at a single frequency. In principle, the three independent semidiurnal frequencies could be used to find the values of r' and I , but this procedure is very difficult because of the complexity of the equations involved and the uncertainties of the observations. The estimate of incidence angle obtained from Swanson's work offers an alternative since once this angle is known it is a straight-forward task to determine the reflection coefficient from a single observation of ellipticity and orientation. Doing this for the M_2 tidal frequency with $I = -20^\circ$ gives a reflection coefficient of

$$r' = 0.95, \quad (53)$$

which is close to the estimate derived in (52).

Other observations in the Middle Atlantic Bight support the Sverdrup-Poincare wave model too. The model suggests that clockwise

rotating tidal current ellipses should be the norm in most circumstances. Emery and Uchupi (1972) found that this was true at 94% of the sites surveyed by Haight (1942). Redfield's (1958) empirical fit of long gravity waves (without rotation) to tidal elevations and phases in the Middle Atlantic Bight implies that the Sverdrup wave, the extension of the long gravity wave to a rotating system, is the appropriate solution for modelling tidal phenomena in the region. Finally, the results of Patchen, Long, and Parker (1976) (figure 2-3) show ellipses for a wave propagating with a shoreline to the left-hand side (New Jersey) looking in the direction of propagation, and for a wave propagating with a shoreline to the right-hand side (Long Island). Both of these cases show the predicted sense of ellipse orientation in nearshore measurements--a positive orientation angle for the shore-to-the-left case and a negative angle for the shore-to-the-right case.

The two-wave, Sverdrup-Poincare model is clearly an oversimplification of the complex tidal regime of the region, even though it does explain many of the observed features. The model, for example, does not account for geometries other than infinitely long, straight coasts. Corners, such as that formed by the coast of Long Island and the coast of New Jersey, and the additional reflections that result from them are not considered. Small scale coastal irregularities, which scatter incoming wave energy (Mysak, 1978), are also ignored. And, the two-wave model predicts an energy flux in the direction of wave propagation (towards the west at the COBOLT site) that is an order of magnitude larger than that which is observed.

Kelvin waves have also been ignored, though this is not likely to be a serious flaw. The semidiurnal tides of the Middle Atlantic Bight generally progress in the onshore direction and have the small energy fluxes that are characteristic of standing waves. By contrast, the Kelvin wave, a possible solution (though not in this model), would be attenuated offshore and have a large alongshore energy flux. These features are not seen in the observations.

Although more complicated models are possible and may be necessary to account for these additional features, the comparison with observations is good enough to suggest that:

1. The classical Sverdrup wave is the fundamental mode of propagation for the semidiurnal tides of the Middle Atlantic Bight since it accounts for many of the observed features of the tidal currents.
2. The coastal region absorbs a small amount of the incident energy of the Sverdrup wave, probably through frictional dissipation in water shallower than 10 m. This absorbed energy, although a small fraction of the incident wave energy, is larger than some previous studies have suggested.

I. The effects of local topography

It is of considerable interest to consider the effects on the Sverdrup-Poincare wave model of one particular complicating feature that is evident in the COBOLT region--topography. Not only is it of interest to consider depth variations to determine how far away from

shore can be correctly considered a small distance in the step model, but also to shed some light on the question of where the inferred dissipation may occur. In other words, it is hoped that this model will answer the questions: how good is the vertical wall assumption, and where does the large amount of energy observed to be propagating onshore dissipate?

The long wave equations, with no bottom friction, can be solved for a variety of bottom profiles. The COBOLT region, however, has a particularly well-suited profile to approximate by a simple analytical expression. This function is

$$H(y) = H_0(1 - b e^{-sy}), \quad (54)$$

where H_0 , s , and b are chosen to give the best fit to the actual bottom profile of the area. These constants were chosen from a straight-line fit on the graph of $\ln(H_0 - H)$ versus y shown in figure 16. In this plot, y is only extended to 14 km--slightly greater than the distance of the outermost COBOLT mooring. Of the different values of H_0 shown, $H_0 = 35$ m appears to give the best fit. The linear fit for this depth gives $b = 0.9$ and $s = 0.2 \text{ km}^{-1}$ as the approximate parameters in equation (54). A comparison of the resulting computed profile with the actual depth profile is shown in figure 17.

With the depth variations retained and the bottom stresses omitted in equations (24), elimination of the velocities gives the equation for the free surface,

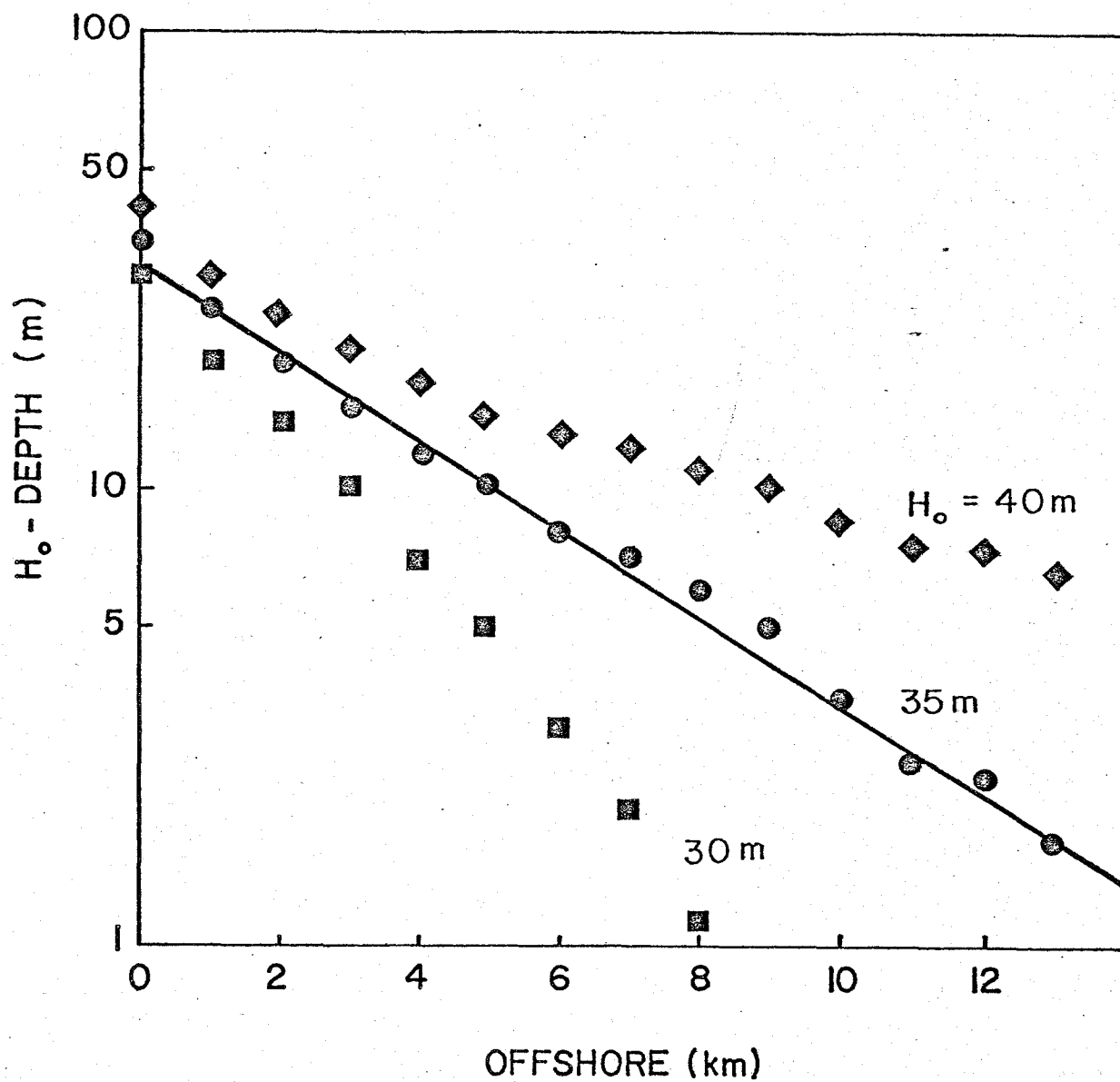


Figure 3-16 Plot of $\ln(H_o - H)$ versus offshore distance at the COBOLT site, plus linear curve fit

$$\left(\frac{\partial^2}{\partial t^2} + f^2\right) \frac{\partial \zeta}{\partial t} - gHV^2 \frac{\partial \zeta}{\partial t} - g \nabla H \cdot \left(\nabla \frac{\partial \zeta}{\partial t} - \hat{f}k \times \nabla \zeta\right) = 0. \quad (55)$$

Taking the depth to be only a function of the offshore variable allows a solution,

$$\zeta(x, y, t) = F(y) \exp i(kx - \omega t), \quad (56)$$

which, when substituted into (55), results in the second order, ordinary differential equation,

$$\frac{d^2 F}{dy^2} + \frac{1}{H} \frac{dH}{dy} \frac{dF}{dy} + \left(\frac{\omega^2 - f^2}{gH} + \frac{fk}{\omega} \frac{1}{H} \frac{dH}{dy} - k^2\right) F = 0. \quad (57)$$

A change of the independent variable to

$$z = b \exp(-sy), \quad (58)$$

and substitution of the depth profile (54), transforms (57) to

$$z^2(1-z) \frac{d^2 F}{dz^2} + z(1-2z) \frac{dF}{dz} + (\alpha^2 + \beta z) F = 0, \quad (59)$$

where

$$\alpha^2 = \frac{1}{s^2} \left(\frac{\omega^2 - f^2}{gH} - k^2\right)$$

$$\beta = \frac{k}{s} \left(\frac{f}{\omega} - \frac{k}{s}\right).$$

Equation (59) is one of the many variations of the hypergeometric equation (Morse and Feshbach, 1953). It has regular singularities at $z = 0, 1, +\infty$ (or at $sy = +\infty, \ln b, -\infty$); all of which lie outside the domain of interest provided $b < 1$.

This equation has been studied in an oceanographic context before by Ball (1967) and by Munk, Snodgrass, and Wimbush (1970). Its solutions, hypergeometric functions, are tabulated in Abramowitz and Stegun (1964) but are so general as to obscure the results. It is much more illuminating to solve equation (59) directly using the method of Frobenius.

Substituting the infinite series,

$$F(z) = z^p \sum c_n z^n, \quad (60)$$

into equation (57) and equating lowest order terms gives the indicial equation,

$$p^2 + \alpha^2 = 0. \quad (61)$$

This equation has two distinct roots which are associated with the two independent solutions of the second order problem. Equating the higher order terms determines the constants c_n , for $n > 0$, by the equation

$$c_n = \frac{(p+n)(p+n-1) - \beta}{(p+n)^2 + \alpha^2} c_{n-1}. \quad (62)$$

Or, with the use of (61) to eliminate p ,

$$c_n = \frac{(n(n-1) - \beta - \alpha^2) \pm i(2n-1)}{n(n \pm i2\alpha)} c_{n-1}. \quad (63)$$

For large n (i.e., $z \rightarrow 0$) the solution becomes

$$\lim_{sy \rightarrow 0} F(y) = b e^{i\alpha sy}, \quad (64)$$

provided $\alpha^2 > 0$. This solution is simply the plane Sverdrup wave solution which is appropriate, apparently, for large y (that is, over the flat portion of the topography) or for large s (that is, for a steep slope). The similarities between this and the step model can be pursued by examining an incident (using the plus sign in equation (64)) and a reflected (minus sign) wave just as before. It is also apparent from (63) and (59) that $s\alpha = \ell$ is an appropriate definition for the wave number in the offshore direction.

Both of the previous studies have examined the case for $b = 1$ and emphasized solutions where $\alpha^2 < 0$. These are the shore-trapped modes consisting of topographic, Kelvin, and edge waves. Ball completely ignores the trigonometric solutions while Munk, Snodgrass, and Wimbush merely point out that they exist. Neither of the previous studies examined the shapes of the solutions; only their spectra.

In the interest of examining the effects of this specific depth profile, the final form of the trigonometric solutions is rearranged to consist of an incident and reflected wave. From equations (57) and (60):

$$\zeta = (A e^{i\ell y} \sum c_n^+ b^n e^{-sny} + B e^{-i\ell y} \sum c_n^- b^n e^{-sny}) e^{i(kx - \omega t)}, \quad (65)$$

where $c_0 = 1$. The absorbing boundary condition is applied as before, by demanding that the reflected wave amplitude be less than

the incident wave amplitude for $r' < 1$, and that the onshore velocity vanish at the coast for $r' = 1$ (This condition determines the phase of the reflected wave.). The onshore velocity is

$$v = \frac{g}{\omega^2 - f^2} (A e^{i\lambda y} \sum c_n^+ b^n (Q + i s \omega n) e^{-s n y} - (B e^{-i\lambda y} \sum c_n^- b^n (Q^* - i s \omega n) e^{-s n y}) e^{i(kx - \omega t)}, \quad (66)$$

where Q is defined in equation (36). This determines the coefficients,

$$A = r' \sum c_n^* b^n (Q^* - i s \omega n) = r' B^* \quad (67)$$

$$B = \sum c_n b^n (Q + i s \omega n).$$

Here it has been noted from equation (63) that $c^+ = c^{-*} = c$.

The final form of the solution closely parallels that of the step model (compare to equation (40) and (41)):

$$\zeta = (F^*(y) e^{-i\lambda y} + r' F(y) e^{i\lambda y}) e^{i(kx - \omega t)}$$

$$v = \frac{g}{\omega^2 - f^2} (r' e^{i\lambda y} (Q F(y) + i s \omega G(y)) - e^{-i\lambda y} (Q^* F^*(y) - i s \omega G^*(y))) e^{i(kx - \omega t)} \quad (68)$$

$$u = \frac{g}{\omega^2 - f^2} (r' e^{i\lambda y} (S^* F(y) - s f G(y)) + e^{-i\lambda y} (S F^*(y) + s f G^*(y))) e^{i(kx - \omega t)}$$

where

$$F(y) = B^* \sum c_n b^n e^{-s n y}$$

$$G(y) = B^* \sum c_n b^n n e^{-s n y},$$

and S is defined as in equation (41). These functions are easily calculated numerically, but several features can be noted before the solution is presented.

One of the questions to be answered is whether or not the step topography is an adequate representation of the COBOLT region. This is accomplished by examining the ratio c_1/c_0 since the successive terms in the series are a measure of the extent to which the solution deviates from a plane wave. This ratio,

$$\frac{c_1}{c_0} = \frac{-(\beta + \alpha^2) + i\alpha}{1 + i2\alpha}, \quad (69)$$

is small if both α and β are small. These parameters are indeed small for the semidiurnal frequency waves since

$$\alpha \propto l/s \quad \beta \propto k/s \quad (70)$$

are the ratios of the topographic length scale to the tidal wavelengths. The ratio (69) is estimated to be no greater than 0.03.

This result does not imply that the topography will be unimportant to tidal characteristics very near to the shore, particularly within the region of topographic change. Off Tiana Beach, the characteristic topographic scale is $l/s = 5$ km so variations in the current meter records between the COBOLT moorings are a possibility. Far from the coast, however, the shore can be considered a vertical wall for tidal models.

For perfect reflection ($r' = 1$) the expressions in equation (68) simplify considerably since all three are either the sum or difference of a number and its complex conjugate. Disregarding the x dependent term, $\exp i(kx - \omega t)$, this means that ζ and u are real quantities and v is imaginary. So, just as in the flat-bottom, vertical boundary model, the velocities, u and v , are 90° out-of-phase and ellipse orientation angles are restricted to be either 0° or 90° . Again, an energy absorbing boundary condition ($r' < 1$) is necessary to provide the orientation "tilt" needed to fit the observations.

The absorbing boundary condition is much more effective in shoaling water, however, since the incoming wave crests are refracted by the topography to parallel the shoreline. Moreover, a plot of the orientation angle as a function of offshore distance (figure 18) shows that this effect is only evident very near to the shore--too close to be detected by the COBOLT moorings.

A plot of the computed ellipticity (figure 19) shows that an absorbing boundary condition is also needed in the presence of topography to bring the ellipticity to the magnitude and sign of the observations. Again, the greatest variations occur closer to shore than could have been detected with the operational COBOLT moorings.

These computations suggest that the strongest variations may be observed in a region very close (within 2-3 km) to the coast. They also support the inter-mooring averaging used in chapter 2 to increase the statistical confidence in the tidal current measurements

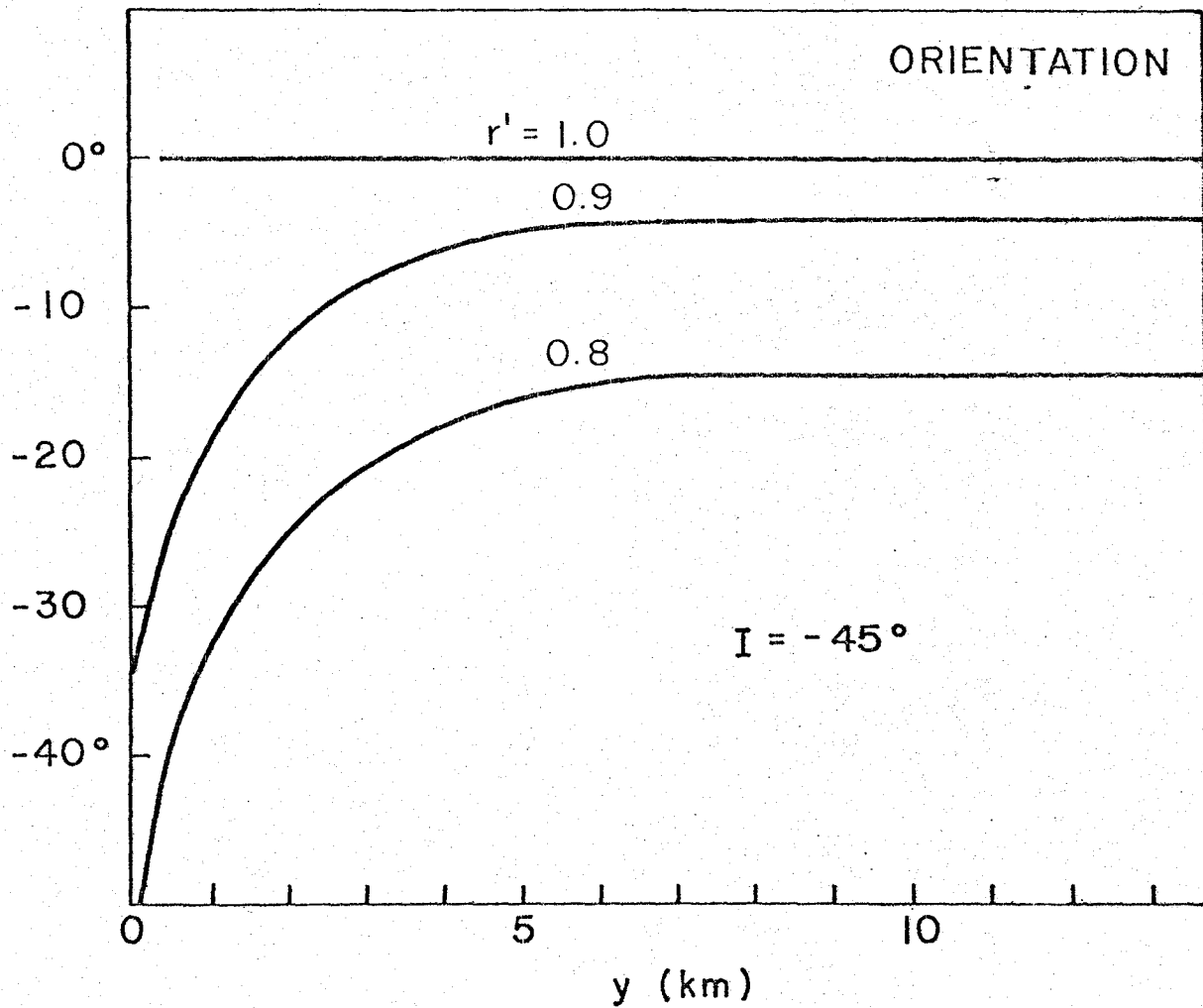


Figure 3-18 Orientation angle versus offshore distance for the depth dependent model

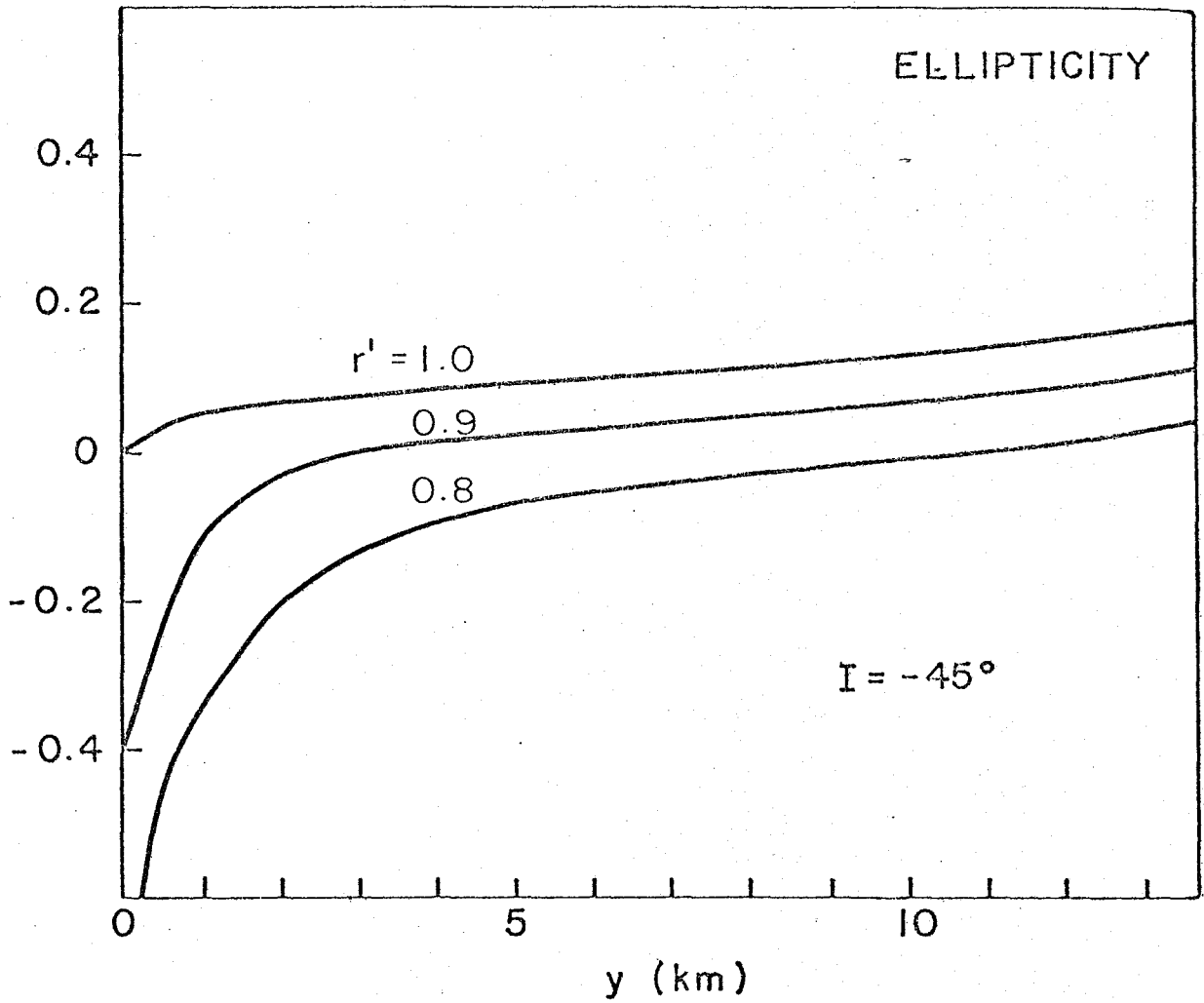


Figure 3-19 Ellipticity versus offshore distance for the depth dependent model

since the depth-varying model suggests little variation in ellipse parameters beyond 5 km from shore.

The question of where the inferred tidal dissipation might occur and whether it is great enough to account for the reflection coefficients can be answered in part by examining equation (59). As noted previously, this equation has a singularity at $z = 0$, or equivalently at $sy = \ln b$, which lies very close to the shore for $b < 1$ and exactly at the shoreline for $b = 1$. The velocities and free surface are kept finite at this singularity by choosing the integration constants, A and B, correctly; i.e., by demanding that all incoming wave energy be reflected (the Sommerfeld radiation condition). This case of perfect reflection ($r' = 1$) leads to a standing wave and fairly uniform energy over the entire nearshore region. Allowing a purely progressive wave, on the other hand, permits the velocities to become infinite at the singularity, which in turn allows a large energy level near to the singularity.

Examining the kinetic energy as a function of offshore distance for several different values of r' confirms this. Figure 20 is a plot of

$$\text{KINETIC ENERGY} = \frac{1}{2} H (u^2 + v^2) \quad (71)$$

computed for the depth-dependent model. The kinetic energy actually decreases nearshore for the case of perfect reflection, while energies for $r' < 1$ show the presence of the singularity by rising

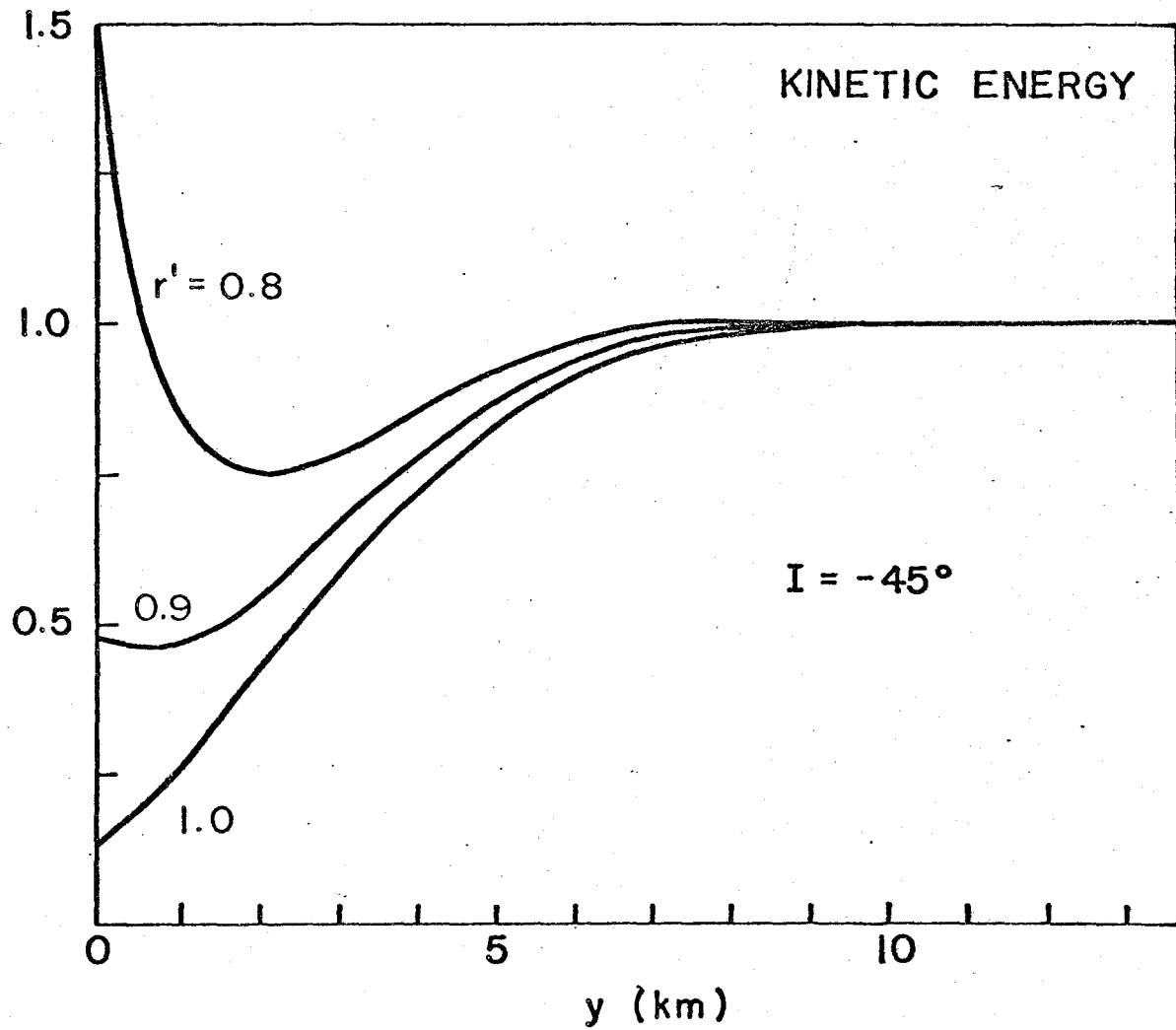


Figure 3-20 Kinetic energy versus offshore distance for the depth dependent model

slightly very close to the shore. The depth factor in (71) diminishes this effect somewhat.

It is reasonable to assume that dissipation rates are great where the energy content of the wave field is great, even though friction is not included in the model. The dissipation rate in this instance can be estimated using Taylor's (1919) dissipation equation,

$$\text{DISSIPATION} = C_d |\vec{U}|^3 = C_d (u^2 + v^2)^{3/2} . \quad (72)$$

Figure 21 shows the computed values of this function for the depth-varying model, again for several different values of r' and with a uniform offshore dissipation rate of 1. The nearshore dissipation rate, as expected, shows a marked increase near the shoreline only for imperfectly reflected waves ($r' < 1$). This increase starts to be apparent at about 5 km distance from the shore and, once again, cannot be detected by the COBOLT moorings. Furthermore, it is many times greater than the offshore rate and is certainly able to account for the additional dissipation needed to explain the observed onshore energy flux.

In contrast to the kinetic energy and dissipation, the free surface (figure 22) does not show a rise in amplitude near to the shore for any of the realistic values of the reflection coefficient. It exhibits instead the linear trend characteristic of co-oscillating tides (Petrie, 1975). The relatively flat wave amplitude also agrees with coastal observations and implies that high dissipation rates could not be detected by observations taken from tidal stations.

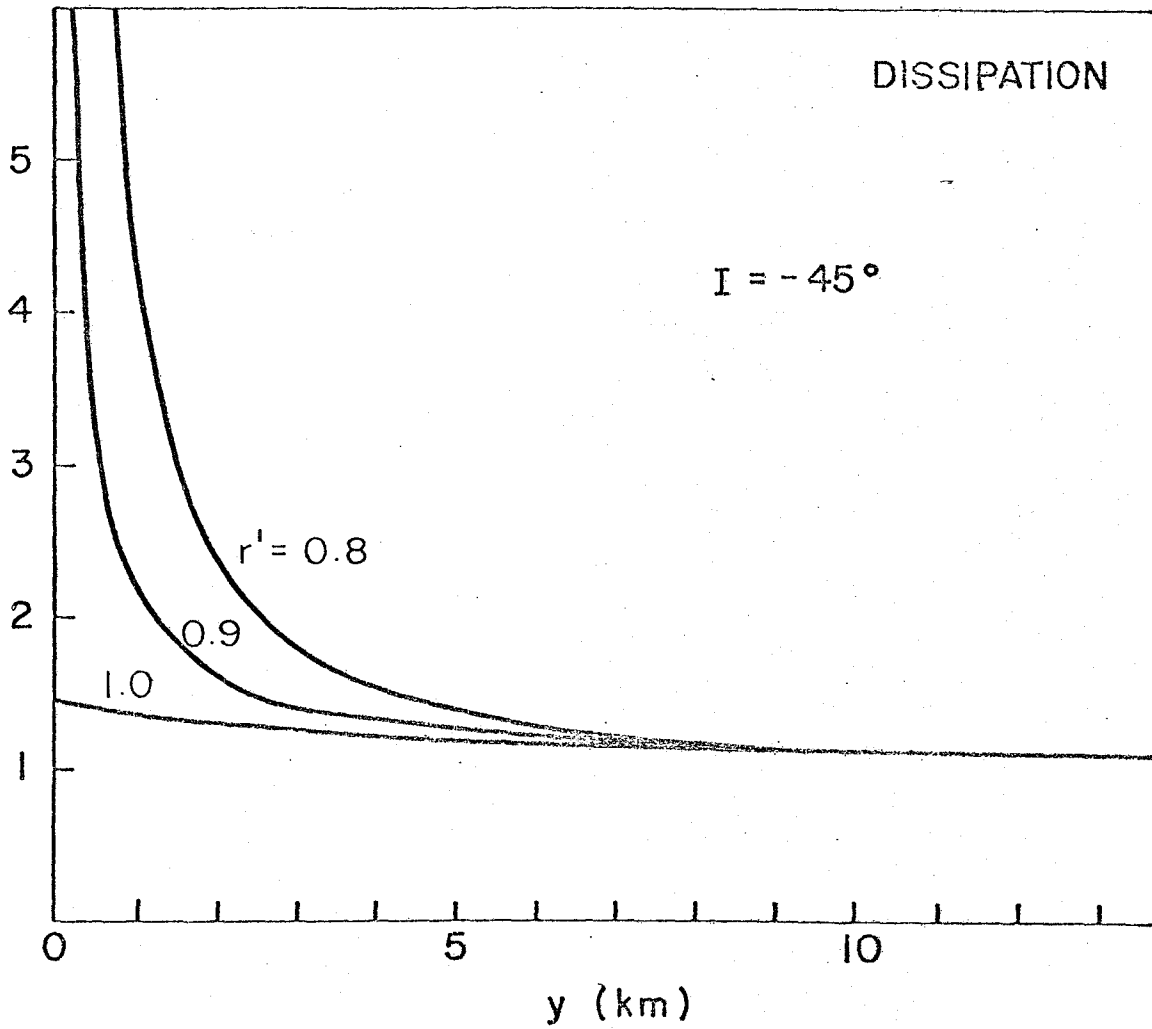


Figure 3-21 Dissipation versus offshore distance for the depth dependent model

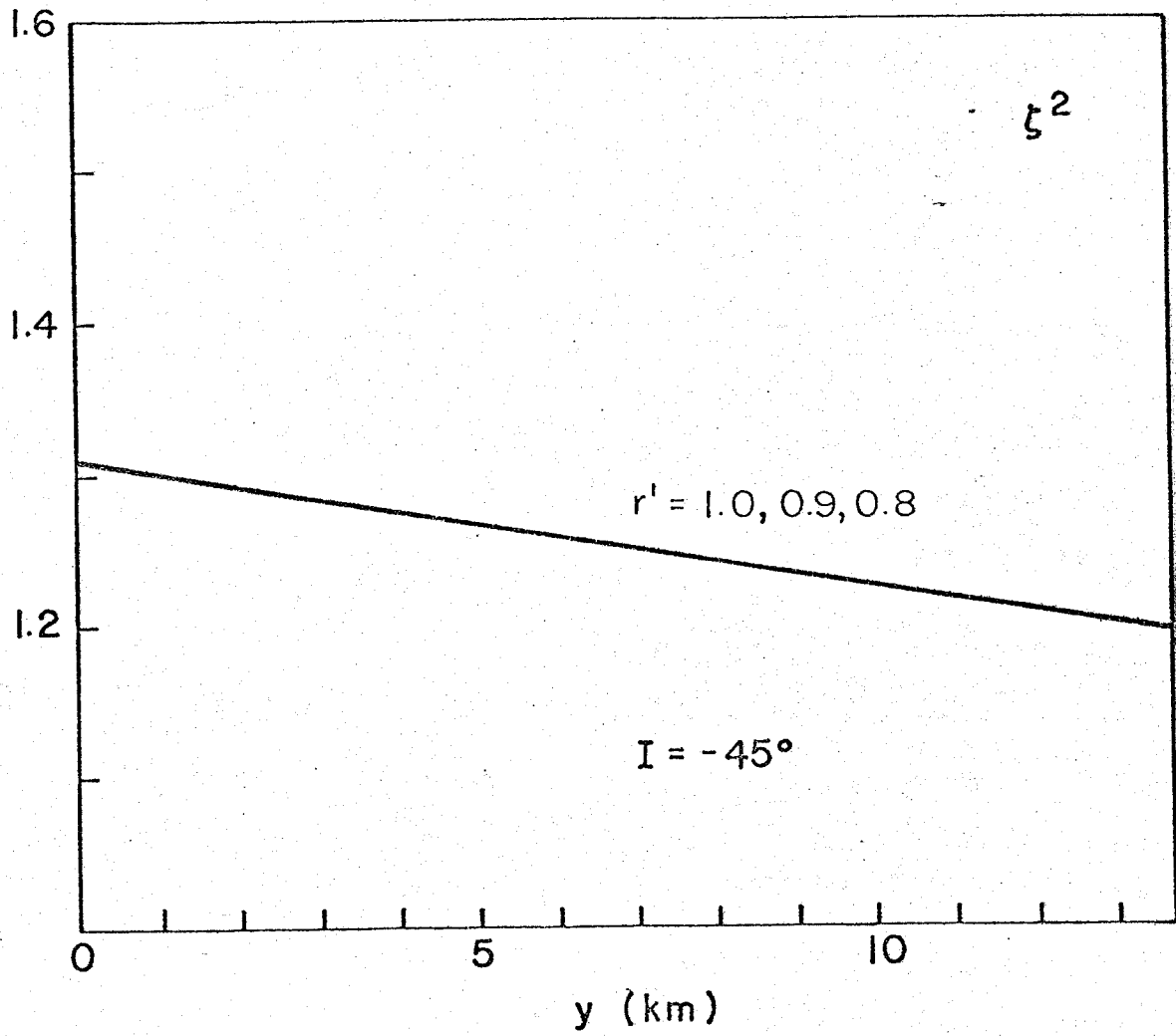


Figure 3-22 Free surface elevation versus offshore distance for the depth dependent model

Retaining a realistic topography in the Laplace tidal equations appears to confirm some notions that have been advanced to explain the COBOLT tidal records; namely, that variations across the three moorings are minimal and can be modelled effectively by a vertical-wall coastline, and that the inferred tidal dissipation may be possible in shallow water inside the coverage region of the COBOLT experiment.

J. Summary

Three idealized analytical models have been examined in an effort to illuminate the effects of friction on tidal measurements in the coastal region. They were: a constant eddy viscosity, vertical structure model; a reflected Sverdrup wave model with an absorbing vertical coastline; and, a reflected Sverdrup wave model with simple topography.

From the first of these models, it appears that a constant eddy viscosity parameterization of frictional stresses allows an adequate description of the vertical structure of semidiurnal and diurnal ellipticity and orientation, provided the proper boundary conditions are applied. The bottom boundary condition, which in Sverdrup's (1926) investigation was the physically inadequate no-slip condition, must be modified to account for the presence of a turbulent wall layer near the bottom. A more appropriate boundary condition which relates the bottom stress to the bottom velocity through a linear drag law, results in vertical profiles which agree quite well with the observations.

In the second model, a boundary which perfectly reflects incident Sverdrup waves was not capable of explaining nearshore barotropic tidal ellipse characteristics. Specifically, the model did not show the correct sense of current vector rotation, the correct major axis orientation angle, or the presence of onshore energy flux. A nearshore dissipative mechanism, which is due to the enhancement of frictional effects in shallow water, was modelled by an absorbing boundary condition. The resulting Sverdrup-Poincare waves successfully reproduced the features mentioned above.

Finally, by including realistic topography in a third model, it was found that the vertical wall geometry is a good approximation to reality, if it is stipulated that wavelengths are large in comparison to the topographic scale and the the region of interest is outside this scale. For the COBOLT region these conditions are met since the topographic length scale is short; about 5 km. The analysis also suggests that dissipation rates are large within the scale distance and could account for the apparent absorption of tidal energy in the coastal region.

CHAPTER IV

OBSERVATIONS OF COASTAL INTERNAL TIDES

A. Introduction

With the ability to measure deep ocean currents has come the realization that tidal frequency motions are not exclusively due to the surface or barotropic tide. Internal tides, or internal waves at tidal or near-tidal frequencies, are present in almost all oceanic current records and may even dominate velocity measurements at some locations and frequencies (Gould and McKee, 1973).

By obvious extension, much of the observational and theoretical literature of internal waves is applicable to the internal tides. The extent of this material is evident in a general review of internal waves by Briscoe (1975). In addition, the literature specific to the internal tides, much of which is devoted to the generation process, is summarized in an excellent review by Wunsch (1975).

Observations on the continental shelf and in shallow seas (see e.g., Petrie, 1975, Halpern, 1971, Lee, 1971, or Apel, et. al., 1975) show that internal tides are common--probably because nearby regions, particularly the continental slope, are areas where internal tides are generated (Prisenberg, Wilmot, and Rattray, 1974, and Cox and Sandstrom, 1962). Current measurements near the coast, however, are rare, despite theoretical interest in this so called "corner region"

(Wunsch, 1969). Measurements that have been made (Winant, 1974) are primarily concerned with freely propagating waves. Trapped internal motions, such as those of the mid-latitude diurnal tide, have been observed near topographic features such as seamounts (Hendry, 1975), however, and presumably may be important near the coast.

The presence or absence of an internal tidal signal in the COBOLT data is of relevance to the barotropic tidal analysis of chapter 2. It is well-known that velocities due to internal tides are a major source of confusion in efforts to interpret deep-ocean tidal currents (Regal and Wunsch, 1973 and Magaard and McKee, 1973). Besides the addition of energy to barotropic tidal current estimates, the intermittent nature of internal tides results in large uncertainties of both amplitudes and phases in these estimates. Also, the vertical structure of the internal tides may affect the analysis of the vertical structure of barotropic tidal parameters such as those associated with the tidal ellipse.

B. Dynamic theory of the internal tides

The analysis of the COBOLT data is strengthened by a brief exposition of the theory relevant to internal tides. The development of the theory here follows closely those given in standard texts on the subject such as Eckart (1960), Phillips (1966), or Krauss (1966). The approximations involved in formulating the model equations are similar to those made for the Laplace tidal equations (see chapter 3). The primary differences are that the fluid is no

longer considered to be homogeneous and the effects of a mean current will be included in the dynamics.

Consider then a stratified ocean with a uniform mean current U , in geostrophic equilibrium, and a mean density distribution $\rho_0(z)$, in hydrostatic equilibrium. Small deviations (indicated by lower case letters) from this mean state, such as those caused by internal waves, are governed by the linearized, incompressible, Boussinesq equations:

$$\begin{aligned} \frac{D\vec{v}}{Dt} + f\hat{k} \times \vec{v} &= -\frac{1}{\rho_0} \nabla p - \frac{\rho g}{\rho_0} \hat{k} \\ \frac{D\rho}{Dt} + w \frac{\partial \rho}{\partial z} &= 0 \\ \nabla \cdot \vec{v} &= 0, \end{aligned} \quad (1)$$

where ρ is a density perturbation such that $\rho \ll \rho_0$ and the total density is equal to the sum of ρ and ρ_0 , \hat{k} is a unit vector pointing in the $+z$ direction, and

$$\frac{D}{Dt} = \frac{\partial}{\partial t} + U \frac{\partial}{\partial x}. \quad (2)$$

The equations which relate the velocity and pressure fields are:

$$\left(\frac{D^2}{Dt^2} + f^2 \right) \vec{v} = -\frac{1}{\rho_0} \left(\frac{D}{Dt} \nabla_h p - f \hat{k} \times \nabla_h p \right)$$

(3)

and

$$\left(\frac{D^2}{Dt^2} + N^2 \right) w = -\frac{1}{\rho_0} \frac{D}{Dt} \frac{\partial p}{\partial z},$$

where ∇_h is the horizontal gradient operator $\partial / \partial x \hat{i} + \partial / \partial y \hat{j}$ and the Brunt-Vaisala frequency is defined as

$$N^2(z) = -g (\partial \rho_0 / \partial z) / \rho_0 . \quad (4)$$

Combining (1) into a single equation in the vertical velocity gives

$$\left(\frac{D^2}{Dt^2} + f^2 \right) \frac{\partial w}{\partial z} + \left(\frac{D^2}{Dt^2} + N^2 \right) \nabla_h^2 w = 0 , \quad (5)$$

with associated boundary conditions

$$w(z=0) = w(z=-H) = 0 . \quad (6)$$

This "rigid lid" approximation removes the surface wave solutions of equation (5).

C. Solutions for constant Brunt-Vaisala frequency

For constant $N^2(z) = N_0^2$ a solution to equation (5) is the plane wave,

$$w(x,y,z,t) = W_0 \exp i(kx + \ell y + mz - \tilde{\omega} t) , \quad (7)$$

where the wave vector $\vec{K} = k\hat{i} + \ell\hat{j} + m\hat{k}$, and $\tilde{\omega}$ is the wave frequency measured by a stationary observer. The boundary conditions demand a discrete set of vertical wavenumbers m

$$mH = n\pi \quad (8)$$

while substituting the solution (7) into equation (5) gives the dispersion relation,

$$((\tilde{\omega} - Uk)^2 - f^2) m^2 = (N_0^2 - (\tilde{\omega} - Uk)^2)(k^2 + \ell^2) , \quad (9)$$

In the absence of a mean current (removing the tilda from $\tilde{\omega}$ to denote this case) the dispersion relation can be further simplified for tidal frequencies and coastal regions, where $\omega^2 = 10^{-8} \text{ sec}^{-2}$ and $N_0^2 = 10^{-4} \text{ sec}^{-2}$, by assuming that $\omega^2 \ll N_0^2$. Then

$$(\omega^2 - f^2) m^2 = N_0^2 (k^2 + \ell^2) . \quad (10)$$

The similarity between this dispersion relation and that for long surface gravity waves (see chapter 3) is apparent if an "equivalent depth"

$$g h_n = (N_0/m)^2 = (N_0 H / n\pi)^2 \quad (11)$$

is defined, reducing (10) to

$$\omega^2 - f^2 = g h_n (k^2 + \ell^2) . \quad (12)$$

Because these equations are similar to the Laplace tidal equations, any solutions implicit in the tidal equations can also appear as solutions of the internal wave equations. In particular, there are free and trapped modes that are equivalent to the Sverdrup and Kelvin wave solutions of the Laplace tidal equations. From (12) it is clear that for $\omega^2 > f^2$ two possibilities exist for the wavenumbers k and ℓ --both demanding that $k^2 + \ell^2 > 0$. In the first case both k^2 and ℓ^2 are positive and freely propagating internal

waves result. In the second case $\ell^2 < 0$ and $|\ell^2| < |k^2|$, imply exponential decay or growth for the solution (7).

For $\omega^2 < f^2$ only one possibility exists-- $\ell^2 < 0$ and $|\ell^2| > |k^2|$ --implying waves of this frequency range do not propagate freely in the y-direction but are trapped to a boundary such as the coast. In addition, the wavelengths of both free and trapped internal motions are considerably smaller than the equivalent surface waves since

$$g h_n = (N_0 H / n\pi)^2 \ll gH. \quad (13)$$

Taking $N_0^2 = 10^{-4} \text{ sec}^{-2}$ and $H = 30 \text{ m}$, for example, suggests that first mode ($n = 1$) internal waves should have wavelengths of about 10 km--a factor of 100 less than the equivalent surface wavelengths.

D. Solutions for an arbitrarily stratified fluid

For an arbitrarily stratified fluid equation (5) has a solution

$$w(x, y, z, t) = W(z) \exp i(kx + \ell y - \omega t), \quad (14)$$

if (with $\omega^2 \ll N^2$ and notation of equation (16) retained)

$$\frac{d^2 W}{dz^2} + \frac{N^2(z) K^2}{\omega^2 - f^2} W = 0, \quad (15)$$

where $\vec{K} = \hat{k}i + \hat{\ell}j$ is now the horizontal wave vector ($|\vec{K}| = K$) and the boundary conditions of equation (6) remain. This is a classical

eigenvalue problem whose solutions are a countable number of eigenfunctions, $F_n(z)$, each with an associated eigenvalue K_n . These eigenvalues and eigenfunctions, for arbitrary $N^2(z)$, can be computed numerically by one of any number of integration techniques. One such method, a matrix diagonalization technique, is described by Krol (1974). The rigid lid boundary conditions also assure that eigenfunctions are orthogonal,

$$\begin{aligned} \frac{K_n^2}{\omega^2 - f^2} \int_0^H N^2(z) W_n^2(z) dz &= \int_0^H \left(\frac{dW_n}{dz} \right)^2 dz \\ \int_0^H N^2(z) W_m(z) W_n(z) dz &= 0 \\ \int_0^H \frac{dW_m}{dz} \frac{dW_n}{dz} dz &= 0 \quad \text{for } m \neq n. \end{aligned} \quad (16)$$

Other perturbation fields are related to the eigenfunctions by

$$\begin{aligned} u_n(z) &= i \frac{\omega k + i f l}{\omega K_n^2} \frac{dW_n}{dz} \\ v_n(z) &= i \frac{\omega l - i f k}{\omega K_n^2} \frac{dW_n}{dz} \\ p_n(z) &= i \rho_0 \frac{\omega^2 - f^2}{\omega K_n^2} \frac{dW_n}{dz} \\ \rho_n(z) &= i \rho_0 \frac{N^2(z)}{g \omega} W_n(z). \end{aligned} \quad (17)$$

Important relationships defining the amplitude ratios and relative phases between the various measured quantities can be developed from (17). For trapped waves, where $k^2 < 0$,

$$\frac{u_n}{v_n} = i \frac{\omega k + f \lambda}{\omega \lambda + f k}$$

$$\frac{u_n}{\rho_n} = g \frac{\omega k + f \lambda}{\rho_0 K_n^2 N^2} \frac{1}{W_n} \frac{dW_n}{dz}, \quad (18)$$

where the decay parameter has been redefined as: $\lambda = -i\ell$. Comparable equations for free waves are found by taking $\lambda = 0$ since the direction of propagation is arbitrary.

The phase relation between the velocity in the direction of propagation (u) and that perpendicular to it (v) is 90° for both types of waves, while the phase relation between u and ρ is either 0° or 180° depending on the sign of dW_n/dz . These phases are an important consideration in determining the propagation direction of the internal wave.

The energetics of an internal wave field are examined by multiplying the momentum equation by v , the continuity equation by $-p$, and the density conservation equation by $\rho g/N^2$, and adding the results to obtain the energy conservation equation,

$$\frac{\rho_0}{2} \frac{D}{Dt} (u^2 + v^2 + w^2 + (\rho g/\rho_0)^2/N^2) + \nabla \cdot p\vec{v} = 0. \quad (19)$$

Making the assumption that $\omega^2 \ll N^2$ allows one to disregard the vertical kinetic energy, w^2 . Integrating (19) over the water

column and performing a time average (indicated by brackets $\langle \rangle$) results in slightly different expressions for free and trapped waves when the relations of equation (17) are substituted into (19):

$$\begin{aligned}
 \text{KINETIC ENERGY} &= \frac{\rho_0}{4} \int (\langle u^2 \rangle + \langle v^2 \rangle) dz = \\
 &= \frac{1}{4} \frac{\omega^2 + f^2}{\omega^2 K^2} \int \left(\frac{dW_n}{dz} \right)^2 dz && \text{FREE} \\
 &= \frac{1}{4} \frac{(\omega k + f\lambda)^2 + (\omega\lambda + fk)^2}{\omega^2 K^4} \int \left(\frac{dW_n}{dz} \right)^2 dz && \text{TRAPPED} \\
 \\
 \text{POTENTIAL ENERGY} &= \frac{\rho_0}{4} \int \langle (g \rho / \rho_0)^2 \rangle / N^2 dz = && (20) \\
 &= \frac{1}{4\omega^2} \int N^2 W_n^2 dz && \begin{array}{l} \text{FREE} \\ \& \text{TRAPPED} \end{array} \\
 \\
 \text{ENERGY FLUX} &= 1/2 \int \langle pv \rangle dz = \\
 &= \rho_0 \frac{1}{2\omega K^2} (k \hat{i} + \lambda \hat{j}) \int N^2 W_n^2 dz && \text{FREE} \\
 &= \rho_0 \frac{\omega k + f\lambda}{2\omega^2 K^2} \hat{i} \int N^2 W_n^2 dz && \text{TRAPPED}
 \end{aligned}$$

(Note that there is no vertical energy flux in the modal description of internal waves.) The ratio of potential to horizontal kinetic energy, another important diagnostic quantity, is

$$\frac{\text{P.E.}}{\text{K.E.}} = \frac{\omega^2 - f^2}{\omega^2 + f^2} \quad \text{FREE} \quad (21)$$

$$= \frac{(\omega^2 - f^2)(k^2 - \ell^2)}{(\omega k + f\lambda)^2(\omega\lambda + fk)^2} \quad \text{TRAPPED.} \quad (21)$$

cont.

Finally, the total energy for both wave types is

$$E = \text{K.E.} + \text{P.E.} = \frac{1}{2(\omega^2 - f^2)} \int N^2 W_{\text{H}}^2 dz \quad \text{FREE} \quad (22)$$

$$= \frac{1}{4\omega^2} \left[\frac{(\omega k + f\lambda)^2 + (\omega\lambda + fk)^2}{K^2(\omega^2 - f^2)} + 1 \right] \int N^2 W^2 dz \quad \text{TRAPPED.}$$

This quantity, the total energy per unit surface area, is that energy carried along by a wave packet. Consequently

$$\rho \vec{v} = E \vec{C}, \quad (23)$$

where \vec{C} is the group velocity,

$$\vec{C} = \partial\omega/\partial k \hat{i} + \partial\omega/\partial \ell \hat{j} + \partial\omega/\partial m \hat{k}. \quad (24)$$

E. The mean fields of the COBOLT experiment

The average sigma-t cross section formed from the twenty-two days of profiling that coincided with the buoy measurements is shown in figure 1. The most noticeable feature is a fairly distinct pycnocline about 12 m deep which broadens toward the shore. Because this feature exists in the individual daily cross sections, it is reasonable to assume that this reduction of stratification is due to some physical process (such as the enhanced mixing) and is not solely an artifact of the averaging procedure.

MAY 1977 AVERAGE

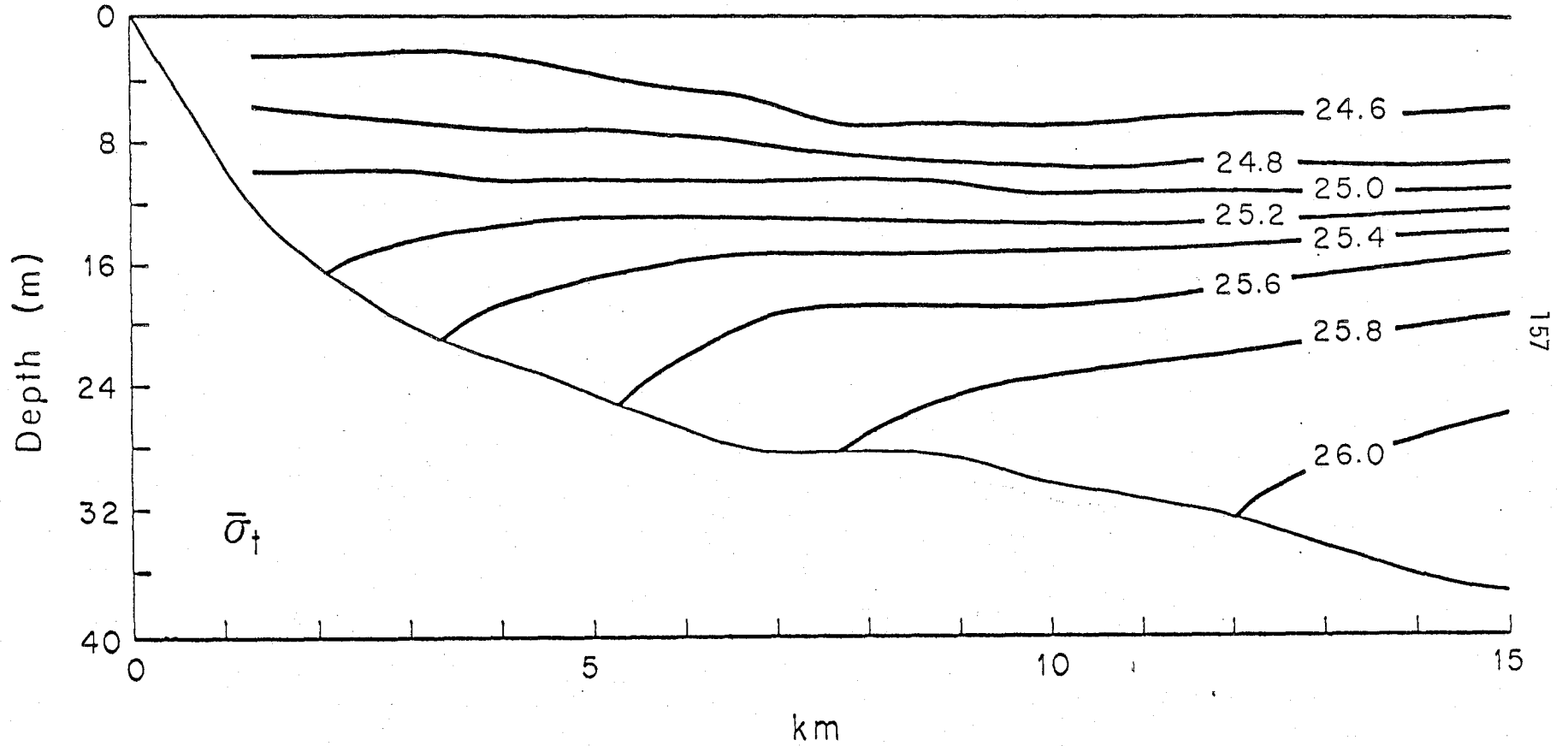


Figure 4-1 Twenty-two day average sigma-t cross section at the COBOLT site

The numerical values of temperature, salinity, and sigma-t at the location of spar buoy 3 are listed in table 1. To determine as representative a profile as possible the twenty-two day average profiles of the two transect stations located on either side of a given mooring (averages were also performed for buoys 2 and 4) were combined to make the estimates in the table. Also included in the table are the standard deviations of the averaged temperatures and salinities.

These profiles suggest that density during the month of May was primarily controlled by the salinity. This can be checked quantitatively by noting that the partial derivatives of density with respect to temperature and salinity (obtained directly from the equation of state) are quite different, i.e.,

$$\begin{aligned} \frac{\partial \rho}{\partial S} &= 7.5 \times 10^{-4} \frac{\text{gm}}{\text{cm}^3 \text{ o/oo}} \\ \frac{\partial \rho}{\partial T} &= -1.4 \times 10^{-4} \frac{\text{gm}}{\text{cm}^3 \text{ o/oo}}, \end{aligned} \quad (25)$$

at $T = 8^\circ$ and $S = 32 \text{ o/oo}$. At buoy 3 a temperature contrast across the thermocline of about 3° results in a density change of $4.2 \times 10^{-4} \text{ gm/cm}^3$. The salinity change was about 1 o/oo across the halocline giving a density change of $7.5 \times 10^{-4} \text{ gm/cm}^3$ --almost twice as great as that due to temperature. The late-spring measurement period and the large amounts of fresh water discharge from the Connecticut River (Ketchum and Corwin, 1964) are probably responsible for this result.

TABLE 4-1

NUMERICAL VALUES OF T, S, SIGMA T, AND N²

AT BUOY 3

DEPTH	TEMP. (°C)	SALIN. (‰)	SIGMA T	N ² (SEC ⁻²)	PERIOD (MIN)
1	10.71	31.96	24.46		
2	10.68	31.96	24.46	0.73x10 ⁻⁴	12
3	10.60	31.97	24.48	1.78	8
4	10.50	31.98	24.51	2.27	7
5	10.39	31.99	24.54	2.85	6
6	10.26	32.01	24.58	3.99	5
7	10.08	32.05	24.63	5.49	4
8	9.86	32.09	24.70	6.86	4
9	9.63	32.15	24.78	7.86	4
10	9.40	32.21	24.87	8.57	4
11	9.17	32.28	24.96	9.14	3
12	8.94	32.36	25.06	9.60	3
13	8.70	32.44	25.16	9.75	3
14	8.46	32.52	25.26	9.32	3
15	8.25	32.59	25.34	8.37	4
16	8.07	32.65	25.41	7.23	4
17	7.92	32.70	25.48	6.17	4
18	7.80	32.75	25.53	5.27	5
19	7.67	32.78	25.58	4.54	5
20	7.56	32.81	25.62	3.97	5
21	7.47	32.85	25.65	3.58	6
22	7.40	32.88	25.69	3.34	6
23	7.32	32.90	25.72	3.11	6
24	7.23	32.92	25.75	2.76	6
25	7.15	32.94	25.77	2.30	7
26	7.08	32.95	25.79	1.87	8
27	7.02	32.96	25.81	1.67	8
28	6.97	32.97	25.83	1.76	8
29	6.91	32.99	25.85	2.01	7
30	6.86	33.01	25.87	1.89	8
31	6.84	33.02	25.87	0.81	12
Standard deviation:	1.5	0.1			

Also included in table 1 (and displayed in figure 2 for all three mooring locations) are the values of the Brunt-Vaisala frequency. The equivalent periods are quite short--generally less than ten minutes--implying that resolution of high frequency internal waves is not possible because of the one hour buoy averaging period. However, high frequency internal waves will not alias the low frequency signals either.

The COBOLT instruments also recorded significant mean currents. Onshore mean currents are generally quite small (less than 2 cm/sec) and can be ignored as an influence on internal tides. The alongshore mean currents, presented in table 2 for two different averaging intervals, are substantially stronger than onshore currents and more comparable to the phase speed of internal waves. These currents flowed to the west during the experiment, and, given the distance to Montauk Point and the entrance to Long Island Sound (60 km), suggest an upper layer advective time scale of 7-14 days.

Although the measurement period over which these averages were made was quite variable, it appears that the major time scales have been included. Figure 3, showing the salinity time series of buoy 3 at 3.8m and 25.0m (instruments 31 and 34), illustrates the abrupt changes measured during the experiment. On May 10 a large storm crossed the site causing the water column to become practically homogeneous. Higher salinities then persisted at the surface for approximately ten days, until May 20, when the salinity changed sharply from about 32.5 o/oo to 31.7 o/oo. This freshening is

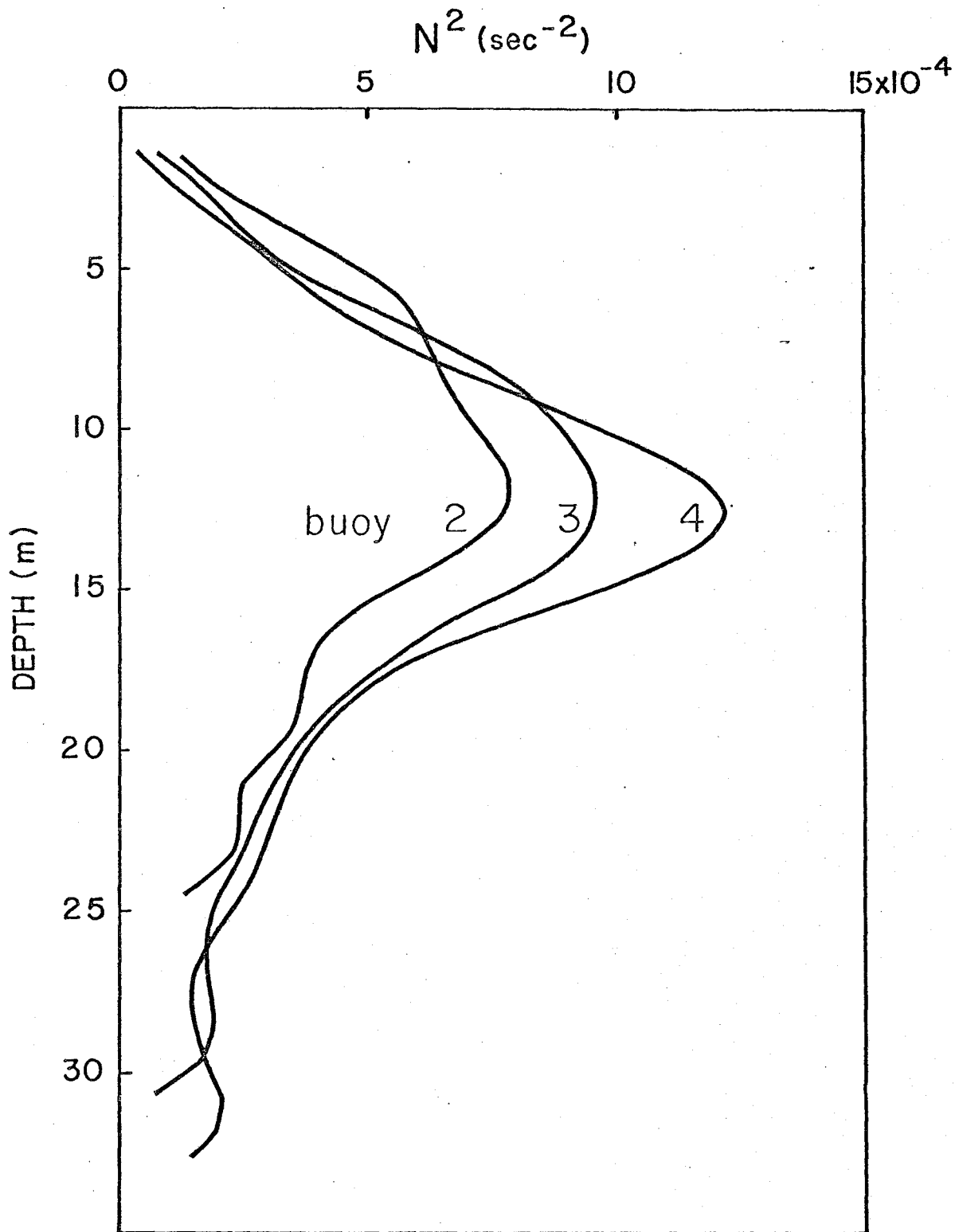


Figure 4-2 Twenty-two day average Brunt-Vaisala frequency profiles at buoys 2, 3 and 4

TABLE 4-2

MEAN ALONGSHORE CURRENTS

FOR BUOYS 2, 3, & 4;

MAY 1977

CURRENTS AT BUOY NO.

	<u>2</u>	<u>3</u>	<u>4</u>
	APR. 30-MAY 15		
LEVEL 1	-4.5 cm/sec	-	-11.9 cm/sec
2	-6.2	-10.5	-10.2
3	-2.8	-6.6	-7.4
4	-0.6	-2.4	-2.6

APR. 30-MAY 25

LEVEL 1	-3.2 cm/sec	-
2	-5.6	-8.2
3	-2.9	-5.0
4	-1.2	-2.3

*Negative values are to the west

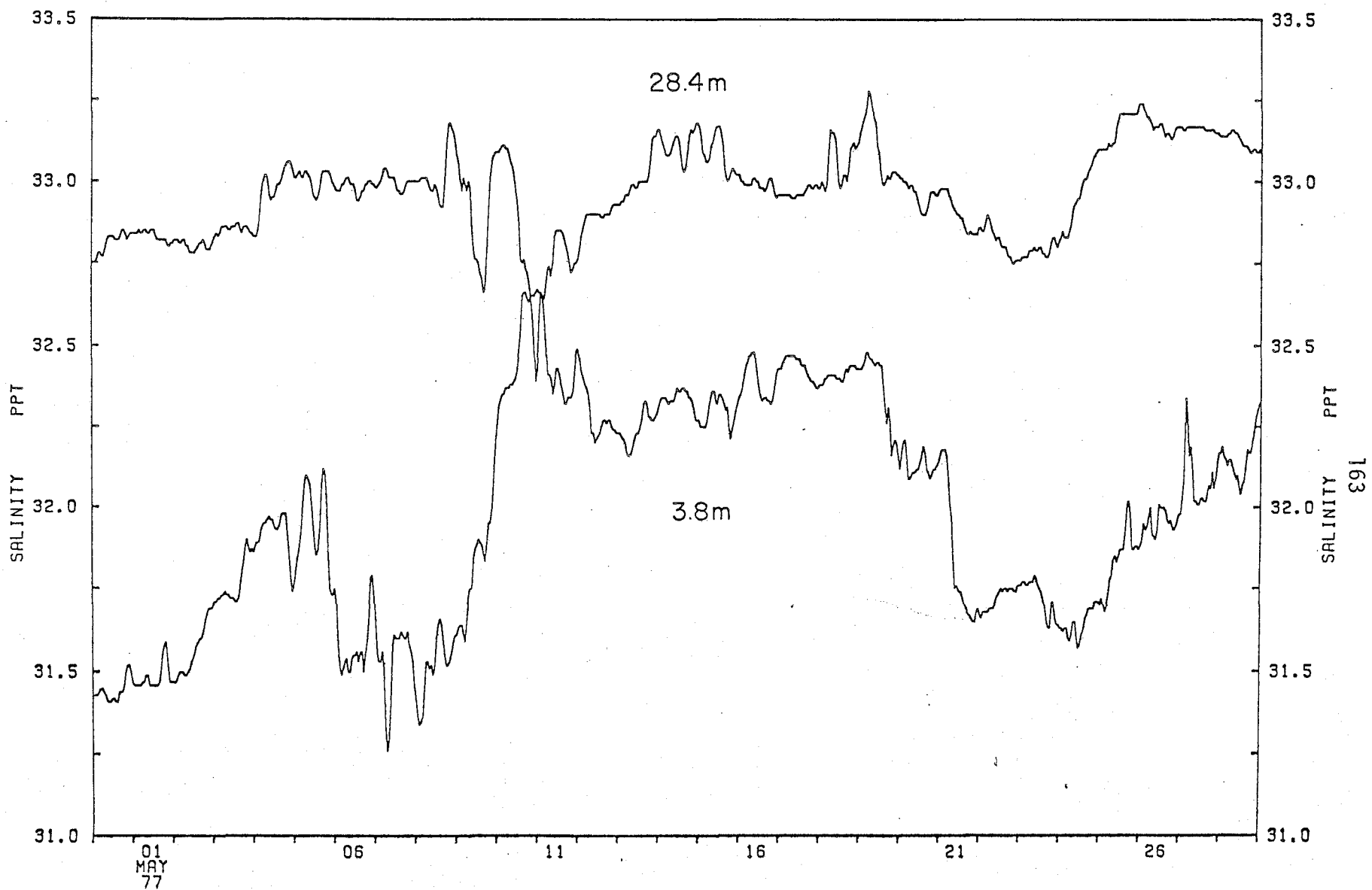


Figure 4-3 Salinity time series from instruments 31 and 34

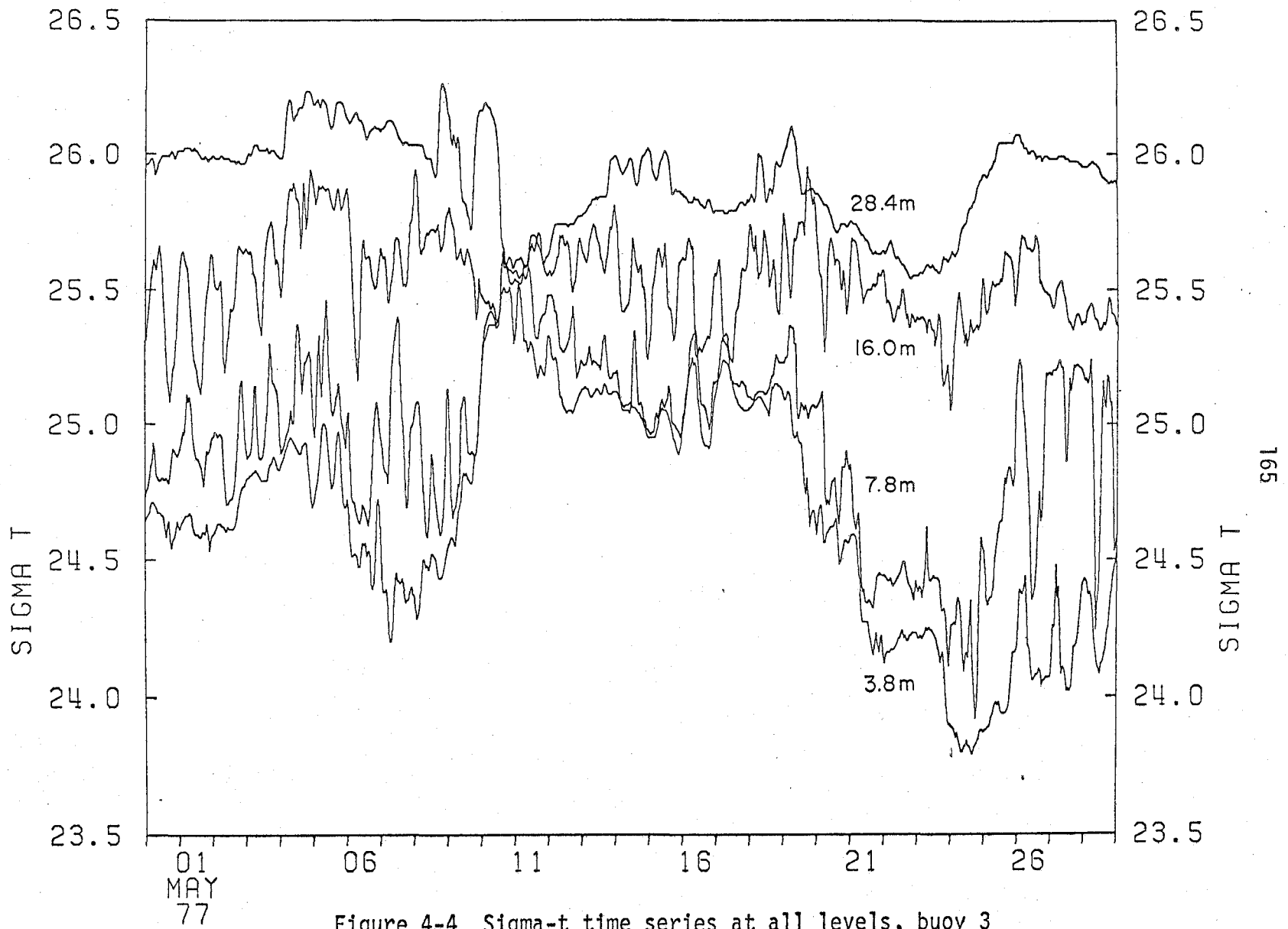
probably due to an influx of water from Long Island Sound (the nearest and most logical source of fresh water). Furthermore, the ten day time estimate obtained from the salinity series agrees with the advective time scale suggested by the mean currents and supports the notion that a thirty day averaging period is reasonably representative.

F. Internal tidal oscillations

The COBOLT experiment is well-suited for observations of the internal tides. The three kilometer spacing of moorings was intended to provide a coherent array for internal (albeit very low frequency) motions. While the orientation of the transect line (i.e., perpendicular to shore) limits directional sensitivity to the offshore direction, the propagation of free waves is probably biased in this direction by the local topography.

The sigma-t time series of all four instruments on buoy 3 (figure 4) shows plainly the variations of interest here: the internal tides. The large regular oscillations at instruments 32 and 33 are typical of measurements near the pycnocline while smaller oscillations at instruments 32 and 33 indicate reduced stratification and adjustment to top and bottom boundaries.

To identify the major periodicities of pycnocline oscillations, energy spectra of sigma-t time series were computed. Figure 5 shows the averaged sigma-t energy density of instruments 21-23 and 31-33 for the twenty-five day period over which both buoys were operational



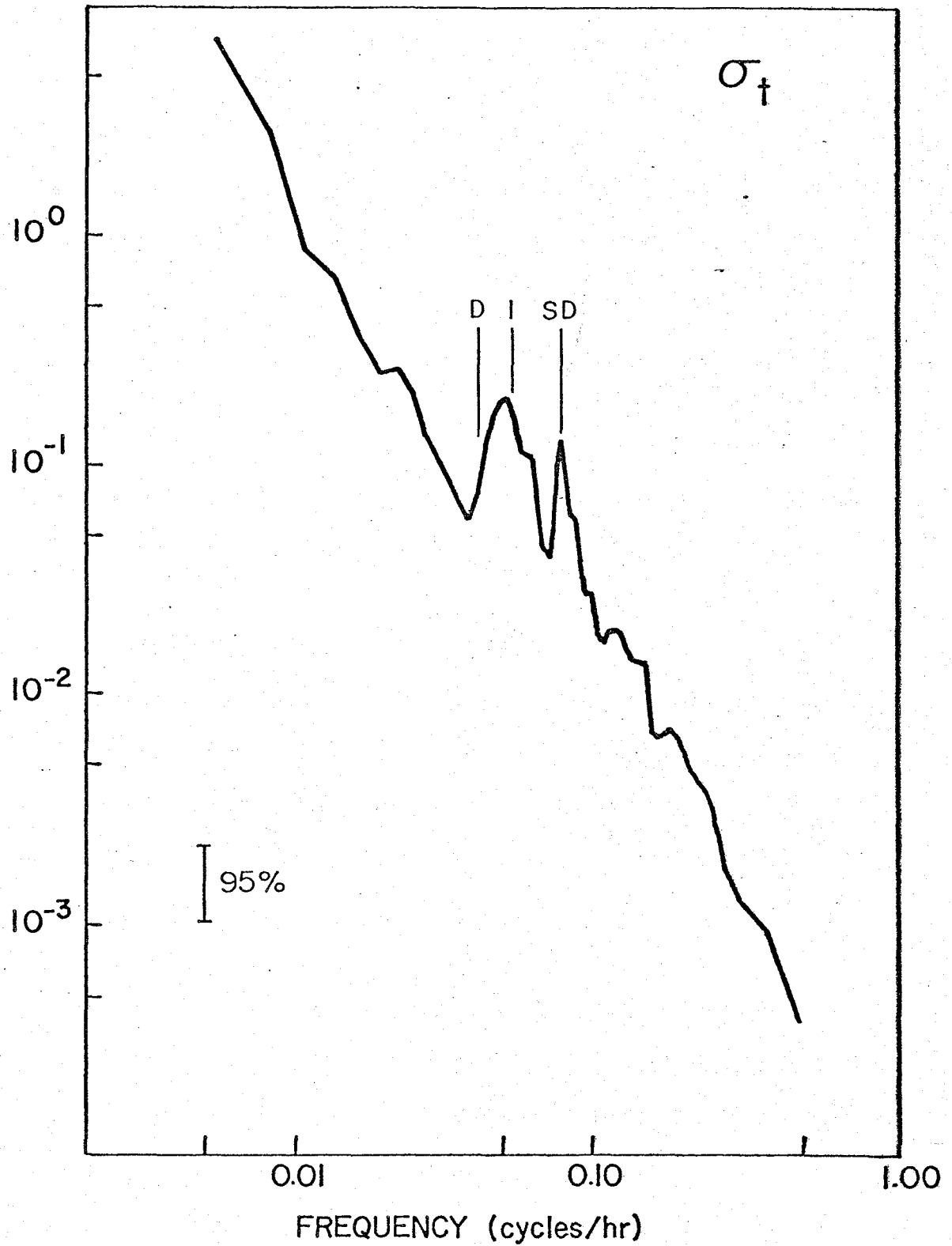


Figure 4-5 Sigma-t energy density spectrum from insts. 21-23 & 31-33

(April 30-May 24), with the values of diurnal ($D = 24.00$ hr), local inertial (18.35 hr), and semidiurnal (12.42 hr) frequencies included for reference. These instruments were selected as representative of upper layer and pycnocline fluctuations. The internal oscillations have two resolved maxima at which energy rises above the background level: a broad peak centered around the inertial frequency and a sharp peak centered on the principal semidiurnal frequency. Because the "inertial" peak is so much broader than that at semidiurnal frequencies, it contains almost three times as much energy and accounts for most of the regular oscillations that catch the eye in figure 4. By contrast, the temperature spectrum from the same instrument packages (figure 6) does not show any energy significantly above the continuum.

Further insight into the nature of the internal oscillations can be obtained by examining the kinetic energy spectrum. A comparison of the energy density of onshore velocities (figure 7) with that of alongshore velocities (figure 8) shows a marked disparity. Onshore energy is much less than alongshore energy for both diurnal and semidiurnal frequency ranges, but not for frequencies near inertial. In fact, alongshore currents are almost ten times as energetic as onshore currents for the semidiurnal band and almost three times as energetic for the diurnal. Currents in the inertial range, on the other hand, have comparable energies in both directions.

A convenient way to characterize the sigma-t variations is to convert the energy in a particular frequency band to an equivalent isopycnal displacement using the differential

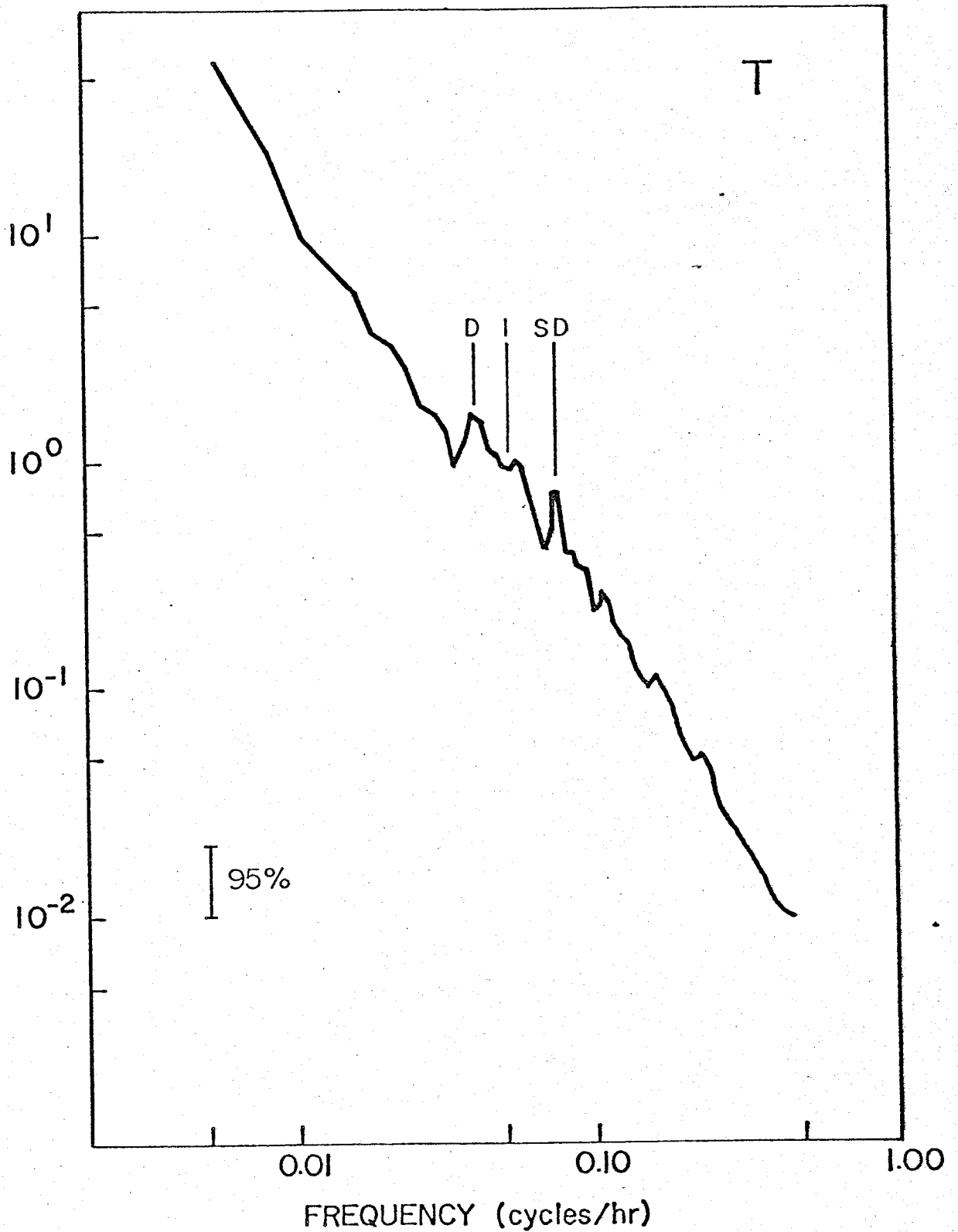


Figure 4-6 Temperature energy density spectrum from insts. 21-23 & 31-33

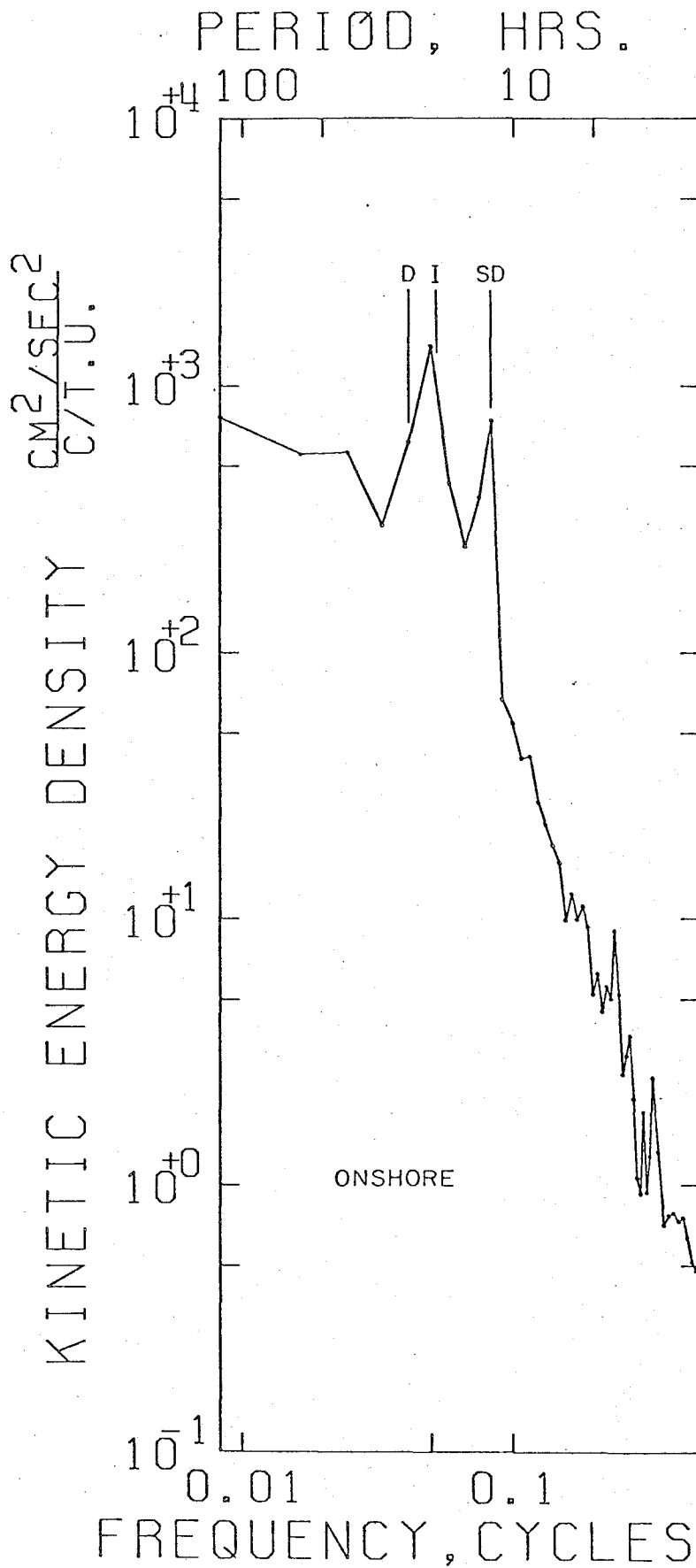


Figure 4-7

Onshore velocity energy density spectrum from insts. 32 and 33

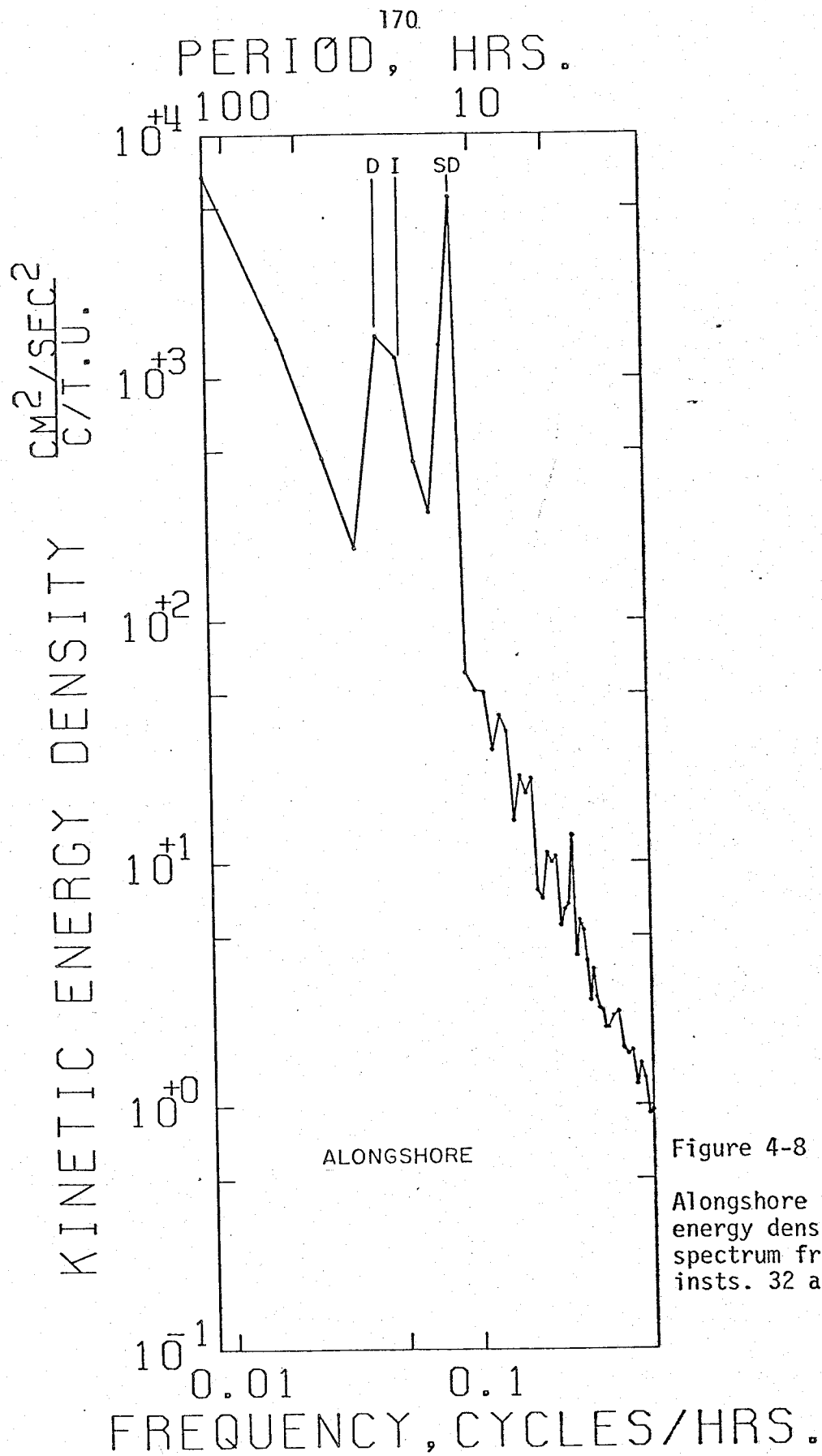


Figure 4-8

Alongshore velocity
energy density
spectrum from
insts. 32 and 33

$$\Delta\sigma = \partial\sigma/\partial z \Delta z = N^2 \Delta\zeta . \quad (26)$$

These quantities are averaged for buoys 2 and 3 at each instrument level and presented for the three periods of interest in table 3 with the isopycnal displacement expected for a long surface wave of 100 cm amplitude. This last item is computed by assuming that the vertical velocity decreases linearly to zero at the bottom and that it is equal to the time derivative of the displacement, i.e.,

$$w(z) = a\omega (H-z)/H$$

and

(27)

$$\partial\zeta/\partial t = w(z) ,$$

where a is the amplitude of the surface wave, ζ is the isopycnal displacement, and H is the depth of the water. Since the semidiurnal surface tide has an amplitude of about 1 m in the COBOLT region and the diurnal surface tide an amplitude of about 10 cm, these numbers give a fair indication of the isopycnal displacements due to surface tides alone.

A comparison of the measured and computed displacements shows to what degree the surface tide can account for the sigma-t variations at each frequency. In the semidiurnal band displacements due to the surface tide and those computed from density variations are virtually identical (except for instruments at level 4 where energy peaks fade into the continuum) implying that the narrow energy peak at this

TABLE 4-3

ISOPYCNAL DISPLACEMENTS

FOR BUOYS 2 & 3;

ALL LEVELS

INST	N ²	24 HR.		18 HR.		12 HR.	
		(CM)	(CM)	(CM)	(CM)	(CM)	(CM)
21	3.3×10^{-4}	102	3.9×10^{-2}	70	2.3×10^{-2}	73	2.4×10^{-2}
22	6.2	45	2.8	79	4.9	71	4.4
23	4.8	50	2.4	100	4.8	52	2.5
24	2.4	96	2.3	67	1.6	42	1.0
31	2.3	170	4.0	130	3.1	91	2.1
32	6.9	62	4.3	78	5.4	78	5.4
33	7.2	60	4.3	86	6.2	60	4.3
34	2.0	180	3.5	65	1.3	110	2.2

DISPLACEMENTS FROM SURFACE WAVE

WITH 1 METER AMPLITUDE

<u>LEVEL</u>	<u>DEPTH</u>	<u>$\Delta\zeta$</u>
1	4 m	87 cm
2	8	73
3	16	53
4	25	17

frequency is almost exclusively a consequence of the barotropic tide. The diurnal band displacements, however, are 5-10 times greater than can be expected from surface wave contributions and therefore must be in part due to the baroclinic tide. And finally, since there is no surface displacement around 18 hours, it is reasonable to assume that all of this energy is baroclinic in nature. In this sense the large horizontal scale (barotropic) and small horizontal scale (baroclinic) fluctuations are sorted by frequencies in the May experiment.

This sorting of dynamics does not always occur. Unlike the May 1977 experiment, where kinetic energy is found in a broad band at and above diurnal frequencies, a comparable spectrum of kinetic energy density for the September 1975 experiment (figure 9) shows energy spread fairly symmetrically about 24 hours, and not as high as the inertial frequency. The semidiurnal energy peak is again very sharp, as in May, 1977, and is centered at 12.42 hours.

G. Modal structure of the internal tides

It is possible to discriminate between barotropic and baroclinic flows, and between the different modes of baroclinic motions, by examining the modal structure of the currents computed from the density distribution (see table 1). Consider, for example, the first three vertical velocity eigenfunctions, $W_n(z)$, computed from the density distribution at buoy 3 by the procedure outlined by Krol (1974). These modes (figure 10) generally have large amplitudes

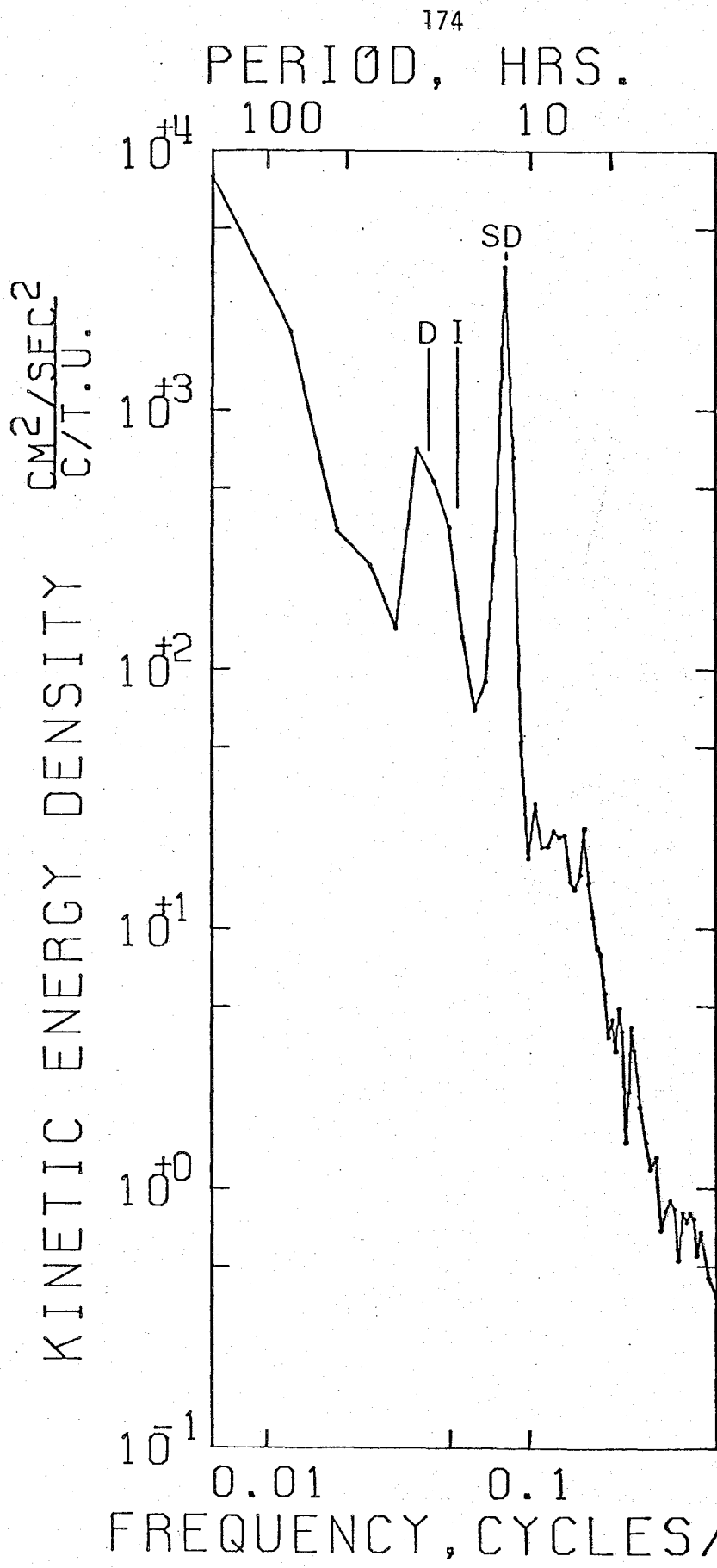


Figure 4-9
Kinetic energy density at 15 m for September, 1975 experiment

VERTICAL MODES

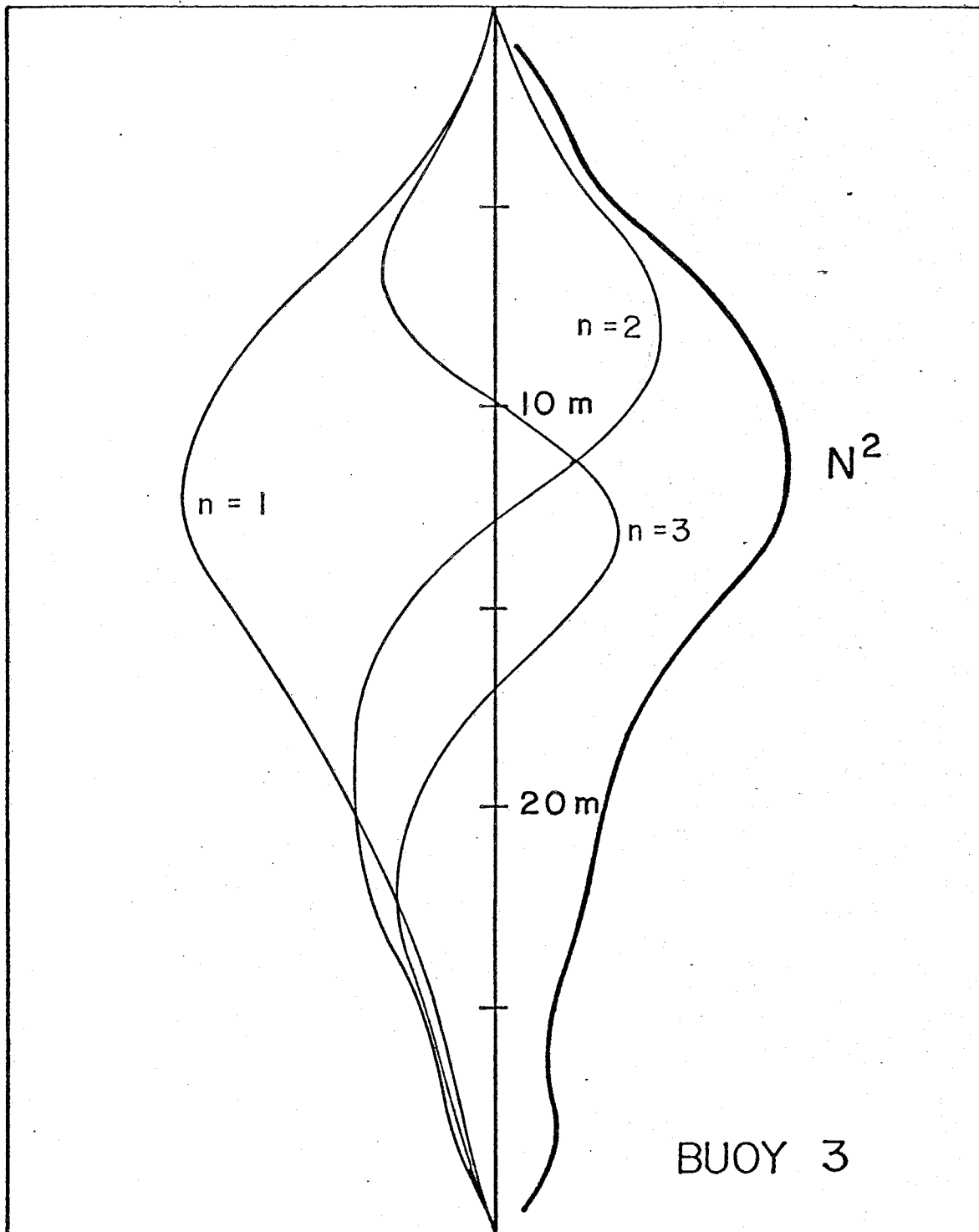


Figure 4-10 First three vertical velocity modes at buoy 3

where N^2 is large, i.e. in the pycnocline, and smaller amplitudes toward the top and bottom, where N^2 weakens and the vertical velocity adjusts to the boundaries. These are the features that are evident in the sigma-t variations of the COBOLT experiment.

The horizontal velocity modes, which are proportional to dW_n/dz , are shown in figure 11. Unlike vertical velocities, which must be extrapolated from other fields, the horizontal velocities are directly measured quantities and can be used in a straightforward manner in interpreting the distribution of energy among the modes.

The COBOLT data were analyzed by fitting the calculated eigenfunctions to the observed velocities in a least squares sense. Given a continuous eigenfunction $U_n(z) = dW_n/dz$ and velocity measurements u_i at each of M different points in the vertical, it is possible to determine a coefficient a_n , for each mode, such that

$$\sum (u_i - a_n U_n(z_i))^2 h_i \quad (28)$$

is a minimum. The weighting factors, h_i , are chosen by the trapezoid integration rule to favor instruments that cover a large vertical range. Minimizing (28) with respect to a_n determines the values of the coefficients,

$$a_n = \frac{\sum_{i=1}^M \frac{h_i u_i U_n(z_i)}{h_i U_n^2(z_i)}}{\sum_{i=1}^M \frac{h_i U_n^2(z_i)}{h_i U_n^2(z_i)}} \quad (29)$$

Because the eigenfunctions have arbitrary amplitudes, a more useful

HORIZONTAL MODES

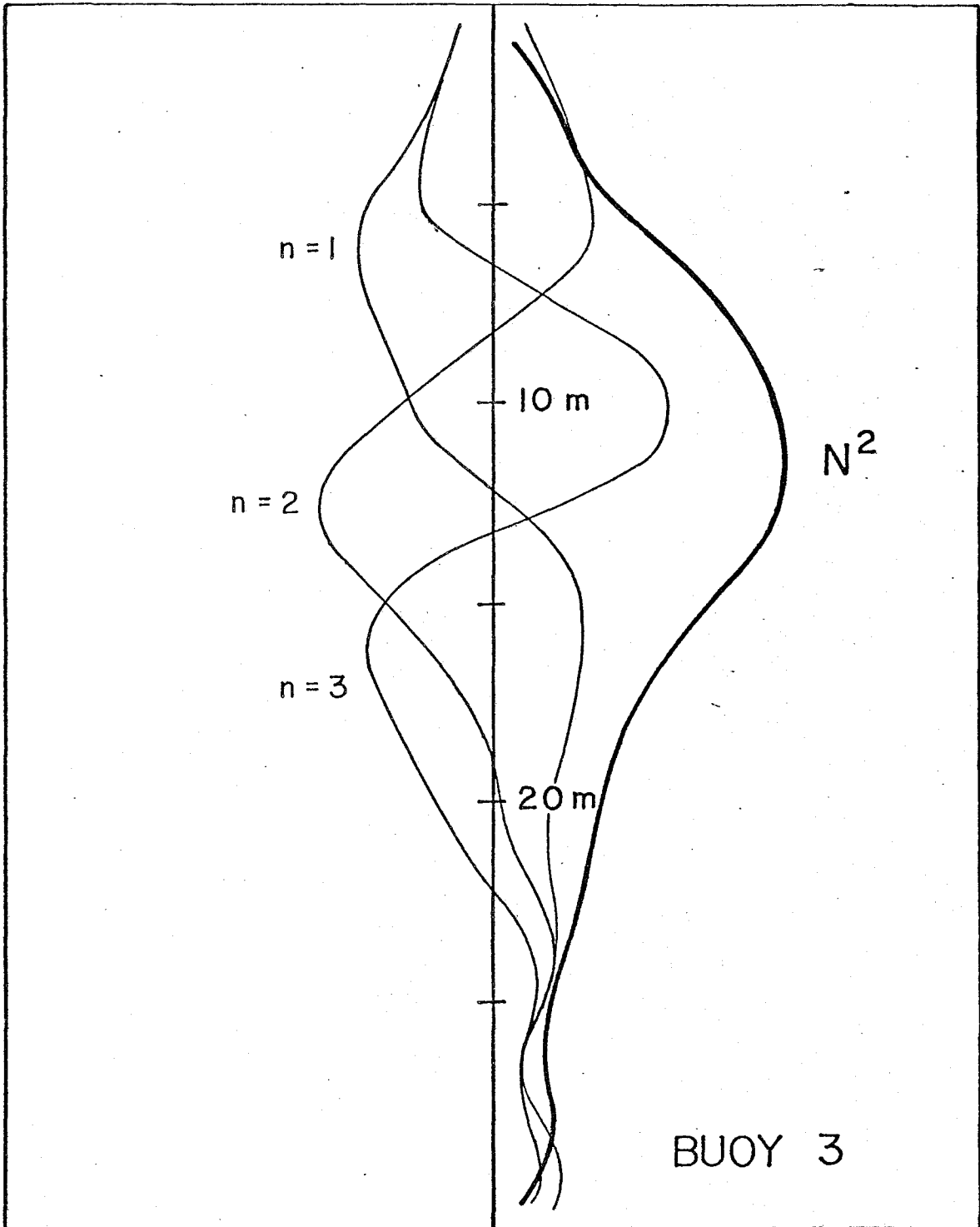


Figure 4-11 First three horizontal modes at buoy 3

quantity is the ratio of the fitted eigenfunction variance to the observed variance,

$$P_n = \sum_{i=1}^M \frac{h_i a_n^2 U_n^2(z_i)}{h_i u_i^2}, \quad (30)$$

which is expressed as the percentage of observed variance (or energy) that can be accounted for by a fit of the n^{th} eigenfunction.

The results of the eigenfunction analysis and mode fitting for three different frequency bands are summarized in table 4. With only four instruments measuring velocity (three at buoy 3) a fit of more than four modes is not possible. In practice it was found that the barotropic ($n = 0$) and first two baroclinic modes ($n = 1$ & 2) accounted for virtually all the variance, so fitting of higher order modes was not necessary.

Table 4 confirms the results of the isopycnal displacement analysis by showing: that the vertical variance in the 12 hr band is largely barotropic; the variance in the 18 hr band is largely baroclinic; and, that the variance in the 24 hr band is mixed. The table also shows that onshore velocities at 12 and 24 hr have a higher percentage of variance in the baroclinic modes than do alongshore velocities.

The mode fitting of 18 hour variance is consistent with the assertion that energy in this band is internal tidal energy that has been Doppler-shifted away from the diurnal band, since 80-95% of the variance at all three COBOLT moorings can be attributed to the first

TABLE 4-4

PERCENTAGE OF VARIANCE IN
BAROTROPIC AND FIRST TWO BAROCLINIC
MODES

B U O Y	M O D E	% AT 12 HR.			% AT 18 HR.			% AT 24 HR.			WAVE LENGTH (KM.)	
		NO.	EA.	T	NO.	EA.	T	NO.	EA.	T	12 HR.	24 HR.
				0			0			0		
2	0	55	95	90	1	0	1	5	87	63		
	1	16	2	3	97	99	98	90	9	33	12	17
	2	0	0	0	0	0	0	2	0	1	5	7
3	0	81	96	95	2	0	1	4	90	64		
	1	3	1	1	89	95	92	82	4	28	15	22
	2	6	1	2	2	0	1	6	2	3	6	9
4	0	44	94	86	2	4	3	11	71	51		
	1	33	1	6	81	81	81	55	9	24	16	23
	2	1	0	0	0	0	0	1	0	0	7	9

NO. = Onshore component

EA. = Alongshore Component

TOT. = Total variance

baroclinic mode. The 18 hr velocities at buoy 2 and the fitted first mode, shown together in figures 12 and 13, visually confirm the baroclinic nature of this frequency band.

The modal analysis also supplies the magnitude of the eigenvalue, $K_n = (2\pi/\text{wavelength})$. These wavelengths (see table 4) are approximately 15 km for the first internal mode in the COBOLT region, and around 5 km for the second internal mode.

For trapped waves, more information is needed to determine the wavelength--i.e., there must be some method of choosing the decay scale or e-folding distance. Traditionally the Kelvin wave problem is modelled in an ocean with a vertical wall and no-normal-flow boundary condition. Equation (17) shows that this condition (assuming y is the onshore direction),

$$v \propto \omega \lambda - i f k = -i (\omega \lambda + f k), \quad (31)$$

demands that

$$\lambda = - f k / \omega, \quad (32)$$

so that the eigenvalue is

$$\frac{K_n^2}{\omega^2 - f^2} = \frac{k_n^2}{\omega^2}. \quad (33)$$

As a result, the wavelength of a first mode semidiurnal internal Kelvin wave is almost half that of a free wave. In comparison, a first mode diurnal internal Kelvin wave has a wavelength of around 20 km. Furthermore, it is necessary, in order to have exponential offshore decay, for these wave to propagate alongshore to the west (the negative x direction)--the same direction as the mean current.

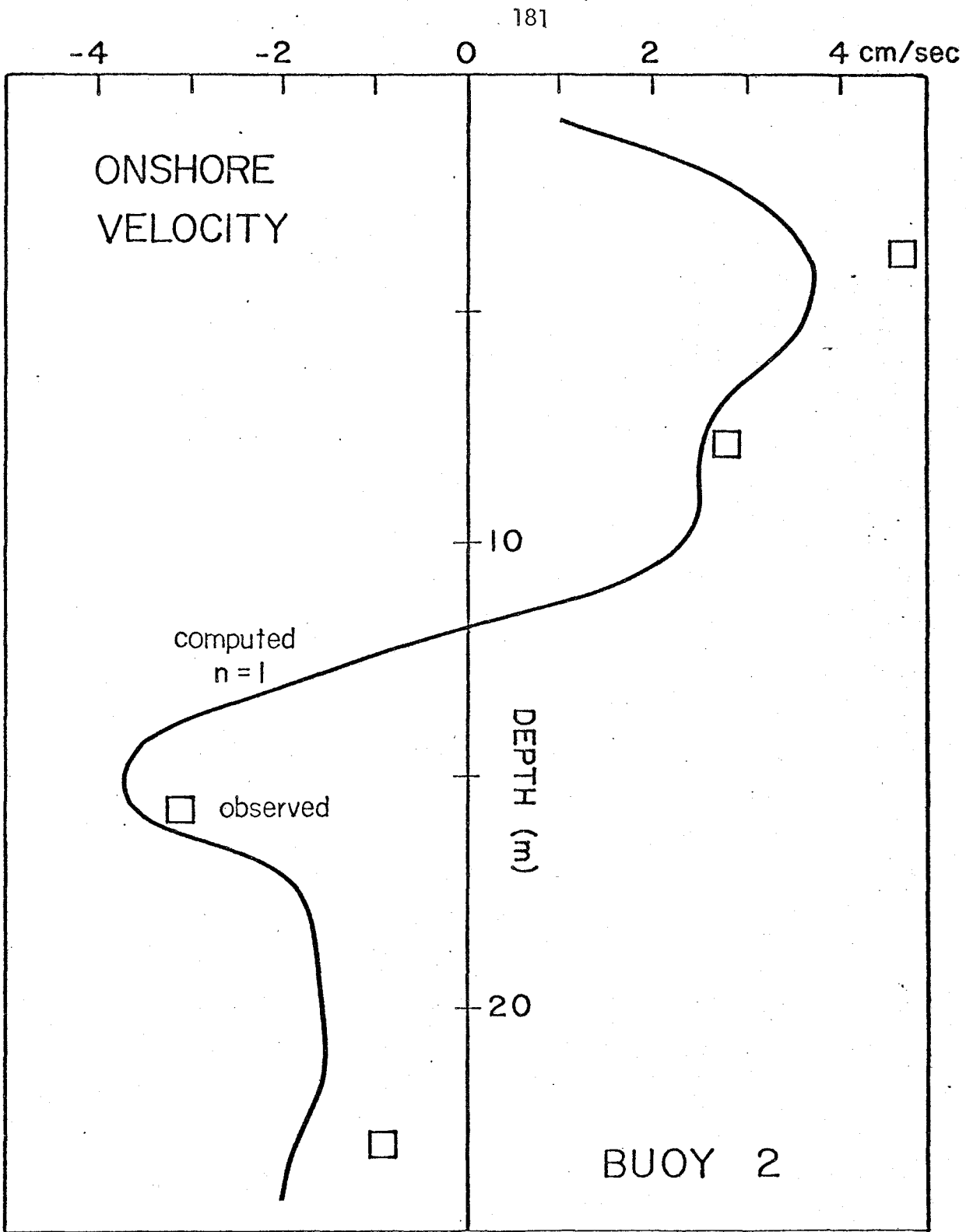


Figure 4-12 Fitted first baroclinic mode at buoy 2: onshore velocities

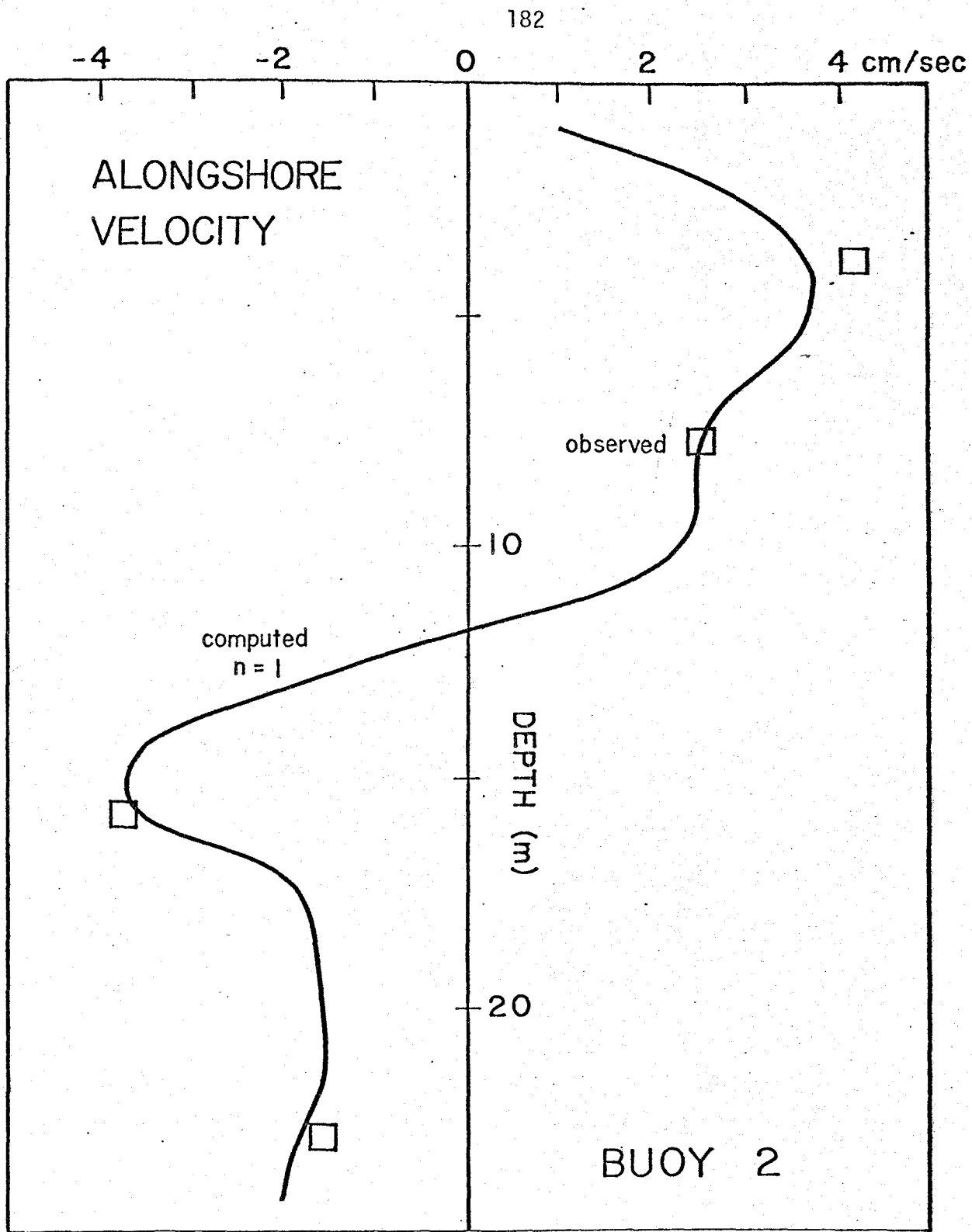


Figure 4-13 Fitted first baroclinic mode at buoy 2: alongshore velocities

H. Comparison to theory

This last fact makes the internal Kelvin wave particularly subject to Doppler shifting. The frequency of a diurnal internal Kelvin wave superimposed on a mean current of 10 cm/sec would be measured by a stationary observer as

$$\begin{aligned}\tilde{\omega} &= \omega + Uk = 1/24 \text{ hr} + 10 \text{ cm/sec} \times 1/20 \text{ km} = \\ &= 1/17 \text{ hr} .\end{aligned}\tag{34}$$

This estimate, using realistic values for all of the parameters, results in a Doppler-shifted frequency that is remarkably close to the sigma-t energy maximum observed in the COBOLT data. In fact, smaller amplitude mean currents would bring the frequency estimate more into line with the observed sigma-t energy peak at 19-20 hour periods. This evidence again favors the hypothesis that energy peaks at near inertial frequencies in the May 1977 data are a result of Doppler-shifted internal tides of diurnal period.

Vertical coherence at 18 hour periods is high among the COBOLT instruments (always significantly different from zero at the 99% confidence level) so phases between measured quantities can be computed accurately. These phases agree with the predictions of equation (18). An average of all COBOLT instruments shows that u-velocities (alongshore east) lag v-velocities (onshore) by $91^\circ \pm 5^\circ$, indicating a clockwise rotation of ellipses. Also, lower layer

(level 3) alongshore velocities lead thermocline (level 3) sigma-t variations by $170^{\circ} \pm 10^{\circ}$ --again in close agreement to predicted values.

Horizontal coherence between buoys is also high at 18 hour periods and phases generally small (less than 20°) indicating that the wave crests are parallel to the mooring transect (perpendicular to the shore). Phase differences that do exist can be explained by considering the different mean alongshore velocities at each of the moorings.

The comparison of observations with the idealized vertical boundary Kelvin wave model fails in certain respects. The boundary condition used to choose the offshore decay scale (equation (33)) demands that onshore velocities be identically zero everywhere. Furthermore, the magnitude of the decay scale, using appropriate values of ω , f , and k , suggests that the e-folding distance should be less than 3 km. Observations, by contrast, indicate that onshore velocities are comparable to alongshore velocities ($u/v \approx 0.9$) and that their magnitudes do not show any measureable decrease offshore, even out to 12 kilometers (buoy 4).

It is apparent from the discussion that led to equation (34) that the absence of onshore currents and the choice of a decay scale are both a consequence of the no-normal-flow boundary condition. In view of the relatively gentle bottom slope (see chapter 3), this boundary condition and the traditional Kelvin wave model are probably inappropriate for the COBOLT region. The pycnocline intersects the bottom

several kilometers from the shore and suggests that the boundary condition may be modelled more correctly by demanding that

$$\int v \, dz = 0 . \quad (35)$$

This condition is already met by the baroclinic modes and cannot be used to determine a decay scale. Unlike the Kelvin wave, however, the integral condition does allow onshore velocities (see equation (18)) for decay scales other than that obtained in equation (32).

Although the traditional, vertical boundary, internal Kelvin wave model fails to account for some of the observed features, it is possible that similar, trapped-wave dynamics are responsible for the observations. Also, because of the strength and persistence of coastal mean currents, it is reasonable to assume that the broadening of the kinetic energy around diurnal frequencies is due to the combined presence of surface and Doppler-shifted internal tidal motions. Wunsch (1975) suggests that a broadening of energy peaks is one of the noticeable features of the internal tide, and that it can be used to distinguish the respective contributions of barotropic and baroclinic tides to current meter records. The presence of a broad peak in both fall and spring measurements suggests a persistent generation mechanism such as the barotropic tide since other possible generation processes (e.g., wind stress) are intermittent and quite different for the two seasons.

Despite these arguments, however, it is difficult to establish unequivocally the reality of the Doppler-shifting mechanism without examining other effects which may be important. Factors such as direct forcing, mean shear, topography, etc., may be responsible for the unusual results of the May, 1977 experiment. Only more inclusive models and further examination of the data will resolve this question.

I. Energy and flux of the internal tide

The energy content of the internal diurnal tide is examined with the aid of equation (24). From table 4 (assuming that the Doppler mechanism is operating) it is apparent that not all of the diurnal internal tidal energy is shifted to the 18 hour band, since 24 hour period velocities still show a substantial amount of variance in the first baroclinic mode (about 30%). It is estimated that this contribution is about one-fourth of the contribution from the 18 hour band and is ignored in the following calculations. Depth integrated values of potential and kinetic energies for the 18 hour band are averaged for buoys 2-4 to give

$$\begin{aligned} \text{K.E.} &= 33 \pm 5 \text{ Joules/m}^2 \\ \text{P.E.} &= 5 \pm 1 \text{ Joules/m}^2 . \end{aligned} \tag{36}$$

This is roughly half of the energy content that can be computed for the surface diurnal tide and less than one-tenth of that of the surface semidiurnal tide.

The ratio of energies is

$$\text{P.E./K.E.} = 0.15 \pm 0.05, \quad (37)$$

again in contrast to the Kelvin wave model. Using the Kelvin wave decay scale in equation (21) suggests equipartition of energy (i.e., $\text{P.E./K.E.} = 1$) while a larger decay scale, more in line with the observations, gives an energy ratio of less than one, as observed.

It is also possible to perform a crude energy flux calculation. Unlike the surface wave flux calculation, where measurable quantities (free surface elevation and velocities) were used for the computation, the flux calculation for internal waves requires some knowledge of the dynamics. For a shore-trapped internal wave, equation (23) can be used if it is assumed that the the group velocity of the wave is not too different than the phase velocity (they are identical for the Kelvin wave); i.e. $C = 20 \text{ km}/24 \text{ hr} = 23 \text{ cm/sec}$. In this case

$$\text{Energy Flux} = 9 \text{ watts/m} \quad (38)$$

alongshore to the west. While this figure is small with respect to computed surface semidiurnal flux rates (chapter 2) it is comparable to deep water internal tide fluxes measured by Wunsch and Hendry (1972).

If the internal wave is assumed to progress alongshore to the west, the source of this energy is probably Long Island Sound. Topographic features at the entrance to the Sound itself are quite

pronounced and undoubtedly provide the correct length scale for generation. The alongshore length scales of topographic features to the south of Long Island, by contrast, are not well-matched to those of the internal tide, but are generally much longer. Thus a topographic generation process such as that proposed by Baines (1973) is more likely to occur at the entrance to the Sound than locally along the South Shore. Furthermore, the entrance to Long Island Sound is wide with respect to the internal tide wavelength and undoubtedly will prevent any transmission across from the southern coast of New England (see Buchwald, 1971). It is also possible, though the matter is open to speculation, that the semi-permanent density front known to exist where the fresh waters of the Sound come into contact with the saline waters of the Mid-Atlantic Bight, play a role in the generation process.

It is not likely that the internal tide evident at 12 hour periods results from generation in Long Island Sound. Internal waves at semidiurnal frequencies are free waves and are therefore able to radiate away from the generation region in all directions. A more likely source would be from offshore (e. g., the shelf break) or onshore generation regions. Because the records are dominated by barotropic currents, analysis of the internal oscillations is very difficult. Even so, there are indications in the COBOLT data that nearshore density fluctuations lead those further out; evidence of generation in the coastal zone. Until longer records are available, it is not feasible to resolve this question fully.

J. Conclusions

The effects of the internal tides on the tidal analysis of chapter 2 should be clear at this point. Semidiurnal velocities show little baroclinic energy present to interfere with the barotropic analysis. Onshore velocities, where the baroclinic effects were the strongest, were indeed subject to the most variations (see chapter 2). Diurnal velocities, during the May 1977 experiment, experienced a bit more interference from internal tides but not nearly so much as might have occurred in the absence of a mean current. In either case, the fact that baroclinic variance is primarily in the first mode promotes the success of the vertical integration as a way of reducing the effects of the baroclinic tides on the results of the barotropic analysis.

REFERENCES

- Apel, J. R., H. M. Byrne, J. R. Proni, and R. L. Charnell. 1975. Observations of oceanic internal and surface waves from the Earth Resources Technology Satellite. Journal of Geophysical Research. 80:865-881.
- Abramowitz, M. and I. Stegun. 1964. Handbook of Mathematical Functions. National Bureau of Standards, Applied Mathematics Series 55. 1046pp.
- Ball, F. K. 1967. Edge waves in a ocean of finite depth. Deep-Sea Research 14:79-88.
- Baines, P. 1973. The generation of tides by flat bump topography. Deep-Sea Research. 20:179-205.
- Beardsley, R. C., W. Boicourt, L. C. Huff, and J. Scott. 1977. CMICE 76: A current meter intercomparison experiment conducted off Long Island in Feb.-Mar. 1976. Woods Hole Oceanog. Inst. Technical Report WHOI 77-62: 123 p.
- Beardsley, R. C., W. Boicourt, and D. Hansen. 1976. Physical oceanography of the Middle Atlantic Bight. in Middle Atlantic Continental Shelf and the New York Bight. vol 2. M. Grant Gross, ed. American Society of Limnology and Oceanography. p. 20-34.
- Bendat, J. S. and A. G. Piersol. 1971. Random Data: Analysis and Measurement. Wiley-Interscience, N. Y.: 407 p.
- Bowden, K. F. 1962. Turbulence. The Sea. Vol. 1. Ed. by M. N. Hill. Interscience Pub., N. Y.: 802-825.
- Bowden, K. F. and L. A. Fairbairn. 1956. Measurements of turbulent fluctuations and Reynolds stresses in a tidal current. Proceedings of the Royal Society of London. A 237:422-438.
- Briscoe, M. 1975. Internal waves in the ocean. Reviews of Geophysics and Space Physics. 13:591-645.
- Buchwald, V. 1971. The diffraction of tides by a narrow channel. Journal of Fluid Mechanics. 46:501-511.
- Butman, B. 1975. On the Dynamics of Shallow Water Currents in Mass. Bay and on the N. England Continental Shelf. Doctoral Dissertation. Massachusetts Institute of Technology and Woods Hole Oceanographic.

- Cartwright, D., W. Munk, and B. Zetler. 1969. Pelagic tidal measurements. EOS. 50:472-477.
- Charnell, R. L. and D. Hansen. 1974. Summary and Analysis of Physical Oceanography Data Collected in the New York Bight During 1969-1970. NOAA/MESA Report No. 74-3. Boulder, CO.
- Cox, C. and H. Sandstrom. 1962. Coupling of internal and surface waves in water of variable depth. Journal of the Oceanographic Society of Japan. 30th Anniversary Volume. 449-513.
- Csanady, G. 1972. The coastal boundary layer in Lake Ontario. Journal of Physical Oceanography. 2:41-53, 168-176.
- Csanady, G. 1977. The coastal jet conceptual model in the dynamics of shallow seas. in The Sea. Vol. 6. E. D. Goldberg, Ed. John Wiley and Sons, N.Y. 117-144.
- Cushing, V. 1976. Electromagnetic water current meter. MTS and IEEE Oceans 76 Conf. Proc 25C. 1-7.
- Defant, A. 1961. Physical Oceanography. Vol. 2, Pergamon Press, N.Y. 560 p.
- Dietrich, G. 1944. Die Schwingungssysteme der half - und eintagigen tiden in den ozeanen. Veroeffentl. Inst. Meerskd. Univ. Berlin. A41:7-68.
- Dimmler, D. G., D. Huszagh, S. Rankowitz, and J. Scott. 1976. A controllable real-time collection system for coastal oceanography. Ocean 76 Conf. Proc. 14E-1:1-13.
- Doodson, A. T. and H. D. Warburg. 1941. Admiralty Manual of the Tides. His Majesty's Stationery Office, London:270 pp.
- Dronkers, J. J. 1964. Tidal computation in rivers and coastal waters. North-Holland Pub., Amsterdam. 173 pp.
- Eckart, C. 1960. Hydrodynamics of Oceans and Atmospheres. Pergamon Press, N.Y. 290 pp.
- EG&G, Environmental Consultants. 1975. Summary of Oceanographic Observations in New Jersey Coastal Waters near 39 28'N Latitude and 74 15'W Longitude during the period May, 1973 through May, 1974. A Report to the Public Service Electric and Gas Co., Newark, N.J.
- Emery, K. O. and E. Uchupi. 1972. Western North Atlantic. Amer. Assoc. of Petroleum Geologists, Tulsa, Okla. 532 pp.

- Ferrel, Wm. 1874. Tidal Researches. U. S. Coast Survey Rept. U. S. Govt. Printing Office, Washington, D.C. 268 pp.
- Filloux, J. H. 1971. Deep-sea tide obs. from the northeastern Pacific. Deep-Sea Research. 18:275-284.
- Flagg, C. N. 1977. The Kinematics and the Dynamics of the New England Continental Shelf and Shelf/Slope Front. Doctoral Dissertation, Massachusetts Institute of Technology-Woods Hole Oceanographic Institution. 207 pp.
- Gould, W. and W. McKee. Vertical structure of semidiurnal tidal currents in the Bay of Biscay. Nature. 244:88-91.
- Haight, F. J. 1942. Coastal Currents along the Atlantic Coast of the United States. U. S. Coast and Geodetic Survey Spec. Publ. No. 230. 73 pp.
- Halpern, D. 1971. Semidiurnal internal tides in Massachusetts Bay. Journal of Geophysical Research. 76:6573-6584.
- Hendershott, M. C. 1973. Ocean tides. EOS 54:76-86.
- Hendershott, M. C. 1977. Numerical models of ocean tides. The Sea. Vol. 6. E. D. Goldberg, Ed. John Wiley and Sons, N.Y. 47-95.
- Hendershott, M. C. and W. Munk. 1970. Tides. Annual Review of Fluid Mechanics. Vol. 2. M. Van Dyke, Ed. Annual Reviews, Inc. Palo Alto, CA. 205-224.
- Hendershott, M. C. and A. Speranza. 1971. Co-oscillating tides in long, narrow bays; the Taylor problem revisited. Deep-Sea Research. 18:959-980.
- Hendry, R. M. 1975. The Generation, Energetics and Propagation of Internal Tides in the Western North Atlantic. Doctoral Dissertation, Massachusetts Institute of Technology-Woods Hole Oceanographic Institution. 345 pp.
- Ketchum, B. and N. Corwin. 1964. The persistence of "winter" water on the continental shelf south of Long Island, New York. Limnology and Oceanography. 9(4):467-475.
- Krauss, W. 1966. Methoden und Ergebnisse der Theoretischen Ozeanographie: Interne Wellen. Gebruder Bor'ntraeger, Berlin. 248 pp.

- Krauss, W. 1973. Methods and Results of Theoretical Oceanography: Dynamics of the Homo. and Quasihomo. Ocean. Gebruder Bor'ntraeger, Berlin. 302 pp.
- Krol, H. 1974. Some numerical considerations: Eigenvalue problems in the theories of underwater sound and internal waves. NATO SACLANT ASW Memorandum SM-40.
- Lamb, H. 1932. Hydrodynamics. Dover Pub., N.Y. 738 pp.
- Lee, O. 1961. Observations on internal waves in shallow water. Limnology and Oceanography. 6:312-321.
- Lowe, R. L., D. L. Inman, and B. M. Brush. 1972. Simultaneous data system for instrumenting the shelf. 13th Conf. on Coastal Eng., Vancouver, B.C.
- Magaard, L., and W. McKee. 1973. Semidiurnal tidal currents at Site D. Deep-Sea Research. 20:997-1009.
- McCullough, J. 1977. Problems in measuring currents near the ocean surface. MTS & IEEE Ocean 77 Conf. Proceedings 468:1-7.
- Miles, J. 1974. On Laplace's tidal equations. Journal of Fluid Mechanics. 66:241-260.
- Miller, G. 1966. The flux of tidal energy out of the deep ocean. Journal of Geophysical Research. 71(10):2485-2489.
- Mooers, C. N. K. 1975. Several effects of a baroclinic current on the cross-stream propagation of inertial-internal waves. Geophysical Fluid Dynamics. 6:245-275.
- Morse, P. and H. Feshback. 1953. Methods of Theoretical Physics. McGraw-Hill, New York.
- Munk, W. 1968. Once again--tidal friction. Quart. Jour. Roy. Astron. Soc. 9:352-375.
- Munk, W. and D. Cartwright. 1966. Tidal spectroscopy and prediction. Proc. Roy. Soc. London. A259:533-581.
- Munk, W., F. Snodgrass, and M. Wimbush. 1970. Tides off-shore: Transition from California coastal to deep-sea waters. Geophysical Fluid Dynamics. 1:161-235.
- Mysak, L. 1978. Wave propagation in random media, with oceanic applications. Reviews of Geophysics and Space Physics. 16(2):233-261.

- Niiler, P. O. 1975. A report on the continental shelf circulation and coastal upwelling. Reviews of Geophysics and Space Physics. 13(3):609-659.
- Patchen, R., E. Long, and B. Parker. 1976. Analysis of Current Meter Observations in the New York Bight Apex, August, 1973-June, 1974. NOAA Technical Report 368-MESA 5. U. S. Department of Commerce. 24 pp.
- Peregrine, D. H. 1976. Interaction of water waves and currents. in Advances in Applied Mechanics, vol.16. C. S. Yih, Ed. Academic Press, N. Y. p9-117.
- Petrie, B. 1975. M_2 surface and internal tides on the Scotian shelf and slope. Journal of Marine Research. 33:303-323.
- Phillips, N. A. 1966. The equations of motion for a shallow rotating atmosphere and the "traditional" approximation. Journal of Atmospheric Science. 23:626-628.
- Phillips, O. 1966. Dynamics of the Upper Ocean. Cambridge Univ. Press. 261p.
- Platzmann, G. 1971. Ocean tides and related waves. Lectures on Applied Mathematics, v. 14. Ed. by W. Reid. American Mathematical Society, Providence, R.I.
- Prinsenber, S. J., W. Wilmot, and M. Rattray, Jr. 1974. Generation and dissipation of coastal internal tides. Deep-Sea Research. 21:263-281.
- Proudman, J. 1941. The effect of coastal friction on the tides. Geophys. Suppl. Mon. Nat. Roy. Astrono. Soc. 5(1):23-26.
- Proudman, J. 1953. Dynamical Oceanography. John Wiley, N.Y. 409 pp.
- Rattray, M. 1960. On the coastal generation of internal tides. Tellus. 12:54-62.
- Redfield, A. 1950. The analysis of tidal phenomena in narrow embayments. Papers in Physical Oceanography and Meteorology. 11(4):1-36.
- Redfield, A. 1958. The influence of the continental shelf on the tides of the Atlantic coast of the United States. Journal of Marine Research. 17:432-448.
- Redfield, A. 1978. The tide in coastal waters. Journal of Marine Research. 36:255-294.

- Regal, R. and C. Wunsch. 1973. M_2 tidal currents in the western North Atlantic. Deep-Sea Research. 20(5):493-502.
- Rooth, C. 1972. A linearized bottom friction for large scale oceanic motions. Journal of Physical Oceanography. 2(2):509-510.
- Scott, J. and G. Csanady. 1976. Nearshore currents off Long Island. Journal of Geophysical Research. 81(30):5401-5409.
- Scott, J., T. Hopkins, R. Pillsbury, and E. Davis. 1978. Velocity and Temperature off Shinnecock, Long Island in October-November, 1976. Oceanographic Services Division, Brookhaven National Laboratory (unpublished manuscript).
- Shureman, P. 1958. Manual of Harmonic Analysis and Prediction of Tides. U. S. Coast and Geodetic Survey, Special Publication No. 98. U. S. Government Printing Office, Washington, D.C. 317 pp.
- Smith, P., B. Petrie, and C. Mann. 1978. Circulation, variability and dynamics of the Scotian Shelf and Slope. Jour. Fish. Res. Board Can. 35:1067-1083.
- Sverdrup, H. 1926. Dynamics of tides on the North Siberian shelf. Geophys. Publ. 4(5):1-75.
- Sverdrup, H., M. Johnson, and R. Fleming. 1942. The Oceans. Prentice-Hall, Inc., Englewood Cliffs, N.J. 1087 pp.
- Swanson, R. 1976. Tides. MESA New York Bight atlas Monograph 4. New York Sea Grant Inst., Albany, N.Y. 34 pp.
- Swift, D., D. Duane, and T. McKinney. 1973. Ridge and swale topography of the Middle Atlantic Bight, North America: Secular response to the Holocene hydraulic regime. Marine Geology. 15:227-247.
- Taylor, G. I. 1919. Tidal friction in the Irish Sea. Phil. Trans. Roy. Soc. A220:1-93.
- Traschen, J. 1976. Tides of the New England continental shelf. Woods Hole Oceanographic Institution (unpublished manuscript).
- Whitham, G. 1960. A note on group velocity. Journal of Fluid Mechanics. 9:347-352.
- Winant, C. 1974. Internal surges in coastal waters. Journal of Geophysical Research. 79:4523-4526.
- Winant, C. 1978. Coastal current observations. To appear in Reviews of Geophysics and Space Physics.

- Wunsch, C. 1969. Progressive waves on slopes. Journal of Fluid Mechanics. 35:131-144.
- Wunsch, C., and R. Hendry. 1972. Array measurements of the bottom boundary layer and the internal wave field on the continental slope. Geophysical Fluid Dynamics. 4:101-145.
- Wunsch, C. 1975. Internal tides in the ocean. Reviews of Geophysics and Space Physics. 13:167-182.

BIOGRAPHICAL NOTE

Paul May was born on June 14, 1950 in Chicago, Illinois. He spent most of his younger years in the suburb of Hinsdale. Paul graduated from high school in 1968 with high scholastic honors. After attending Southern Missionary College in Collegedale, Tennessee for four years, he graduated as a physics major and as president of his class in 1972. As a graduate student, he enrolled in the Department of Geophysical Sciences at the University of Chicago for one year before coming to Woods Hole Oceanographic Institution and Massachusetts Institute of Technology.

Paul is interested in a variety of outdoor activities, including back-packing, scuba-diving, and skiing. He is also an avid photographer. He is married to the former Sandra Watkins of E. Falmouth, Massachusetts and will have a child in the near future (5 months!).